DE GRUYTER
OLDENBOURG

POWER ELECTRICAL SYSTEMS

Edited by Faouzi Derbel, Nabil Derbel, Olfa Kanoun

ADVANCES IN SIGNALS, SYSTEMS AND DEVICES 11

Faouzi Derbel, Nabil Derbel, Olfa Kanoun (Eds.)
Power Systems & Smart Energies

Advances in Signals, Systems and Devices

Edited by
Olfa Kanoun, University of Chemnitz, Germany

Volume 11

Power Systems & Smart Energies

———

Edited by
Faouzi Derbel, Nabil Derbel, and Olfa Kanoun

DE GRUYTER
OLDENBOURG

Editors of this Volume

Prof. Dr.-Ing. Faouzi Derbel
Leipzig University of Applied Sciences
Chair of Smart Diagnostic and Online Monitoring
Wächterstrasse 13
04107 Leipzig, Germany
faouzi.derbel@htwk-leipzig.de

Prof. Dr.-Ing. Olfa Kanoun
Technische Universität Chemnitz
Chair of Measurement and Sensor Technology
Reichenhainer Strasse 70
09126 Chemnitz
olfa.kanoun@etit.tu-chemnitz.de

Prof. Dr.-Eng. Nabil Derbel
University of Sfax
Sfax National Engineering School
Control & Energy Management Laboratory
1173 BP, 3038 SFAX, Tunisia
n.derbel@enis.rnu.tn

Advances in Systems, Signals and Devices

Editors in Chief:

Systems, Analysis & Automatic Control

Prof. Dr.-Eng. Nabil Derbel
ENIS, University of Sfax, Tunisia
n.derbel@enis.rnu.tn

Power Systems & Smart Energies

Prof. Dr.-Ing. Faouzi Derbel
Leipzig Univ. of Applied Sciences, Germany
derbel@eit.htwk-leipzig.de

Communication, Signal Processing & Information Technology

Prof. Dr.-Ing. Faouzi Derbel
Leipzig Univ. of Applied Sciences, Germany
derbel@eit.htwk-leipzig.de

Sensors, Circuits & Instrumentation Systems

Prof. Dr.-Ing. Olfa Kanoun
Technische Universität Chemnitz, Germany
olfa.kanoun@etit.tu-chemnitz.de

Editorial Board Members:

Systems, Analysis & Automatic Control

Dumitru Baleanu, Çankaya University, Ankara, Turkey
Ridha Ben Abdennour, Engineering School of Gabès, Tunisia
Naceur Benhadj, Braïek, ESSTT, Tunis, Tunisia
Mohamed Benrejeb, Engineering School of Tunis, Tunisia
Riccardo Caponetto, Universita' degli Studi di Catania, Italy
Yang Quan Chen, Utah State University, Logan, USA
Mohamed Chtourou, Engineering School of Sfax, Tunisia
Boutaïeb Dahhou, Univ. Paul Sabatier Toulouse, France
Gérard Favier, Université de Nice, France
Florin G. Filip, Romanian Academy Bucharest Romania
Dorin Isoc, Tech. Univ. of Cluj Napoca, Romania
Pierre Melchior, Université de Bordeaux, France
Faïçal Mnif, Sultan qabous Univ. Muscat, Oman
Ahmet B. Özgüler, Bilkent University, Bilkent, Turkey
Manabu Sano, Hiroshima City Univ. Hiroshima, Japan
Abdul-Wahid Saif, King Fahd University, Saudi Arabia
José A. Tenreiro Machado, Engineering Institute of Porto, Portugal
Alexander Pozniak, Instituto Politecniko, National Mexico
Herbert Werner, Univ. of Technology, Hamburg, German
Ronald R. Yager, Mach. Intelligence Inst. Iona College USA
Blas M. Vinagre, Univ. of Extremadura, Badajos, Spain
Lotfi Zadeh, Univ. of California, Berkeley, CA, USA

Power Systems & Smart Energies

Sylvain Allano, Ecole Normale Sup. de Cachan, France
Ibrahim Badran, Philadelphia Univ., Amman, Jordan
Ronnie Belmans, University of Leuven, Belgium
Frdéric Bouillault, University of Paris XI, France
Pascal Brochet, Ecole Centrale de Lille, France
Mohamed Elleuch, Tunis Engineering School, Tunisia
Mohamed B. A. Kamoun, Sfax Engineering School, Tunisia
Mohamed R. Mékidèche, University of Jijel, Algeria
Bernard Multon, Ecole Normale Sup. Cachan, France
Francesco Parasiliti, University of L'Aquila, Italy
Manuel Pérez,Donsión, University of Vigo, Spain
Michel Poloujadoff, University of Paris VI, France
Francesco Profumo, Politecnico di Torino, Italy
Alfred Rufer, Ecole Polytech. Lausanne, Switzerland
Junji Tamura, Kitami Institute of Technology, Japan

Communication, Signal Processing & Information Technology

Sensors, Circuits & Instrumentation Systems

Advances in Systems, Signals and Devices

Volume 1
N. Derbel (Ed.)
Systems, Automation, and Control, 2016
ISBN 978-3-11-044376-9, e-ISBN 978-3-11-044843-6,
e-ISBN (EPUB) 978-3-11-044627-2, Set-ISBN 978-3-11-044844-3

Volume 2
O. Kanoun, F. Derbel, N. Derbel (Eds.)
Sensors, Circuits and Instrumentation Systems, 2016
ISBN 978-3-11-046819-9, e-ISBN 978-3-11-047044-4,
e-ISBN (EPUB) 978-3-11-046849-6, Set-ISBN 978-3-11-047045-1

Volume 3
F. Derbel, N. Derbel, O. Kanoun (Eds.)
Power Systems & Smart Energies, 2016
ISBN 978-3-11-044615-9, e-ISBN 978-3-11-044841-2,
e-ISBN (EPUB) 978-3-11-044628-9, Set-ISBN 978-3-11-044842-9

Volume 4
F. Derbel, O. Kanoun, N. Derbel (Eds.)
Communication, Signal Processing & Information Technology, 2016
ISBN 978-3-11-044616-6, e-ISBN 978-3-11-044839-9,
e-ISBN (EPUB) 978-3-11-043618-1, Set-ISBN 978-3-11-044840-5

Volume 5
N. Derbel, F. Derbel, O. Kanoun (Eds.)
Systems, Automation, and Control, 2017
ISBN 978-3-11-046821-2, e-ISBN 978-3-11-047046-8,
e-ISBN (EPUB) 978-3-11-046850-2, Set-ISBN 978-3-11-047047-5

Volume 6
O. Kanoun, N. Derbel, F. Derbel (Eds.)
Sensors, Circuits and Instrumentation Systems, 2017
ISBN 978-3-11-044619-7, e-ISBN 978-3-11-044837-5,
e-ISBN (EPUB) 978-3-11-044624-1, Set-ISBN 978-3-11-044838-2

Volume 7
F. Derbel, N. Derbel, O. Kanoun (Eds.)
Power Systems & Smart Energies, 2018
ISBN 978-3-11-046820-5, e-ISBN 978-3-11-047052-9,
e-ISBN (EPUB) 978-3-11-044628-9, Set-ISBN 978-3-11-047053-6

Volume 8
F. Derbel, N. Derbel, O. Kanoun (Eds.)
Communication, Signal Processing & Information Technology, 2018
ISBN 978-3-11-046822-9, e-ISBN 978-3-11-047038-3,
e-ISBN (EPUB) 978-3-11-046841-0, Set-ISBN 978-3-11-047039-0

Volume 9
N. Derbel, F. Derbel, O. Kanoun (Eds.)
Systems, Automation, and Control, 2019
ISBN 978-3-11-059024-1, e-ISBN 978-3-11-059172-9,
e-ISBN (EPUB) 978-3-11-059031-9

Volume 10
O. Kanoun, N. Derbel, F. Derbel (Eds.)
Sensors, Circuits and Instrumentation Systems, 2019
ISBN 978-3-11-059025-8, e-ISBN 978-3-11-059256-6,
e-ISBN (EPUB) 978-3-11-059128-6

Contents

M. T. Lazim and A. Al-Faoury

Multi-phase Current Source Cycloconverter Using Amplitude Modulation Technique

Abstract: This paper proposed a new frequency changer which can be regarded as a current source cycloconverter. Frequency changing is achieved by mixing two or more amplitude modulated current waves at supply frequency using power transistors. By appropriate selection of the modulation indices and phase shift between the supply voltages, the supply frequency component can be entirely suppressed. The harmonics content of the resulting current wave is found to be very low. This converter solves the problems and severe restrictions associated with the ordinary full-cycle synchronous AM modulation when applied to three-phase and multi-phase systems. The process of conversion involves only natural commutation.

Keywords: power electronics, A.C. converters, cycloconverter, frequency changers, a.c drives.

Classification: 65C05, 62M20, 93E11, 62F15, 86A22

1 Introduction

The circuits used for power frequency conversion are classified into two groups: inverters and cycloconverters. In inverters, the conversion process is accomplished via DC link, while in cycloconverters; the alternating voltage at supply frequency is converted directly to a lower frequency voltage without any intermediate DC stage. Inverters that commonly used in industry are classified into two groups: voltage source inverters (VSI) and current source inverters (CSI) [1–6]. The VSI were used more often than the CSI because of their better properties. On the other hand, only voltage source cycloconverters in the forms of phase angle controlled and envelope cycloconverters are known in industry [1]. The operating principles of these types of frequency changers are well known and their circuits are well developed in the last six decays. These circuits have an advantage on inverters in that they permit the conversion of a fixed input frequency to a variable output frequency at variable voltage in single stage (direct AC to AC conversion). Such schemes are attractive for AC motor drives.

M. T. Lazim and A. Al-Faoury: M. T. Lazim: Philadelphia University-Jordan,
email: drmohamadtofik@yahoo.com A. Al-Faoury: Al-Balqa' Applied University-Jordan,
email: audihalfaoury@gmail.com

Some other new conversion methods from AC to AC have also been reported such as matrix converter, integrated PWM converter / inverter and bi-phase integral cycle control technique systems [7–10]. These methods have gained considerable acceptance as schemes in the field of power frequency changing and speed control of induction motors.

Compared with a VSI system, the output current of a CSI system is not influenced by the supply voltage, so its output current has low *THD* and high *PF*. Hence, in the 1980s the current source inverters were the main commonly used electric machine feeding devices. The current source inverter was constructed of a thyristor bridge with large inductance and large commutation capacitors. Serious problems in such drive systems were unavoidable overvoltage cases during the thyristor commutation, as the current source inverter current is supplied in a cycle from a dc-link circuit to the machine phase winding. The thyristor CSI has been replaced recently by the transistor reverse blocking IGBT devices (RBIGBT), where the diode is series-connected and placed in one casing with transistor. The power transistors like RBIGBT or Silicon Carbide (SiC) used in the modern CSIs guarantee superior static and dynamic drive characteristics. The use of current sources for the electric machine control ensures better drive properties than in case of voltage sources, where it may be necessary to use an additional passive filter at the inverter output [11, 12].

In this paper an attempt is made to design and build a new current source cycloconverter exploiting the principle of discrete amplitude modulation using RBIGBT power transistor. Although the voltage source cycloconverter is well known in industry, no previous work, to the knowledge of the authors, had been reported on a current source cycloconverter.

2 Principles of discrete amplitude modulation in power transistor circuits (AM current waves mixing)

It has been shown, by the first author, that the load voltage waveforms, corresponding to symmetrical phase-angle triggering and integral-cycle triggering in thyristor circuits, are all discrete forms of amplitude modulation [13]. In each case the modulated output voltage is obtained from a sinusoidal (supply) carrier signal by use of a rectangular modulating function, depending on the power semiconductor device switching pattern.

In general, to illustrate the amplitude modulation process of synchronous type, consider a current wave shown in Fig. 1(a), which represent a voltage or current function $c(t)$ (carrier wave) of angular frequency ω. If this function is multiplied (modulated) with a rectangular modulating signal $s(t)$ whose frequency is a sub-multiple of
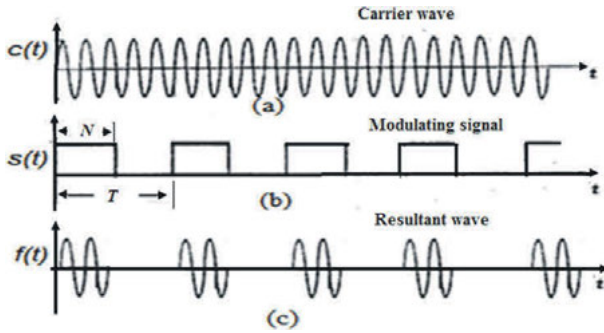
Fig. 1: Amplitude modulation process in power transistor circuits. N : number of conducting cycles and T : control period in cycles.

the carrier (ωT), produced by the switching device, Fig. 1(b), the resultant modulated wave will be as shown in Fig. 1(c).

Mathematically the resultant modulated wave is found to consist of two terms as given in the following general equation [13]:

$$f(t) = A\left(\frac{N}{T}\right)\sin\omega t + \sum_{r=1}^{\infty} H_r \sin\frac{\pi r N}{T}\sin\frac{r}{T}(\omega t - \pi N) \tag{1}$$

where:

$$H_r = \frac{AT}{\pi(T^2 - r^2)} \ , \quad r \neq T \tag{2}$$

$r = r^{th}$ order harmonic component, and A = Amplitude of $c(t)$.

The first term on the *RHS* of equation (1) gives the carrier component. The second term denotes the positive frequency upper side band only.

The use of amplitude modulation (AM) techniques for frequency conversion to realise voltages of non-supply frequency using thyristor circuits, in the form of integral-cycle triggering, are now in common use. However, it is possible to realise amplitude modulated current waves of the same characteristics as that of AM voltage waves by using the power transistor devices such as IGBTs. In order to understand this concept, consider the simple system shown in Fig. 2. Input voltages v_1 and v_2 are of the same frequency and amplitude, but they are shifted in time phase by an angle θ. These voltage sources, together with the large series inductors represent the required current sources.

Now if each controller is gated independently with same switching (modulating) functions of rectangular waveforms of amplitude ±l, to permit a different number of conduction cycles N_1 or N_2 for the current drawn from each source, the modulator produces a composite wave of the two amplitude modulated current waveforms i_1 and i_2. For reference current i_1 and assuming resistive load, the modulated current waves drawn from the two controllers are,

$v_1 = V_m \sin \omega t$, $v_2 = V_m \sin(\omega t - \theta)$
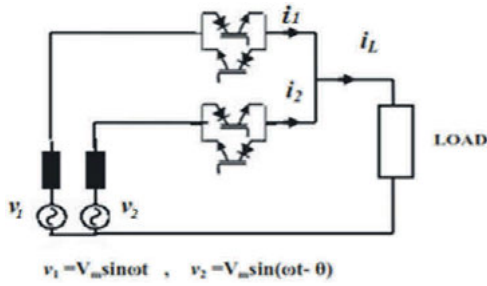
Fig. 2: Two-phase to single-phase converter.

$$i_1(t) = I_m \left(\frac{N_1}{T}\right) \sin \omega t + \sum_{r=1}^{\infty} H_r \sin \frac{\pi r N_1}{T} \sin \frac{r}{T}(\omega t - \pi N_1) \tag{3}$$

$$i_2(t) = I_m \left(\frac{N_2}{T}\right) \sin(\omega t - \theta) + \sum_{r=1}^{\infty} H_r \sin \frac{\pi r N_2}{T} \sin \frac{r}{T}(\omega t - \pi N_2 - \theta) \tag{4}$$

where:

$$H_r = \frac{I_m T}{\pi(T^2 - r^2)} \ , \ \ r \neq T \tag{5}$$

Assuming now, for simplicity, that $N_1 = N_2 = N$, the mathematical expression for the load current $i_L(t)$ becomes: $i_L(t) = i_1(t) + i_2(t)$. Thus,

$$i_L(t) = 2I_m \left(\frac{N}{T}\right) \sin \frac{\theta}{2} \sin(\omega t + \varphi) + \sum_{r=1}^{\infty} 2H_r \sqrt{\sin \frac{\pi r N}{T} \sin \frac{r\theta}{2}} \sin\left(\frac{r\omega t}{T} + \beta\right) \tag{6}$$

where:

$$\varphi = \arctan \frac{\sin \theta}{1 - \cos \theta} \tag{7}$$

and

$$\beta = \arctan \frac{\left(1 - \cos \frac{2\pi r N}{T}\right)\left(1 - \cos \frac{r\theta}{T}\right) - \sin \frac{2\pi r N}{T} \sin \frac{\theta}{2}}{\left(1 - \cos \frac{r\theta}{2}\right)\sin \frac{2\pi r N}{T} + \left(1 - \cos \frac{2\pi r N}{T}\right)\sin \frac{r\theta}{2}} \tag{8}$$

Equation (6) represents an amplitude modulated wave whose phase is varying with undefined angle θ. It is interesting to consider certain features that can arise from the mixing of two amplitude modulated current waves. It is clear that the phase difference angle is the effective parameter that specifies the resulting waveform. The supply frequency component (carrier) can entirely be suppressed from the output current waveform by proper selection of phase angle, ($\theta = 2\pi N$ in this case). Also with judicious selection of the values N, T and θ, it is easy to produce a current waveform with harmonic content less than that of the individual current waveforms, as it will be seen in the three-phase to single-phase conversion illustrated in the following section.

3 Three-phase to single-phase frequency changer

If we use three controllers (modulators) and a three-phase current power supply, as shown in Fig. 3, then we can obtain a three-phase to single-phase frequency changer. If a synchronous full-cycle AM technique is applied to respective three modulators of Fig. 3.

The resultant wave of Fig. 4 can be expressed using (2) as a general form for i_a, i_b, and i_c with $\theta_1 = 0$, $\theta_2 = \frac{2\pi}{3}$, and $\theta_3 = \frac{4\pi}{3}$, and for $r \neq T$ as:

$$i_L = I_m\left(\frac{N}{T}\right)\left[\sin\omega t + \sin\left(\omega t - \frac{2\pi}{3}\right) + \sin\left(\omega t - \frac{4\pi}{3}\right)\right]$$

$$+ \sum_{r=1}^{\infty} H_r'\left(\sin\frac{\pi r N}{T}\right)^{\frac{3}{2}} \sum_{k=1}^{3} \sin\frac{r}{T}\left(\omega t - \frac{2\pi}{T}(k-1) - \pi N\right) \tag{9}$$

where:

$$H_r' = 2I_m\frac{T}{\pi(T^2 - r^2)}\left(\sin\frac{\pi r N}{T}\right)^{\frac{3}{2}} \tag{10}$$

and for $k = 1, 2, 3$ (number of phases), The first term of the *RHS* of (9) will sum to zero leaving only the second term . This indicates that the supply frequency component ($r = T$) or the carrier is entirely suppressed. Hence, the final form of (9) becomes:

$$i_L = 2\sum_{r=1}^{\infty} 2I_m\frac{T}{\pi(T^2 - r^2)}\sin\frac{\pi r N}{T}\frac{\sin\frac{\pi r}{T}}{\sin\frac{\pi r}{3T}}\sin\frac{r}{T}\left(\omega t - \frac{2\pi}{3} - \pi N\right) \tag{11}$$

The amplitude of the rth harmonic of the load current for $r \neq T$ is given by:

$$C_r = 2I_m\frac{T}{\pi(T^2 - r^2)}\sin\frac{\pi r N}{T}\frac{\sin\frac{\pi r}{T}}{\sin\frac{\pi r}{3T}} \tag{12}$$
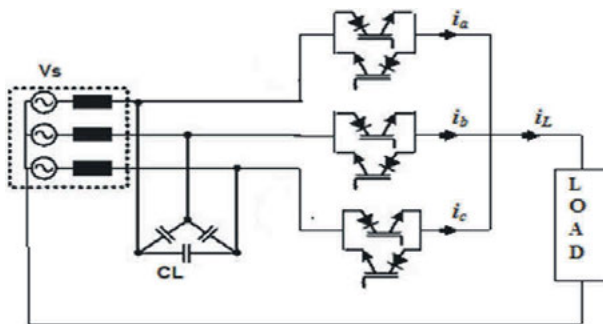
Fig. 3: Three-phase to single-phase converter. then the individual and the resultant modulated current, $i_L(t) = i_a(t) + i_b(t) + i_c(t)$, waveforms will be as shown in Fig.4.
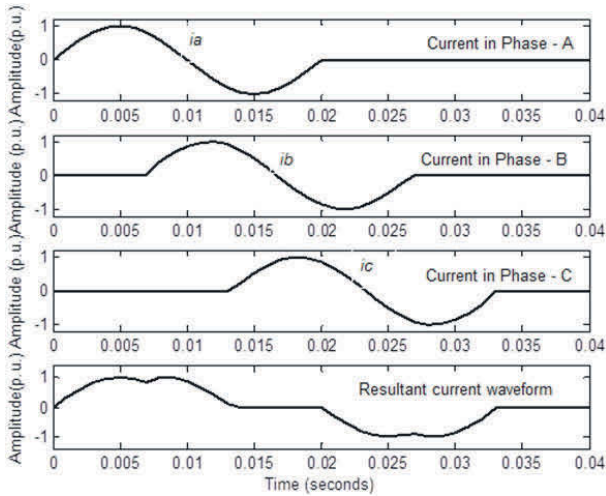
Fig. 4: Modulated current waveforms of the individual phases and the resultant load current waveform for $N = 1$, $T = 2$ (output frequency $f_0 = 25$ Hz).

It should be noted that only odd harmonics exist since, for even harmonics, $C_r = 0$. Frequency spectra of the resultant load current wave of Fig. 4 is shown in Fig. 5, while Figs. 6 to 9 show the resultant current wave and frequency spectra for different values of modulation indices respectively.

It is of significant to not that the subharmonics generated for all cases are between the limits $f = \frac{1}{T}$ and $f = +\infty$. Consequently, one can obtain frequency division below the supply frequency by proper selection of the modulation indices N and T.
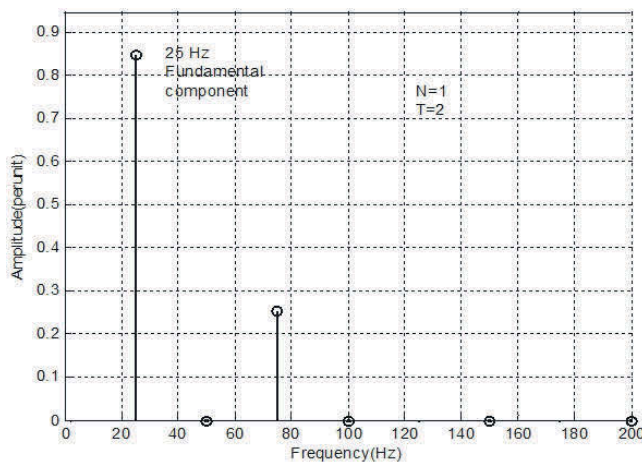
Fig. 5: Frequency spectra of the resultant modulated wave for $N = 1$, $T = 2$.
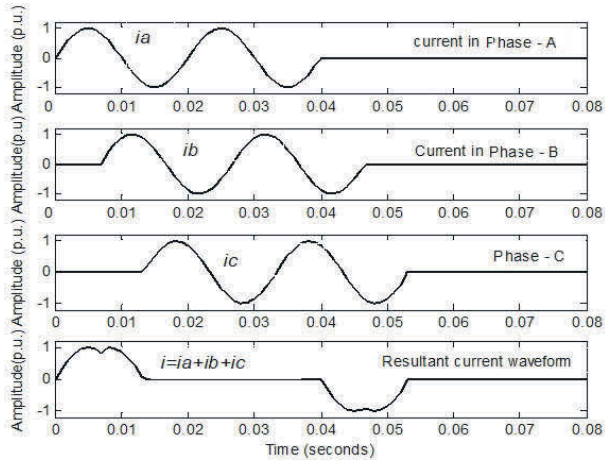
Fig. 6: Modulated current waveforms of the individual phases and the resultant load current waveform for $N = 2$, $T = 4$ (output frequency $f_0 = 12.5$Hz).
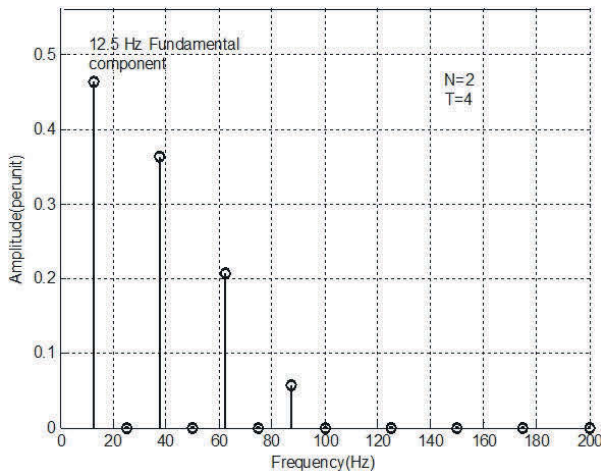
Fig. 7: Frequency spectra of the resultant modulated wave for $N = 2$, $T = 4$.

4 Multi-phase system

For m-phase balanced input current system it can be prove that the amplitude of the rth harmonic of the load current for $r \neq T$, is given by

$$C_r = 2I_m \frac{T}{\pi(T^2 - r^2)} \sin \frac{\pi r N}{T} \frac{\sin \frac{\pi m r}{T}}{\sin \frac{\pi r}{3T}} \tag{13}$$
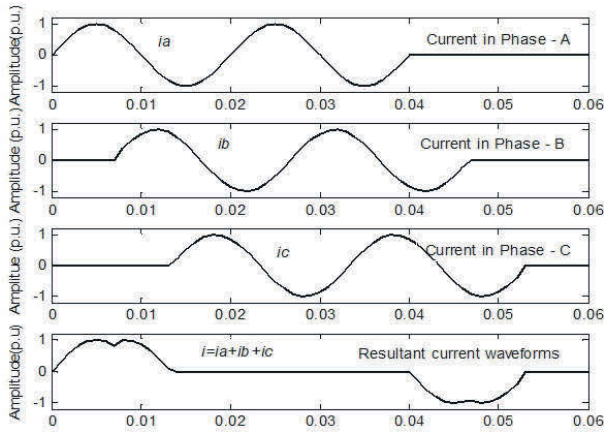
Fig. 8: Modulated current waveforms of the individual phases and the resultant load current waveform for $N = 2$, $T = 3$ (output frequency $f_0 = 16.6$ Hz).
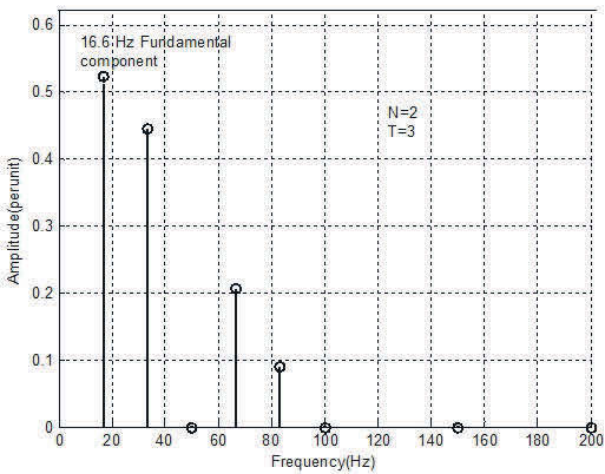
Fig. 9: Frequency spectra of the resultant modulated current wave for $N = 2$, $T = 3$.

where m is the number of phases used.

For a six-phase system, for example, the resultant modulated load current wave in case of resistive load is shown in Fig. 10 for modulation indices, $N = 1$, $T = 2$. The harmonic content of this concurrent consecutive modulated wave is shown in Fig. 11.

From Fig. 10, it can be seen that the output current waveform obtained by six-phase system is nearly sinusoidal. The harmonic content of this waveform is very low as it is clear from Fig. 11. The resultant waveform is free from spikes and
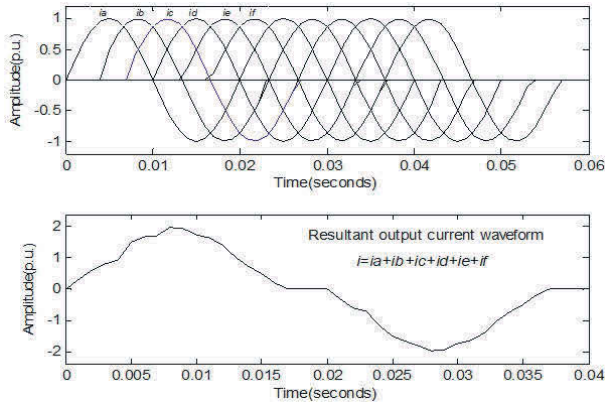
Fig. 10: Modulated current waveforms of the individual phases and the resultant load current waveform for $N = 1$, $T = 2$, for six-phase system (output frequency $f_0 = 25$Hz).
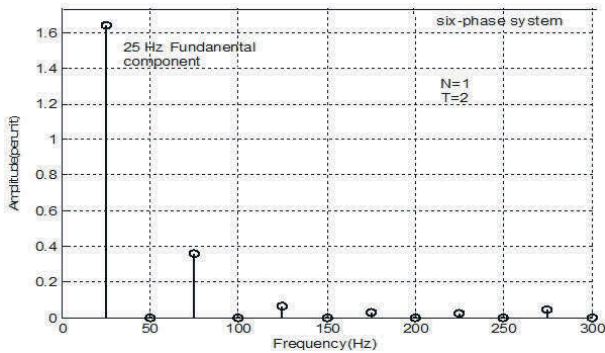
Fig. 11: Frequency spectra of the resultant wave for six-phase system with $N = 1$, $T = 2$.

undesirable discontinuities as it is compared with that produced by the conventional voltage source cycloconverters.

For higher modulation indices, $N = 1$ and $T = 3$, the resultant output current wave will be at lower frequency (16.3Hz) and the quality of the waveform is still acceptable, see Figs. 12 and 13 for the output waves and frequency spectra respectively.

5 Practical Implementation

The three-phase to single-phase converter shown in Fig. 13 was designed, built and tested in the laboratory. Experimental results were found to agree well with the theory. Oscillogram of the load current wave with resistive load is shown in Fig. 14.
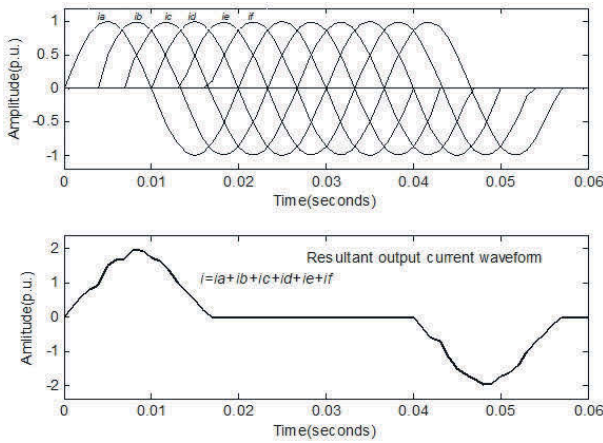
Fig. 12: Modulated current waveforms of the individual phases and the resultant load current waveforms for six-phase system for $N = 2$, $T = 3$, (output frequency $f_0 = 16.6$Hz).
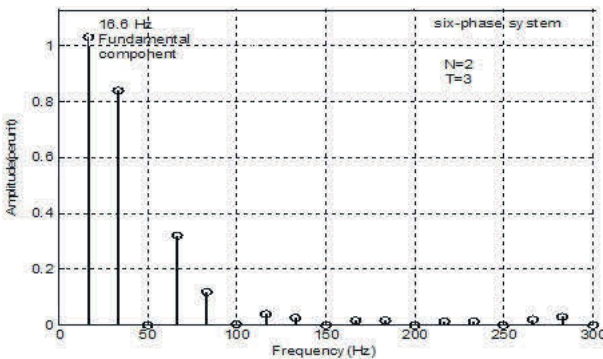
Fig. 13: Frequency spectra of the resultant modulated wave of Fig.12 for $N = 2$, $T = 3$.

A three-phase version of three-phase to single-phase converter was also constructed and tested with resistive load, highly inductive load and induction motor. A schematic diagram of this three-phase to three-phase converter is shown in Fig. 15 feeding a three-phase induction motor.

With resistive load, the converter showed fewest problems since there is no energy fedback to the supply. However with $R - L$, freewheeling transistors are added for each phase to overcome this problem. Three-phase 220V, 50Hz, supply was used for experimental purposes. The motor parameters are: P = 500W, V = 380V Y/220V $\triangle$, I = 1.2A / 2.1A, n_s = 2850r.p.m., frequency=50Hz, Number of poles = 2. With motor load, the converter showed satisfactory operation with output frequencies of 25 Hz and lower with motor load. Table 1 gives the theoretical as well as the experimental
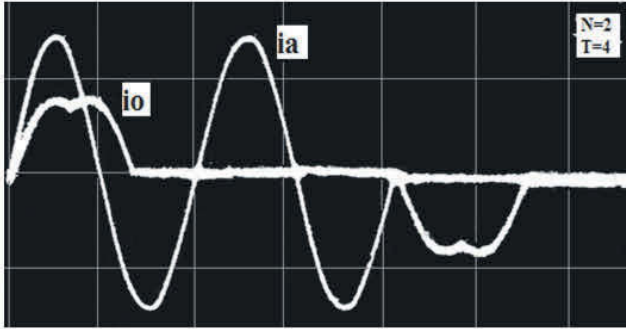
Fig. 14: Phase load current i_0 and supply phase current i_a waveforms of the converter loaded with R−load. Scale: current i_a 1A/Div. Current i_0 2A/Div. Horiz. 10 ms/Div.
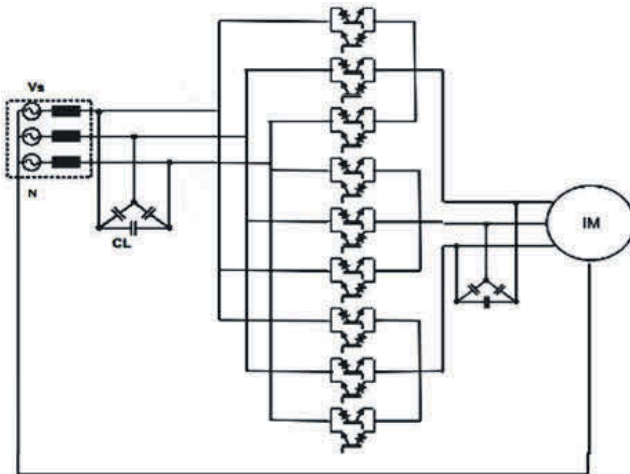
Fig. 15: Three-phase to three-phase converter supplying a star-connected three-phase induction motor.

Tab. 1: Motor performance with some desired frequencies produced by the proposed frequency changer.

T	2	3	4	5
Theoretical desired frequency (Hz)	25	16.6	12.5	10
Theoretical desired shaft speed (r.p.m.)	1468	979	734	587
Actual shaft speed measured experimentally (r.p.m.)	1467	978	727	576
Corresponding Actual operating frequency (Hz)	24.97	16.65	12.37	9.8
Mechanical vibration noticed experimentally	Very Low	Very Low	Low	Low

results for the converter performance with the three-phase induction motor for $N = 1$ and variable T.

With small values of T, the mechanical vibration was very low and the converter showed excellent performance. As T becomes larger the mechanical vibration is increased to some extent. This is because the output frequency is low as well as the dead time in the output current wave becomes large, (see Fig. 12), so the torque produced is less.

6 Conclusion

A new technique of power frequency changing using power transistors is explained. This technique exploits the principle of mixing amplitude modulated current waveforms to obtain power frequency division. The initial investigation of this type of frequency changing technique shows that it exhibits very good power frequency conversion efficiency and low harmonic content current (voltage) waveforms. The quality of the output current, waveform can largely be improved by using multi-phase supply system.

Different versions of converter circuits were built and tested in the laboratory. The results confirm both the principles and theoretical prediction of the performance. The converter accommodates all types of loads for three-phase control and considered as a current source cycloconverter (CSC).

Bibliography

[1] L. Gyugi, and B.R. Pelly. Static Power Frequency Changers, John Wiley and Sons, New York, USA, 1976.

[2] I. Yamato et al. High frequency link DC-AC converter for UPS with a new voltage clamper, Proc. IEEE Power Electronics Specialists Conf., :749–756, 1990.

[3] H. Fujimoto, K. Kuroki, T. Kagotani and H. Kidoguchi. Photovoltaic inverter with a novel cycloconverter for interconnection to a utility line, Proc. IEEE Industry Application Conf., USA, 3:2461–2467, 1995.

[4] M. Matsui, M. Nagai, M. Mochizuki and A. Nabae. High-frequency link DC to AC converter with suppressed voltage clamp circuits naturally commutated phase angle control with self turn-off devices, IEEE Trans. on Industry Applications, 32(2):293–300, 1996.

[5] E. Koutroulis, J. Chatzakis, K. Kalaitzakis and N. C. Voulgaris . A bidirectional, sinusoidal, high-frequency inverter design. IEE Proc. Electric Power Applications, 148(4):315–321, 2001.

[6] P.G. Barbosa, H.A.C. Braga, M.C.B. Rodrigues, M.C.B., and E.C.Teixeira. Boost current multilevel inverter and its application on single-phase grid-connected photovoltaic systems. IEEE trans. Power Electronics, 21(4):1116–1124, 2006

[7] E.H.E. Bayoumi,A. Maamoun, O. Pyrhönen,M.O. Khalil, and A. Mhfouz. Enhanced method for controlling PWM converter-inverter system. Proc.of the IASTED International Conf. of Power and Energy Systems, PES'02, California, USA, :425–430, May 2002.

[8] E.H.E. Bayoumi. Analysis and design of linear and variable structure control techniques for PWM rectifier. Electromotion Scientific Journal, 11(4):205–212, October-December, 2004.

[9] M.S.M Khasbak. Integral-cycle based cycloconverter with voltage control using PWM technique. Ph.D Thesis, Nahrain University - Iraq, 2007.

[10] M.T. Lazim and M.A. Zeidan. Power frequency changer using bi- phase integral cycle control technique. Journal of Electrical Engineering [Online], 13(3), 2013, (www.jee.com).

[11] M. Glab. Z. Krezminski and A. Lewicki. Multiscaler control of induction motor supplied by current source inverter. Conf. PCIM2007, Nurenberg, 2007.

[12] A. Kwak and H.A. Toliyat. A current source inverter with advanced external control circuit method. IEEE Trans. on Industry Application, 42(6):1496–1507, 2006 .

[13] M.T . Lazim and W. Shepherd. Low frequency modulation properties of thyristor circuits. Journal of Franklin Institutes, 312(6):373–397, 1981.

Biographies

Mohammed Tawfiq Lazim graduated from Engineering College, University of Baghdad, Iraq in 1967. He received the M.Sc. degree in from University of Baghdad, Iraq in 1975 and the Ph.D in electrical and electronics engineering from the university of Bradford, West Yorkshire, England in 1981, all in electrical and electronics engineering. He was assistant professor and head of electrical and electronics engineering department at the Military Engineering College, Iraq from 1981 to 1991 and head of computer engineering department at the Mansoor University, Iraq from 1991 to 1999. He worked at the Nahrain University, Baghdad, Iraq as associate professor and head of electronics and communication engineering department from 1999 to 2007.He joined the Faculty of Engineering, Philadelphia University, Jordan in 2007, and is now Professor of Electrical and Power Electronics Applications in the electrical engineering department. He is the author of four books and translator to Arabic of thee books.

Audih Al Faoury was born in Sult-Jordan. He received M.Sc. and Ph.D. degrees in electrical engineering from Cluj Napoca Technical University-Romania 1990 and 1995 respectively. He worked at the Ministry of Energy and Minerals Resources (MEMR) 1997 until 2004 during this period he worked in many area of inters such as preparation contracts, studies, analysis and review regulation in distribution, transmission and generation systems in Jordan. He was also an participant of JICA team for one year to analysis and recommendations of distribution power system in Jordan. He is member of IET. From 2004 to 2015 he is pursuing an academic track at Philadelphia University and occupied head of electrical department for two times Including teaching in the power field Recently he is assistant dean of engineering faculty of Al Balqa Applied University and a staff member of power and energy department and teaching all courses in power system such as protection, operation, transmission lines design, stability and reliability, electromagnetics as well as power system analyses.

E. Ponce, L. Benadero and A. El Aroudi

Bifurcation Analysis in a Self-Oscillating Series Resonant Converter

Abstract: In this paper, the dynamics of a dc-ac resonant self-oscillating LC series inverter is analyzed from the point of view of piecewise smooth dynamical systems. The system under study is defined by two symmetric configurations and its bifurcation analysis is performed in a one dimensional parameter space. This analysis reveals that a non smooth transition takes place between two strongly different dynamical behaviors. The first one is an oscillating regime, which is the one used in applications and it involves a repetitive switching sequence between the system configurations. This behavior is exhibited whenever the open loop equilibrium corresponding to the system configurations are foci. The second one is a non desired stationary regime corresponding to the equilibrium points of node type whose stable manifolds preclude the appearance of oscillations.

1 Introduction

Resonant converters have been investigated for many years and they are still receiving attention from power electronics community [1, 2]. They have been used to reduce the switching losses in many industrial applications involving switched mode power supplies such as in lighting [3], induction heating [4, 5], battery charging [6] and wireless power transfer [7] among others. Roughly speaking, there are three basic types of the resonant converters: series resonant converters, parallel resonant converters and series-parallel resonant converters. Zero current switching is a common method of controlling the output voltage in resonant converters [8]. Due to its simple circuit topology and control system, the series resonant converter is widely used in many applications [9].

In series resonant inverters, the resonant tank is formed by a series LC circuit as seen in Fig. 1, which shows the circuit diagram of the system considered in this study. The LC tank and the load are also connected in series and hence it works as

---

E. Ponce, L. Benadero and A. El Aroudi: E. Ponce, University of Seville, Spain,
email: eponcem@us.es L. Benadero, Polytechnic University of Catalonia, Spain,
email: luis.benadero@upc.edu A. El Aroudi, University of Rovira i Virgili, Spain,
email: abdelali.elaroudi@urv.cat
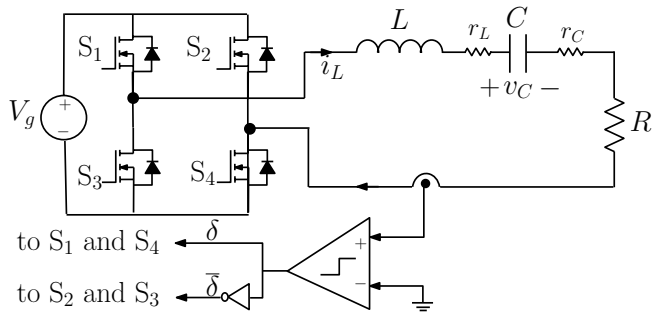
Fig. 1: Schematic diagram of the LC series resonant inverter.

a voltage divider since the voltage gain is always lower than one. Although, this is a clear disadvantage of this inverter topology together with many others, there are many advantages of series resonant converters such as a the existence of a DC current blocking capacitor and the associated good efficiency due to reduced conduction losses.

Currently, resonant inverters are knowing renewed interest and are substituting their non-resonant counterparts due to the simplicity and straightforwardness of their working principle. Namely, whenever the current reaches zero, the control signal is switched. This working mode leads to variable switching frequency which can vary in a wide range. The variable frequency operation and large harmonic content of the state variables make conventional modeling techniques no longer applicable and this pose serious problems for their modeling and stability analysis using conventional averaging procedures largely used in switched mode power supply design. While averaged models are only accurate for switching frequency well above the system bandwidth, the switching frequency in resonant inverters is close to the resonant tank. Hence, in spite of the simplicity of the circuit topologies used and the control mechanism, the mathematical description of the self-oscillating mode leads to piecewise models that could exhibit complex dynamical behaviors.

State space analysis techniques have been used in [10] for optimal trajectory control. Some other advanced smooth techniques have been used to describe the dynamical behavior of such systems. For instance, in [5], first harmonic approximation and order reduction were followed by assuming slowly varying amplitude and phase with the aim to obtain simple analytical model of resonant inverters. In [11], phasor transformation was applied to analyze series resonant converters. In [12] a describing function-based analysis is used to predict the steady-state behavior of a resonant converter. Hamel locus is presented in [13] to determine the mode of oscillation of a resonant LCL converter under a self-oscillating hysteretic controller for a given value of the hysteresis width. In [7], a method based on a stroboscopic mapping model is presented for accurately determining all possible steady-state operating points of a switch mode LCL WPT resonant converter. A similar approach was used in [14, 15] and

recently in [1] to study the stability of induced limit cycles in a series resonant DC-DC power converter and a parallel LC resonant inverter respectively. In [1], self-oscillating resonant inverter uses a simple control, whose input is the inductor current so that the two switching branches are alternatively activated. Although the previous approaches are enough accurate for high enough quality factors, their accuracy decreases when this parameter decreases.

In this paper, we deal with the bifurcation analysis of an LC series resonant inverter, following the same approach used in [16] for its LC parallel counterpart. We put in evidence some relevant differences between these two implementations from the point of view of nonlinear dynamics and bifurcation of limit cycles, which are mainly related to the location of the equilibria regarding the switching manifold. In particular, we show that sliding orbits responsible for the coexistence of multiple limit cycles in parallel resonant inverters, can not exist in series resonant inverters and these are therefore free from this undesired behavior.

The rest of the paper is organized as follows. Section 2 presents the mathematical switched model of the system and its normalization, thus resulting in a unique bifurcation parameter. In section 3, we show that the local linear transition of the open loop equilibrium from spiral to node further implies a non smooth global bifurcation, thus inhibiting the desired oscillatory mode of the converter. Some notes regarding merit figures of interest in applications are given in Section 4 and, finally, concluding remarks are drawn in the last section.

2 System description and mathematical Modeling

Figure 1 shows the circuit diagram of the system considered in this study that is an LC series resonant inverter. The circuit parameters, which can be identified in this circuit are: C the capacitance of the output capacitor with ESR r_C, L the inductance of the inductor with winding resistance r_L, R the load resistance, and V_g the input source voltage. The switches S_1 and S_4 are in the ON state when $i_L > 0$ ($\delta = 1$), and they are turned OFF when $i_L < 0$ ($\delta = 0$). The switches S_2 and S_3 are driven in a complementary way to S_1 and S_4. Notice that the system is autonomous, i.e., the switching action is not explicitly time dependent.

By applying KVL and considering the control condition, the dynamical model of the system defined by the diagram in Fig. 1 is as follows:

$$\frac{\mathrm{d}}{\mathrm{d}t}\begin{pmatrix} v_C \\ i_L \end{pmatrix} = \begin{pmatrix} 0 & \dfrac{1}{C} \\ -\dfrac{1}{L} & -\dfrac{R_s}{L} \end{pmatrix}\begin{pmatrix} v_C \\ i_L \end{pmatrix} + \begin{pmatrix} 0 \\ \dfrac{V_g}{L} \end{pmatrix}, \qquad (1)$$

$$h(v_C, i_L) = i_L, \qquad (2)$$

where $R_s = R + r_C + r_L$ is the equivalent series resistance of the circuit. Besides, the capacitor voltage v_C and the inductor current i_L are the state variables of the system.

In order to simplify these expressions by reducing the number of parameters, let us introduce the natural frequency ω_0, the characteristic impedance Z_0 and quality factor Q of the LCR resonant series circuit, which are given by the following expressions

$$\omega_0 = \sqrt{\frac{1}{LC}}, \quad Z_0 = \sqrt{\frac{L}{C}}, \quad Q = \frac{Z_0}{R_S}.$$

Then, by defining a new time τ and state vector $\mathbf{x} = (x_1, x_2)^\mathsf{T}$ as follows

$$\tau = \omega_0 t, \quad x_1 = \frac{v_C}{V_g}, \quad x_2 = \frac{i_L Z_0}{V_g},$$

system equations (1)-(2) get the simplified form

$$\frac{d\mathbf{x}}{d\tau} = A\mathbf{x} + \mathbf{b}u, \tag{3}$$

$$h(\mathbf{x}) = \mathbf{c}^\mathsf{T}\mathbf{x}, \tag{4}$$

where $\mathbf{c}^\mathsf{T} = (0, 1)$, and the matrix A and the vector $\mathbf{b}$ are

$$A = \begin{pmatrix} 0 & 1 \\ -1 & -\dfrac{1}{Q} \end{pmatrix}, \quad \mathbf{b} = \begin{pmatrix} 0 \\ 1 \end{pmatrix}.$$

Note that the open loop system (3), in which the switch variable u remains constant, either $u = 1$ or $u = -1$, has as unique attractor the equilibrium point $\bar{\mathbf{x}} = (u, 0)^\mathsf{T}$.

The eigenvalues of the matrix A are

$$p^\pm = -\frac{1}{2Q} \pm \sqrt{\frac{1}{4Q^2} - 1},$$

and it can be deduced, due the physical restriction $Q > 0$, which implies eigenvalues with negative real part, that the open loop equilibrium is always stable. However, there is a minor transition at $Q = 1/2$, because the eigenvalues change from real to complex values. If $Q > 1/2$, the two eigenvalues are complex conjugated, so that the equilibrium is surrounded by spiraling trajectories. Otherwise, if $Q \le 1/2$, the equilibrium is a node, and therefore, the orbits tend to the stable manifold corresponding to the eigenvector associated to the highest or to the lowest eigenvalue considering forward or backward time evolution respectively. Unlike in the linear system, we will prove that in our piecewise smooth system (3)-(4), a non trivial non smooth bifurcation is produced at the same value $Q = 1/2$.

3 Piecewise smooth analysis

3.1 The switching manifold and the sliding subset

Recall that from (4), the switching manifold is defined here as $\Sigma = \{\mathbf{x} : x_2 = 0\}$, thus splitting the phase in plane in two regions $\Sigma^- = \{\mathbf{x} : x_2 < 0\}$ and $\Sigma^+ = \{\mathbf{x} : x_2 > 0\}$. Accordingly, system (3)-(4) can also be expressed as follows

$$\frac{\mathrm{d}\mathbf{x}}{\mathrm{d}\tau} = \mathbf{F}(\mathbf{x}) = \begin{cases} \mathbf{F}^+(\mathbf{x}) = (F_1^+(\mathbf{x}), F_2^+(\mathbf{x}))^\mathsf{T} = A\mathbf{x} + \mathbf{b}, \ \mathbf{x} \in \Sigma^+, \\ \mathbf{F}^-(\mathbf{x}) = (F_1^-(\mathbf{x}), F_2^-(\mathbf{x}))^\mathsf{T} = A\mathbf{x} - \mathbf{b}, \ \mathbf{x} \in \Sigma^-. \end{cases} \tag{5}$$

Following to the Filippov theory [17], sliding dynamics can occur in a subset Σ_S of the switching manifold Σ, if the vector fields $\mathbf{F}^+$ and $\mathbf{F}^-$ satisfy the condition

$$\Sigma_S = \left\{ \mathbf{x} \in \Sigma : (\nabla h(\mathbf{x}) \cdot \mathbf{F}^+(\mathbf{x})) \, (\nabla h(\mathbf{x}) \cdot \mathbf{F}^-(\mathbf{x})) < 0 \right\}, \tag{6}$$

in which $\nabla(\cdot)$ is the gradient operator. This means that in a sliding region, the vector field points inwards or outwards at both sides of Σ_S. Conversely, in the points not belonging to Σ_S, the vector field crosses Σ. Roughly speaking, three different cases of switching dynamics can exist, one of them corresponding to simple crossing associated to Carathéodory solutions. The other two cases are the attracting and the rejecting sliding motions.

In our case, the field $\mathbf{F}^+$ and $\mathbf{F}^-$ points outwards Σ_S, so the sliding set is repelling and turns out to be the subset $\Sigma_S = \{\mathbf{x} : -1 < x_1 < 1, x_2 = 0\}$. In fact, the two vector fields are anti-collinear at any point in Σ_S, so that the corresponding Filippov vector field is identically zero and there is no proper sliding dynamics, since all the points are non isolated unstable pseudo-equilibrium points. This fact excludes the existence of limit cycles involving a sliding dynamics, in a clear contrast to the parallel resonant converter, in which unstable limit cycles, partially with a sliding dynamics, can take place. More details concerning the existence conditions and the implications of these limit cycles in the parallel resonant converter can be found in [18].

3.2 The non oscillatory dynamics

We deal first with the non oscillatory dynamics. Actually, this is a non desired operation of the converter in real applications, which occurs under the over damping condition, that is in the parameter domain $0 < Q \leq 1/2$. This case is illustrated in Fig. 2(a) using $Q = 0.4$, where some ad hoc trajectories have been depicted. If $0 < Q \leq 1/2$, the eigenvalues of the matrix A are real and negative, and so the dynamics evolving around each equilibrium cannot cross their corresponding stable manifolds. The consequence of this fact is that for any arbitrary trajectory, at most

(a) $Q = 0.4 < \frac{1}{2}$　　　　　(b) $Q = 1.5 > \frac{1}{2}$
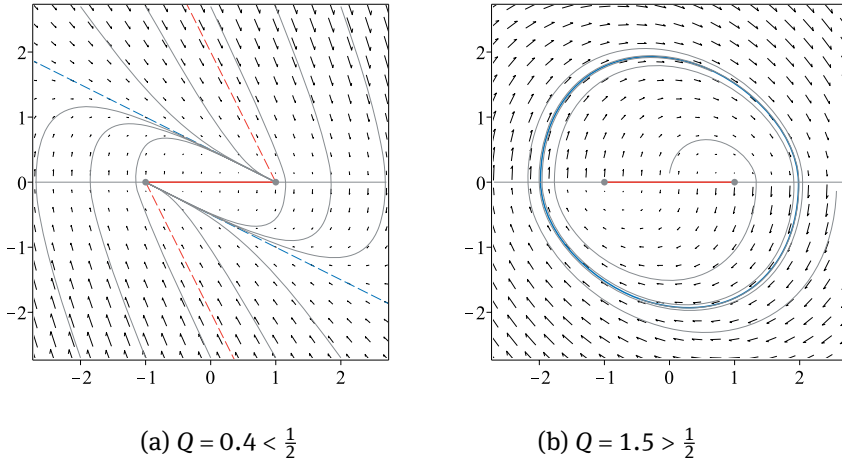
Fig. 2: State diagrams for system (3)-(4) under parameter $Q = 0.4 < 1/2$ in (a), and $Q = 1.5 > 1/2$ in (b). Note in (a) the boundaries of the attraction basin of the twin equilibria (blue points), defined by the rejecting sliding segment and the eigenvectors corresponding to the lowest eigenvalue (red lines). Conversely, in (b), the dynamics is oscillatory, thus converging to a limit cycle (in blue color) defined by two half cycles connected each other.

only one switching can be produced and therefore, the oscillating regimen cannot be attained. The boundary of attraction between the twin equilibrium points, which is also depicted in Fig. 2(a) using red color, is made up of three pieces: the sliding subset Σ_S and the part of stable manifold corresponding to the lowest (more negative) eigenvalue in the valid side of the state plane for each equilibrium. Note that from each pseudo-equilibrium point of the sliding sets two heteroclinic orbits emanate [19], one to the point $(-1, 0)$ and the other to the point $(1, 0)$. Thus, there are infinitely many heteroclinic orbits to these two singular points. Furthermore, we must consider two additional heteroclinic orbits that forms a closed path, joining the two singular points.

After the non-smooth bifurcation that occurs at $Q = 1/2$, that is for $Q > 1/2$, all the heteroclinic orbits are destroyed and one stable limit cycle bifurcates from the above closed path, as shown below.

3.3 The self oscillating dynamics

In the following, we consider the quality factor restricted to the range $Q > 1/2$. Then, system (3)-(4) has an oscillatory dynamics, the one useful for industrial applications. Notice that for the linear case (3), with either $u = 1$ or $u = -1$, we have naturally a focus dynamics converging to an equilibrium, so that the self sustained oscillation is enabled by the switching action introduced in (4). To prove this, let us choose an initial point located in the upper half plane. Because the trajectory evolves clockwise around

the right side equilibrium $\bar{\mathbf{x}}^+ = (1, 0)$, it will necessarily cross Σ at a point $(x_1 > 1, x_2 = 0)$. Then, the trajectory enters the lower half plane, so evolving around the left side equilibrium $\bar{\mathbf{x}}^- = (-1, 0)$ to reach and cross Σ again at a point $(x_1 < -1, x_2 = 0)$. This process is repeated indefinitely, thus converging the trajectory to a finite limit cycle, which is the desired oscillatory dynamics.

To study the stable limit cycle, it is very convenient (see [20–22]) to introduce the bifurcation parameter γ as the real and the imaginary part ratio for the focus eigenvalue p^+, so that

$$p^+ = -\frac{1}{2Q} + i\sqrt{1 - \frac{1}{4Q^2}} = \sigma + i\omega_r = \sigma\left(1 + \frac{i}{\gamma}\right),$$

in which

$$\gamma = \frac{\sigma}{\omega_r} = -\frac{1}{\sqrt{4Q^2 - 1}} < 0.$$

Thus, if we take the new time and variables $\theta = \omega_r\tau$, $y_1 = x_1$, $y_2 = \omega_r x_2$, and take into account that $\omega_r^{-2} = \gamma^2 + 1$, we obtain from (3)-(4) the normalized system

$$\frac{d\mathbf{y}}{d\theta} = \begin{pmatrix} 0 & \gamma^2 + 1 \\ -1 & 2\gamma \end{pmatrix}\mathbf{y} + \begin{pmatrix} 0 \\ 1 \end{pmatrix}u, \tag{7}$$

$$h(\mathbf{y}) = \mathbf{c}^\mathsf{T}\mathbf{y}, \tag{8}$$

in which $\mathbf{y} = (y_1, y_2)^\mathsf{T}$ is the redefined vector state. Accordingly, the switching manifold and the two involved partitions are redefined as $\Sigma = \{\mathbf{y} : y_2 = 0\}$, $\Sigma^- = \{\mathbf{y} : y_2 < 0\}$ and $\Sigma^+ = \{\mathbf{y} : y_2 > 0\}$. Furthermore, the two corresponding focus are $\bar{\mathbf{y}}^\pm = (\pm 1, 0)$.

Taking into account the symmetry of the vector field with respect to the origin, we focus our attention on to the half-plane Σ^+, where $u = 1$ with corresponding attractor $\bar{\mathbf{y}}^+ = (1, 0)$. Thus, solving equation (7) with $u = 1$, we get

$$\begin{pmatrix} y_1(\theta) - 1 \\ y_2(\theta) \end{pmatrix} = e^{\gamma\theta}\begin{pmatrix} \cos\theta - \gamma\sin\theta & (\gamma^2 + 1)\sin\theta \\ -\sin\theta & \cos\theta + \gamma\sin\theta \end{pmatrix}\begin{pmatrix} y_1(0) - 1 \\ y_2(0) \end{pmatrix}. \tag{9}$$

Since we are dealing with orbits for $y_2 \geq 0$ starting at Σ and returning to Σ at time θ_1 after surrounding the focus, we can write $y_2(0) = y_2(\theta_1) = 0$ in (9) thus resulting $\theta_1 = \pi$. This simple solution reflects the fact that any orbit running from Σ to Σ around the focus, will last exactly half time of the cycle corresponding to the linear system, because both focus are at Σ itself. Imposing also the symmetry condition $y_1(\theta_1) = -y_1(0)$, we obtain after some algebra an expression for the amplitude of the limit cycle, as its crossing point at Σ, namely

$$Y_1 = y_1(\theta_1) = \coth\left(-\frac{\gamma\pi}{2}\right).$$

In Fig. 3, the value Y_1 of the normalized variable y_1 at the switching condition is represented versus the two parameters γ and Q. It is worth noting that if the quality

factor is high enough, the expression $Y_1 \approx 4Q/\pi$ is a reasonable approximation for the amplitude of the steady oscillation. Also, if γ is made negative enough, Y_1 converges to its lowest value $Y_1 = 1$. In Fig. 4, the normalized values (y_1, y_2) for one cycle of the steady state oscillation have been represented for two different parameters $Q = 5$ ($\gamma = -0.3535$) and $\gamma = -1$ ($Q = 0.7071$).

(a) $Y_1(\gamma)$ (b) $Y_1(Q)$
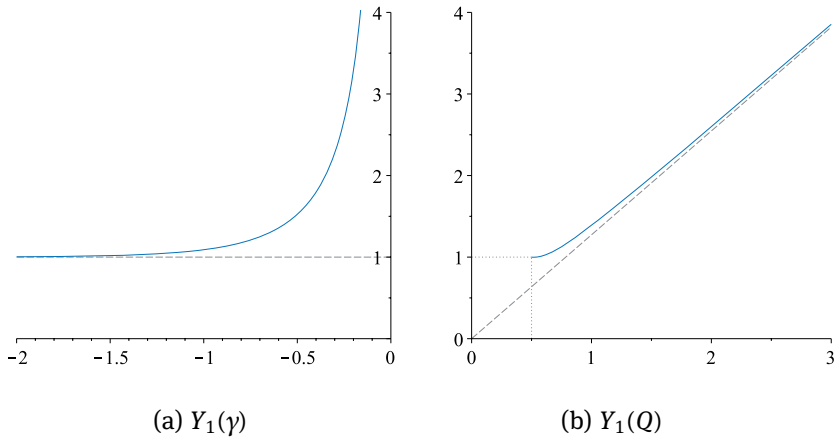
Fig. 3: Amplitude Y_1 of the limit cycle versus γ in (a) and versus Q in (b). The gray dashed lines are the asymptotes to which the amplitude tends for high absolute values of the corresponding parameter.

(a) $Q = 5$ ($\gamma = -0.3535$)   (b) $Y_1(Q)\gamma = -1$ ($Q = 0.7071$)
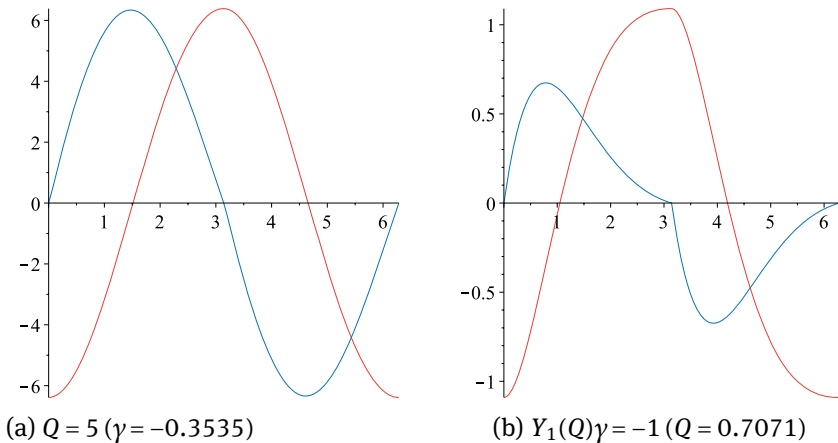
Fig. 4: Limit cycle waveforms with $y_1(\theta)$ in red color and $y_2(\theta)$ in blue color, with parameters specified in the caption.

4 Some features concerning applications

Focusing on applications, let us define a new variable y_R to account for the relative load voltage. Thus, recalling that $y_2 = \omega_r i_L Z_0 / V_g$ and considering the voltage divider relation $\alpha = R/R_S$ between the load R and the series equivalent R_S, we deduce that

$$y_R = \frac{i_L R}{V_g} = \frac{\alpha y_2}{\omega_r Q} = -2\alpha\gamma y_2. \tag{10}$$

Using one of the two symmetrical half cycles in the steady state, we deduce from (9) the expression $y_2(\theta) = (1 + Y_1)\mathrm{e}^{\gamma\theta} \sin\theta$, and then $y_R(\theta;\gamma) = Y_R(\gamma)g(\theta;\gamma)$ follows, in which Y_R is a sort of amplitude and g takes care of the dependence on time for $0 \le \theta \le \pi$. These terms are

$$Y_R(\gamma) = -2\alpha\gamma\left(1 - \coth\frac{\gamma\pi}{2}\right), \quad g(\theta;\gamma) = \mathrm{e}^{\gamma\theta} \sin\theta.$$

From these expressions, it is then possible to evaluate the peak value $\overline{Y}_R(\gamma)$ and the root mean square (rms) value $\widetilde{Y}_R(\gamma)$ for $y_R(\theta;\gamma)$. To achieve this, we proceed to calculate these items for $g(\theta;\gamma)$. Considering the instant $\theta_0(\gamma) = \cot^{-1}(-\gamma)$ at which $g(\theta;\gamma)$ is maximal and the integral of $g^2(\theta;\gamma)$ in a half cycle (from $\theta = 0$ to $\theta = \pi$), with the result $(\mathrm{e}^{2\gamma\pi} - 1)(4\gamma(\gamma^2 + 1))^{-1}$, we get after some algebraic manipulations

$$\overline{Y}_R(\gamma) = \frac{-2\alpha\gamma\left(1 - \coth\frac{\gamma\pi}{2}\right)\mathrm{e}^{\gamma\cot^{-1}(-\gamma)}}{\sqrt{\gamma^2 + 1}},$$

$$\widetilde{Y}_R(\gamma) = \alpha\left(1 - \coth\frac{\gamma\pi}{2}\right)\sqrt{\frac{-\gamma(1 - \mathrm{e}^{2\gamma\pi})}{\pi(\gamma^2 + 1)}}.$$

In Fig. 5, the peak $\overline{Y}_R$ and rms $\widetilde{Y}_R$ values are represented in terms of both parameters γ and Q, considering an ideal divider $\alpha = 1$. Notice the asymptotic behavior of $\overline{Y}_R$ for $\gamma \to -\infty$ ($Q \to 1/2$) and for $Q \to \infty$ ($\gamma \to 0$), thus giving $\overline{Y}_R = 4/\mathrm{e}$ and $\overline{Y}_R = 4/\pi$ respectively. Also, $\widetilde{Y}_R$ tends to $4/\sqrt{2\pi}$ if $Q \to \infty$ and to a null value if $\gamma \to -\infty$. We then conclude that function $y_R(\theta)$ approaches more to the ideal harmonic case as the quality factor increases. On the contrary, though the oscillation is sustained whenever $Q > 1/2$, this function progressively tends to a narrow pulse shape if Q tends to that limit value, thus degrading the inverter efficiency in terms of energy delivered to the load (see Fig. 4(b) and red lines for $\widetilde{Y}_R$ in Fig. 5).

Finally, taking into account that due to the symmetry all even harmonics vanish, the total harmonic distortion (THD) is defined and then calculated as

$$\mathrm{THD} = 100\sqrt{\frac{P_T}{P_1} - 1} = 100\sqrt{\frac{\pi\gamma(\gamma^2 + 4)\coth\frac{\pi\gamma}{2}}{8(\gamma^2 + 1)} - 1},$$

(a) $\overline{Y}_R(\gamma)$ and $\widetilde{Y}_R(\gamma)$ (b) $\overline{Y}_R(Q)$ and $\widetilde{Y}_R(Q)$
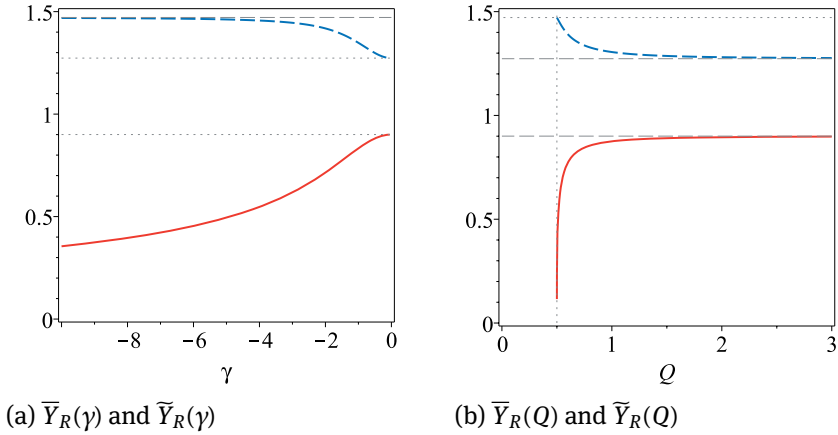
Fig. 5: Peak $\overline{Y}_R$ and rms $\widetilde{Y}_R$ values using a dashed blue line and a continuous red line respectively, in front of parameter γ in (a) and parameter Q in (b). The gray dashed lines are the asymptotes to which these values tend for high absolute values of the corresponding parameter.
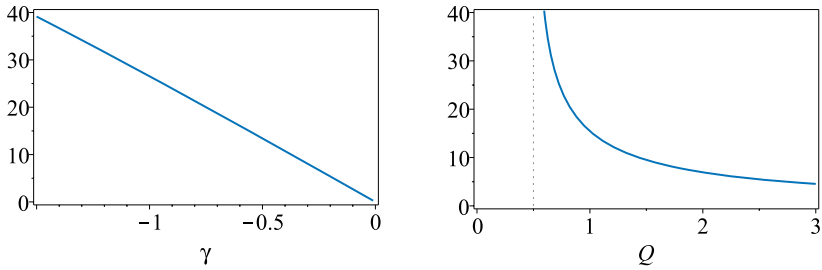
Fig. 6: THD versus parameter γ in (a) and versus parameter Q in (b).

where both P_T and P_1 stand for output power averages, but considering the full signal or only the first harmonic for P_T or P_1 respectively. Notice that the expression given above can be obtained by appropriate time integrations of the function $g(\theta; \gamma)$. The harmonic distortion is represented in the two diagrams in Fig. 6 in front of both parameters γ and Q. Obviously, from the point of view of distortion, the performance of the inverter is also degraded for low values of the quality factor.

5 Concluding Remarks

The dynamics of a self-oscillating zero current switching dc-ac LC series resonant inverter was analyzed in this paper. At the critical value of the quality factor $Q =$

1/2, for which there is a transition from non-spiral to spiral dynamics in the open loop system, a dramatic bifurcation occurs. This non-smooth bifurcation implies a transition from a bi-stable behavior with a pair of symmetric equilibrium points if $Q \leq 1/2$ to the desired oscillatory dynamics if $Q > 1/2$.

Such bifurcation is associated here to the simultaneous destruction of infinitely many heteroclinic orbits that determine a bounded set. This behavior is different from the appearing in the parallel resonant inverter, for which the transition from equilibrium to oscillation involves unstable limit cycles, see [16, 23] and also [18] for a generalized version of the circuit here considered, along with the corresponding bifurcation analysis.

Acknowledgment

Bibliography

[1] R. Bonache-Samaniego, C. Olalla and L. Martínez-Salamero. Design of self-oscillating resonant converters based on a variable structure systems approach. *IET Power Electronics*, 57(1):111–119, 2015.

[2] R. Bonache-Samaniego, C. Olalla and L. Martínez-Salamero. Dynamic Modeling and Control of Self-Oscillating Parallel Resonant Converters Based on a Variable Structure Systems Approach. *IEEE Trans. on Power Electronics*, 32(2):1469–1480, 2017.

[3] P. D. Teodosescu, M. Bojan and R. Marschalko. Resonant LED driver with inherent constant current and power factor correction. *Electronics Letters*, 50(15):1086–1088, 2014.

[4] A. Kumar, M. Sadhu, N. Das, P. K. Sadhu, D. Roy and A. Ganguly. A Survey on High-Frequency Inverter and Their Power Control Techniques for Induction Heating Applications. *Journal of Power Technologies*, 97(3):201–213, 2017.

[5] A. Dominguez, L. A. Barragan, J. I. Artigas, A. Otin, I. Urriza and D. Navarro. Reduced-Order Models of Series Resonant Inverters in Induction Heating Applications. *IEEE Trans. on Power Electronics*, 32(3):2300–2311, 2017.

[6] J. Deng, S. Li, S. Hu, C. C. Mi and R. Ma. Design Methodology of LLC Resonant Converters for Electric Vehicle Battery Chargers. *IEEE Trans. on Vehicular Technology*, 63(4):1581–1592, 2014.

[7] C. S. Tang, Y. Sun, Y. G. Su, S. K. Nguang and A. P. Hu. Determining multiple steady-state ZCS operating points of a switch-mode contactless power transfer system. *IEEE Trans. on Power Electronics*, 24(2):416–425, 2009.

[8] J. Park, M. Kim and S. Choi. Zero-current switching series loaded resonant converter insensitive to resonant component tolerance for battery charger. *IET Power Electronics*, 7(10):2517–2524, 2014.

[9] R. W. Erickson and D. Maksimovic. *Fundamentals of Power Electronics*. Springer, 2nd edition, 2001.

[10] S. Feng. *Optimal Trajectory Control of Series Resonant Converter*. PhD thesis, Lakehead University, Canada, 2001.

[11] C. T. Rim and G. H. Cho. Phasor transformation and its application to the DC/AC analyses of frequency phase-controlled series resonant converters (SRC). *IEEE Trans. on Power Electronics*, 5(2):201–211, 1990.

[12] H. Pinheiro, P. K. Jain and G. Joos. Self-sustained oscillating resonant converters operating above the resonant frequency. *IEEE Trans. on Power Electronics*, 14(5):803–815, 1999.

[13] D. Williams, C. Bingham, M. Foster and D. Stone. Hamel locus design of self-oscillating DC-DC resonant converters. *IET Power Electronics*, 3(1):86–94, 2010.

[14] V. M. Hernandez, R. Silva and H. Sira-Ramirez. On the stability of limit cycles in resonant DC-to-DC power converters. 42nd *IEEE Conf. on Decision and Control*, 1141–1146, 2003.

[15] O. Dranga, B. Buti, and I. Nagy. Stability analysis of a feedback-controlled resonant DC-DC converter. *IEEE Trans. on Industrial Electronics*, 50(1):141–152, 2003.

[16] E. Ponce, L. Benadero, A. El Aroudi and L. Martínez-Salamero. Sliding Bifurcations in Resonant Inverters. 14th *Int. Multi-Conf. on Systems, Signals and Devices*, :122–127, Marrakech-Morocco, 28-31 March 2017.

[17] A. F. Filippov. *Differential Equations with Discontinuous Right-hand Sides*. Kluwer Academic Publishers, Dortrecht, 1998.

[18] L. Benadero, E. Ponce, A. El Aroudi and F. Torres. Limit cycle bifurcations in resonant LC power inverters under zero current switching strategy. *Nonlinear Dynamics*, 91(2):1145–1161, 2018.

[19] L. P. Shilnikov. Homoclinic orbits: Since Poincaré till today. preprint No. 571, WIAS, Berlin, 2000.

[20] A. A. Andronov, A. A. Vitt and S. E. Khaikin. *Theory of Oscillators*. Pergamon Press, Oxford, 1966.

[21] E. Freire, E. Ponce and F. Torres. Canonical discontinuous planar piecewise linear systems. *SIAM J. Appl. Dynamical Systems*, 20(11):181–211, 2012.

[22] E. Freire, E. Ponce and F. Torres. A general mechanism to generate three limit cycles in planar Filippov systems with two zones. *Nonlinear Dynamics*, 78:251–263, 2014.

[23] L. Benadero, E. Ponce, A. El Aroudi and L. Martínez-Salamero. Analysis of coexisting solutions and control of their bifurcations in a parallel LC resonant inverter. *2017 IEEE Int. Symp. on Circuits and Systems (ISCAS)*, 2017.

Biographies

Enrique Ponce was born in Seville, Spain, on July 2, 1955. He received the Ingeniero Industrial and Doctor Ingeniero Industrial degrees from the University of Seville, Seville, Spain, in 1978 and 1987, respectively. Since 1978, he has been with the Department of Applied Mathematics at the University of Seville, where he is currently a Professor. His research interests are nonlinear oscillations, bifurcations and piecewise linear systems, with emphasis on applications in nonlinear control and electronics.

Luis Benadero was born in Ciudad Real, Spain, in 1952. He received the Ph.D. degree from the Universitat Politècnica de Catalunya (UPC), Catalonia, Barcelona, in 1983. He is Associate Professor, at the same university, with the Applied Physics Department and formerly he was with the Department of Electronic Engineering. His research activity is related to nonlinear phenomena, currently mainly focused in nonlinear dynamics, more specifically dealing with piecewise smooth systems. Such systems have an important application in power electronics, subject in which he has published several papers in the two last decades.

Abdelali El Aroudi received the graduate degree in physical science from Faculté des sciences, Université Abdelmalek Essaadi, Tetouan, Morocco, in 1995, and the Ph.D. degree (hons) in applied physical science from Universitat Politècnica de Catalunya, Barcelona, Spain in 2000. During the period 1999-2001 he was a Visiting Professor at the Department of Electronics, Electrical Engineering and Automatic Control, Technical School of Universitat Rovira i Virgili (URV), Tarragona, Spain, where he became an associate professor in 2001 and a full-time tenure Associate Professor in 2005. His research interests are in the field of structure and control of power conditioning systems for autonomous systems, power factor correction, stability problems, nonlinear phenomena, chaotic dynamics, bifurcations and control. He is a Guest Editor of the *IEEE Journal on Emerging and Selected Topics in Circuits and Systems* Special Issue on Design of Energy-Efficient Distributed Power Generation Systems (September 2015). He currently serves as Associate Editor in *IEE IET Power Electronics* and *IEE IET Electronics Letters*.

R. Ben Ayed

Optimal design targeting the environmental footprint reduction of an electrical railway subsystem

Abstract: In this paper, we present a design problem targeting the improvement of the environmental performance of a railway traction transformer associated to a fully-controlled IGBT rectifier. The Life Cycle Assessment tool was used to evaluate and assess environmental impacts in order to obtain a single environmental criterion of the studied system. This environmental criterion is taken into account on the design stage of the transformer. The design problem with the new criterion is expressed as an optimization problem and solved by using a deterministic multi-objective algorithm. Results are shown as trade-off sets between the environment indicator and the subsystem mass. The convenient solution will be chosen according the price that consumers agree to pay for a reduced environmental footprint.

1 Introduction

With the introduction of different environmental standards and regulations like ISO 14001 [1], ISO 14040 [2] and the commission Regulation EC N° 640/2009 [3], industrial concerns are more and more oriented to the design of green products. Amongst problems met when designing such products is the cost control. Indeed, the cost of the eco-designed product shall match with the price that customers agree to pay for a reduced environmental footprint. The design process of railway traction transformer (TT) associated to a fully-controlled IGBT rectifier (FCR) is a multi-physical and systemic problem. Indeed, such system implies several models that are: electromagnetic, thermal, mechanic, fluid mechanic, etc. These models are strongly linked together and a special attention has to be paid to ensure the consistency of modelling. Moreover, some design parameters [4] have antagonist effect on each component of the system. For example, the increase of the switching frequency of FCR leads to a smaller harmonic content in the traction transformer windings operating at 50Hz so, then less losses. Nevertheless, it increases FCR loss.

R. Ben Ayed: R. Ben Ayed, Professional Freelancer, Power Design Engineer, Consultant at IPSIS Belgium, email: benayed.ramzi@gmail.com

A suited approach is then required to handle such as complex issue for the designer. Multi-objective optimization algorithms are a great help to find a set of trade-offs between conflicting goals that fulfil the technical specifications and design constraints. The consistency of the sub-models used for the multi-physical modelling can be ensured by adding additional constraints and variables in the optimization problem.

This work proceeds in three steps. Firstly the design problem of TT associated to FCR is presented. Secondly, all required models of both components are built. These models are connected together to ensure the consistency of results. Finally, optimization results are analysed. Before starting going in depth of the design problem let's present the system and remember briefly some definitions.

2 Railway Traction Chain Subsystems

A typical synoptic of an AC railway traction chain is given in Fig. 1. The traction Transformer which passes the whole power needed by the train reduces the primary voltage and ensures the galvanic isolation. The full IGBT rectifier converts the AC energy to DC energy in traction mode and the contrary in braking mode. The inverter regulates the traction motors' torque in braking and traction mode.
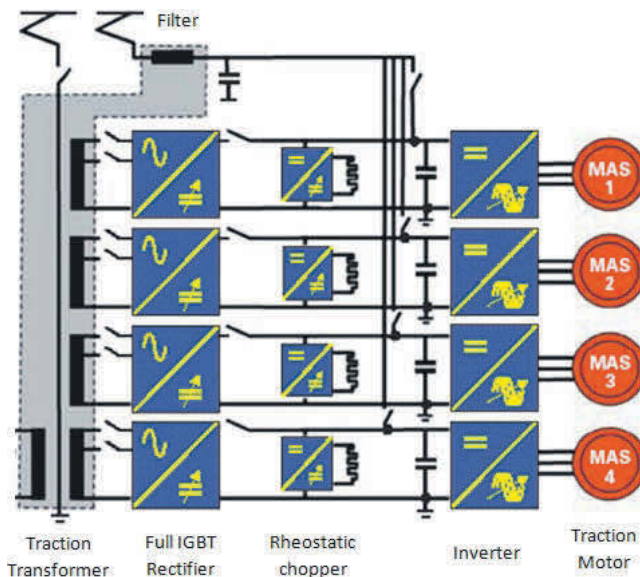
Fig. 1: Electrical synoptic of an electrical AC rolling stock.

3 Ecodesign and Life cycle assessment

3.1 Ecodesign

Ecodesign is an approach that allows the consideration and the minimization of an environmental criterion during the design steps. In literature the environmental criterion can be assessed by several tools. The Life Cycle Assessment (LCA) is among the most widely used.

3.2 Life Cycle Assessment

Life Cycle Assessment [5] is a preventive approach that takes into account the full life cycle of the product (from raw material extraction to end of life) and, the all environmental criteria (raw material depletion, water depletion, energy depletion, toxicity of water and air, hazardous waste production...). The LCA can be used in identifying the main environmental impacts and integrating them in earlier stage of the design process.

A Life Cycle Assessment of a railway traction chain [6] revealed that the traction transformers with its associated rectifiers are the most energy consumers in the traction chain and an optimization of the energy consumption of the subsystem is done. In this paper we will go into details and we will share the most important problems we met during the establishment of models and optimization.

4 Problem Design

The design problem of the subsystem is expressed into an optimization problem. It contains 8 design variables: 7 geometric variables, that are radius of magnetic iron core, width and thickness of wires used in primary and secondary windings, thickness of cooling channels in primary and secondary winding and IGT switching frequency (f_p) in the FCR. f_p is a multiple of the operating frequency (50Hz) and the other variables are considered continuous. *X* refers to the vector of these design variables. The objectives of the optimization is to minimize the mass of TT and minimize the environmental indicator (EI) of the subsystem including the TT and the FCR with the respect of 23 constraints: 8 thermal constraints, 5 geometric constraints, 2 mechanical constraints, 4 electrical constraints, 2 constraints on life time of primary and secondary windings, one constraint on fluid mechanics and one magnetic constraint.

5 Required Models

5.1 Transformer models

In order to calculate the optimization criteria and all constraints expressed in the technical requirement specifications, 4 models of the transformer are developed, that are electromagnetic, thermal, mechanics, and fluid mechanics models. These models are connected together to ensure the consistency of results. For example, the thermal model needs the copper and iron losses calculated by the electromagnetic model in order to calculate winding temperatures and the electromagnetic model needs copper temperature to calculate windings resistance allowing the calculation of winding losses.

5.1.1 Electromagnetic model

This model allows calculating the magnetic field and flux within the iron core, leakage inductance, copper and iron losses, transformer efficiency and the parameters of the equivalent circuit.

The iron core losses are calculated using Steinmetz formula improved by Y. Chen and P. Pillay in 2002 [7] with this analytic formula we got accuracy around 5% on iron losses.

The copper losses were calculated with taking into account proximity and skin effect within transformer winding [8].

The leakage inductance was calculated in a first time by using classical formula based on the transformer geometry, layers number and channel thickness. These formulas reach accurate results only for low frequency studies. But for high frequencies the values obtained shall be multiplied by a coefficient calculated in [9] considering the current harmonics frequencies.

5.1.2 Thermal model

The thermal model is very important while the thermal constraints limit the designer in such as embedded system. Each layer in the transformer is modelled by four thermal resistances that are those of conductor and insulation layer between two conductor layers. The copper losses of each layer were calculated by the electromagnetic model are modelled as current sources in the equivalent thermal circuit given in Fig. 2.

In Fig. 2, T_h is the oil temperature in channels, R_{th_condj}, $j = 1…M$ are thermal resistance of conductor, R_{th_inj}, $j = 1…M + 1$ are thermal resistances of the insulator between layers, T_{condj}, $j = 1…M$ are layers temperature, P_{Jj}, $j = 1…M$ are copper losses for each layer and R_{conv} is the convection thermal resistance of each layers agglomeration.
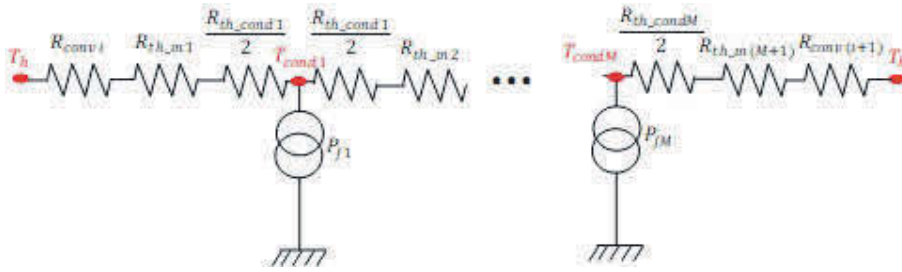
Fig. 2: Equivalent thermal circuit of layers agglomeration located between two cooling oil channels.

The convection resistance is calculated using the convection coefficient which is calculated from Nusselt number. The Nusselt number is calculated from Reynolds and Prandlt numbers, the oil dynamic velocity in the bulk and the contact surface with layers all detailed calculation can be found in [10, 11].

As we can see the convection coefficient depends on the cooling oil velocity which is calculated by the fluid mechanics model.

5.1.3 Fluid Mechanics model

This model is very important because it calculates not only the oil velocity which affects the temperature calculation of windings but also the oil pressure losses that are essential for sizing the motor pump. There are two causes for pressure losses: the first ones are due to channel geometric forms and the second ones are due to the friction of oil with insulation and conductor layers. In our case we neglected the first type of losses as we have straight cooling channels and we assume that the pump provide a constant oil flow $\dot{D}$. Then, the oil pressure losses could be expressed by:

$$P_{losses} = \Lambda \, \frac{L}{D_{eq}} \, \rho \, \frac{v^2}{2} \tag{1}$$

Λ is the Darcy coefficient, ρ and v are, respectively the density and the velocity of cooling oil, D_{eq} and L are hydraulic diameter and length of the cooling channel. This relation could be expressed also by:

$$P_{losses} = \frac{\rho}{2S^2} \, \Lambda \, \frac{L}{D_{eq}} \, \dot{D}^2 = Z \, \dot{D}^2 \tag{2}$$

where Z is the equivalent channels coefficient [12] and it's calculated by:

$$\frac{1}{Z} = \left(\sum_{i=1}^{n_c} \frac{1}{\sqrt{Z_i}} \right)^2 \tag{3}$$

with n_c is channel number and Z_i is the coefficient of one channel. The mechanics fluid equivalent model is shown in Fig. 3. $\dot{D}_i$ is the oil flow in channel number i, then the oil velocity canbe calculated in each channel.

5.1.4 Mechanics model

The mechanics model calculates the pressure generated by electromagnetic forces on the outside wall of windings during a short-circuit phase. Indeed, one of constraints in the technical requirement specifications of the transformer to check that this pressure is less than 60 MPa in short circuit case.

The electromagnetic forces reach its maximum value on the last winding outside wall (N.I Amps/turn are maximum) when the short circuit current reaches its maximum value. Let's consider the current in the positive alternation, the forces could be presented as in Fig. 4.

The pressure is calculated from electromagnetic force applied on winding circumference element F_e and the winding height h_{wind} as:
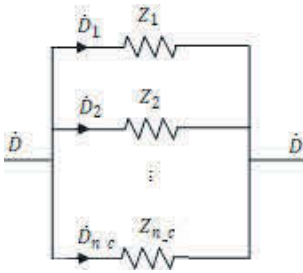
$$p = \frac{F_e}{h_{wind}} \tag{4}$$

Fig. 3: Equivalent fluid mechanics model.
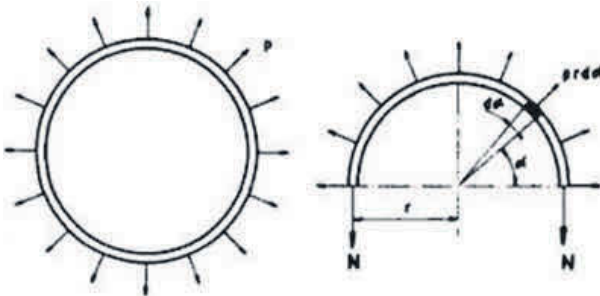
Fig. 4: Pressure on the outside wall of the winding during short circuit phase.
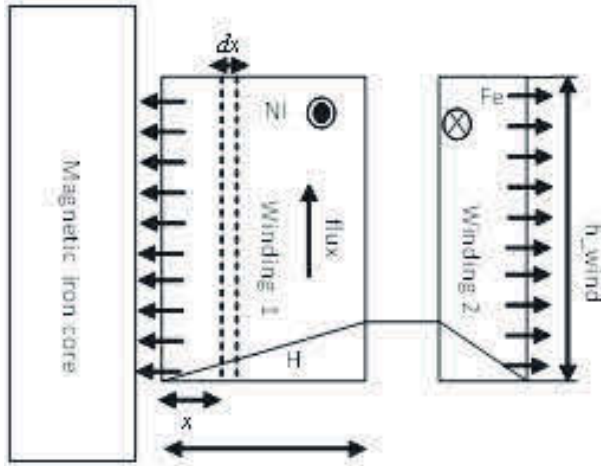
Fig. 5: Electromagnetic force applied on winding circumference element.

In order to calculate this force F_e, we assume that the leakage flux are axial and the amps-turn (NI) are consumed in and between windings. Then the magnetic field H varies linearly in the radial direction as shown in Fig. 5.

According to Laplace formula we have:

$$\frac{dF_e}{dl} = \frac{NI}{e} \, dx \, \mu_0 \, \frac{NI}{h_{wind}} \frac{x}{e} \tag{5}$$

By integration from 0 to winding thickness e we got:

$$F_e = \frac{(NI)^2}{2h \, enr} \quad (N/m) \tag{6}$$

Then the constraint shall be expressed as:

$$\sigma_m = \frac{p\,r}{e} = \frac{F_e\,r}{Ns} \leq 60\,\text{MPa} \tag{7}$$

where N is the conductor turns number and s is the section of the conductor.

5.2 FCR models

Three models are developed for the FCR, that are thermal, electrical and control models. The control model calculates the PWM signals provided to IGBT driver in order to regulate the fundamental voltage (VPMCF) phase and peak across the secondary winding of the transformer. The purpose of the regulation is working with a power factor equal to one.

5.2.1 Control Model

The electrical synoptic of the studied subsystem is given in Fig. 6.

The control model allows calculating the command signals (f_{11} and f_{21}) for FCR's IGBT. A synchronous commandis used. This type of command consists of comparing two a sine wave signal to a saw tooth signal as shown in Fig. 7. In the railway application for such as subsystem the switching frequency fp is about some hundreds Hz.

We want that the power factor of the subsystem is equal to one. Then the ratio between sine wave amplitude and the saw tooth signal amplitude and the phase delay between both signals are calculated according the power duty point, the secondary
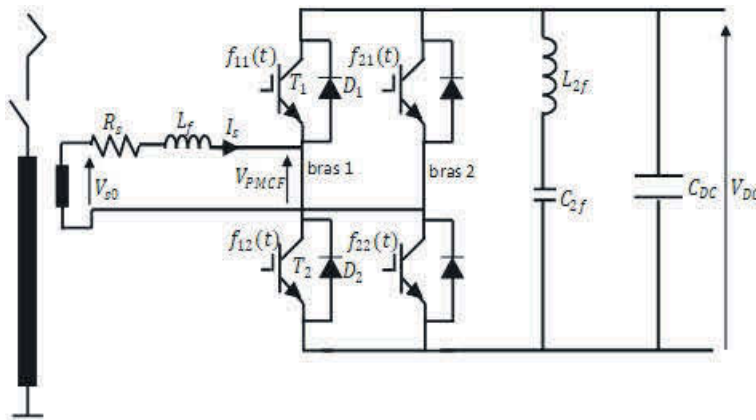
Fig. 6: Electrical synoptic of the TT and one fully-controlled IGBT rectifier.
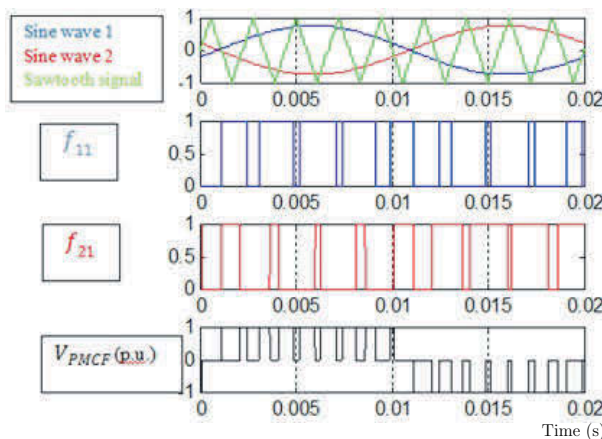
Fig. 7: Command signals for IGBT and the voltage across the FCR.
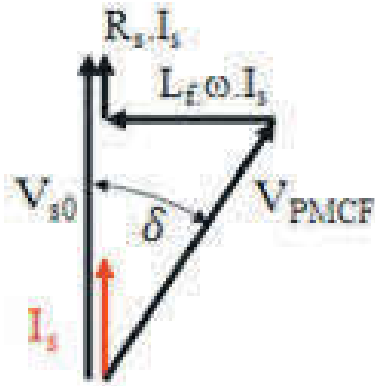
Fig. 8: Vector diagram.

transformer voltage and the DC voltage across the DC bus according the vector diagram shown in Fig. 8.

5.2.2 Electrical Model

The electrical model allows calculating the switching and conducting losses in semi-conductors components.The conduction losses within the IGBT and diodes could be easily calculated from their datasheet and the conducted current (Is). Let's note the conduction losses with the IGBT by $Losses_{IGBT}^{Cond}$ and the conduction losses within the diode by $Losses_{IGBT}^{Cond}$.

The total energy losses during switching are the sum of the energy losses during switching-on (E_{on}), switching-off (E_{off}) and reverse recovery losses (E_{rr}). The simplest way found to calculate these losses in literature is in [13].

$$E_{on}(I_c, V_{DC}, T_j) = k_{on}(T_j)I_s V_{DC} \tag{8}$$

$$E_{off}(I_c, V_{DC}, T_j) = k_{off}(T_j)I_s V_{DC} \tag{9}$$

$$E_{rr}(I_c, V_{DC}, T_j) = k_{rr}(T_j)I_s V_{DC} \tag{10}$$

with:

$$k_{on} = td_{on} + t_r \tag{11}$$

$$k_{off} = td_{off} + t_f \tag{12}$$

$$k_{rr} = t_{rr} \tag{13}$$

td_{on} is the turn-on delay time, t_r is the turn-on rise time, td_{off} is the turn-off delay time, t_f is the turn-off fall time, and t_{rr} is the reverse recovery time. All these parameters are

in the component datasheet. On each switching on the energy losses could be written as:

$$E_{on}(t) = k_{on}^{125\text{°}C} V_{DC}(t) i_s(t) \tag{14}$$

The average energy losses during the positive alternation is:

$$E_{on}^{average} = \frac{2k_{on}^{125\text{°}C} V_{DC}}{T} \int\limits_{\frac{\varphi}{\omega}}^{\frac{\varphi}{\omega}+\frac{T}{2}} I_s \sqrt{2}\sin(\omega t - \varphi)dt = \frac{2\sqrt{2}k_{on}^{125\text{°}C} V_{DC} I_s}{\pi} \tag{15}$$

As the IGBT 1 commute $\frac{1}{2}f_p$ times per second (only during positive alternation), the power losses could be deduced as:

$$Losses_{on} = \frac{F_p \sqrt{2}k_{on}^{125\text{°}C} V_{DC} I_s}{\pi} \tag{16}$$

By doing the same exercise with the switching-off and reverse recovery losses we got:

$$Losses_{off} = \frac{F_p \sqrt{2}k_{off}^{125\text{°}C} V_{DC} I_s}{\pi} \tag{17}$$

$$Losses_{diode}^{sw} = \frac{F_p \sqrt{2}t_{rr} V_{DC} I_s}{\pi} \tag{18}$$

Then, switching losses within IGBT:

$$Losses_{IGBT}^{sw} = losses_{on} + losses_{off} = \frac{F_p V_{DC} \sqrt{2}I_s}{\pi}[td_{on} + t_r + td_{off} + t_f) \tag{19}$$

The total losses within IGBT and diode are:

$$Losses_{IGBT} = Losses_{IGBT}^{sw} + Losses_{IGBT}^{Cond} \tag{20}$$

$$Losses_{diode} = Losses_{diode}^{sw} + Losses_{diode}^{Cond} \tag{21}$$

These losses are used by the thermal model in order to calculate the junction temperature of IGBT packs.

5.2.3 Thermal model

The thermal resistance of the heat-sink $R_{th-sink}$, The thermal resistance of the case $R_{th-case}$, the thermal resistance of the diode junction $R_{th-jundiode}$ and the thermal resistance of the IGBT junction $R_{th-junIGBT}$ are given by component suppliers.

The thermal model we consider is given in Fig. 9, where T_j means temperature junction, T_{case} means case temperature, and T_{amb} is the ambient temperature inside the FCR cubicle. This model is validated on a test bench.
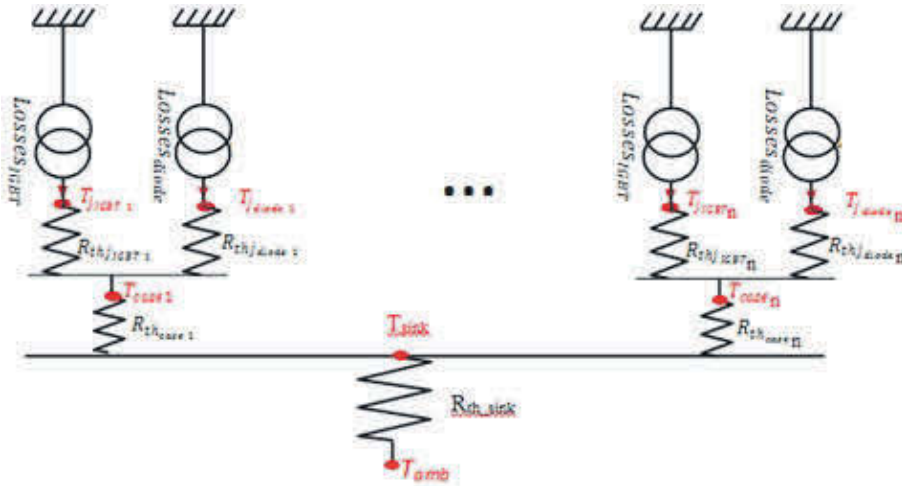
Fig. 9: The thermal model of the subsystem.

5.3 Environmental model

We built an environmental model using environmental management software named EIME® (Environmental Information and Management Explorer) [15]. This software allows the calculation of eleven impacts. They are:

RMD: Raw Material Depletion,

ED: Energy Depletion; WD: Water Depletion,

HWP: Hazardous Waste production,

GW: Global Warming; OD: Ozone Depletion,

POC: Photochemical Ozone Depletion,

AA: Air Acidification,

AT: Air Toxicity,

WT: Water Toxicity,

WE: Water Eutrophication.

We assume in our model that all impacts are linear functions that can be expressed as:

$$Im_i = \sum_{mat} (\alpha^i_{mat} M_{mat}) + LD\alpha^i_{wat}(\beta_1 P_{all} + \beta_2 P_{iron}) \tag{22}$$

where: Im_i is one of eleven impacts calculated by EIME, α^i_{mat} is the value of Im_i calculated by EIME for 1 kg of material (mat); is the mass (Kg) of material (mat); LD is lifetime of transformer in years; α^i_{wat} is the value of Im_i calculated by EIME for consuming a watt in a year; β_1 is the percentage of operating time of the transformer in full load, β_2 is the percentage of operating time of the transformer at no-load. The EM calculates the eleven impact of EIME with a high accuracy (error is less than 0.1%).

Fig. 10 shows the contribution of each life stage of the transformer (Manufacturing (M), Distribution (D), and Use (U)) on its environmental impacts. Fig. 10 confirms that the use stage is the most polluting comparing to manufacturing and distribution stages. So to reduce substantially the impacts we need to reduce the transformer energy consumption.

After calculating the 11 impacts that are results of the life cycle inventory, the next step according to life cycle assessment process is the impact assessment. Several methods exist to aggregate the impacts calculated by EM. Impact 2002 + is chosen because it is the most recent method and its approach respects the standard ISO 14044 [19]. This method is detailed in [5]. The environmental indicator (EI) of Impact 2002+ is obtained by weighting the four categories of damage: damage of global warming, damage on ecosystem, damage on human health and damage on resources. Each category of damage is an aggregation of impacts calculated by the environmental model. Figure 11 shows the impact (midpoint) categories and the four damage categories within which they interfere. For some of environmental impacts, it is necessary to convert environmental impacts units in order to prepare data for EM. For instance, in the case of "Air Acidification" impact, unit shall be converted from gram equivalent of (ion of hydrogen) to kg of nitrogen oxides to be used by Impact2002+.

At this level of the study the optimization problem is simplified by reducing the number of objectives: a bi-objective optimization (M, EI) problem instead of an optimization problem which has twelve objectives (the mass and the 11 impacts).
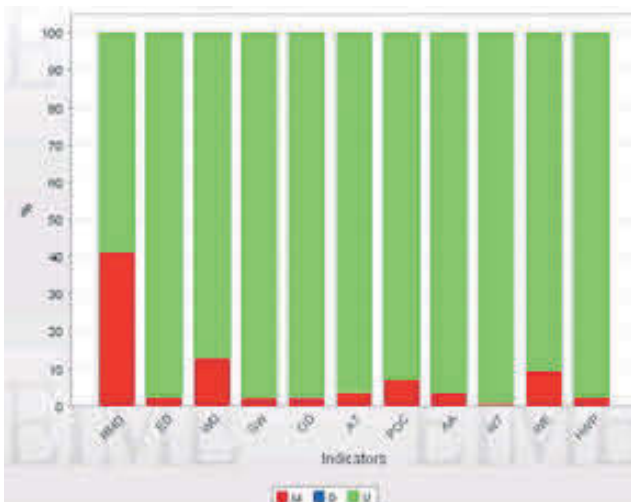
Fig. 10: Contribution of each life stage of the transformer on its environmental impacts.
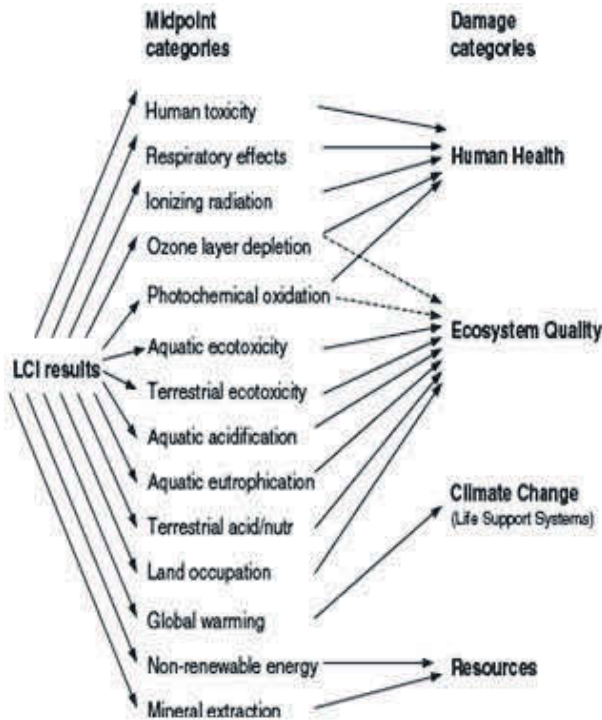
Fig. 11: Overall scheme of the IMPACT 2002+ framework, linking Life Cycle Inventory (LCI) results via the midpoint categories to damage categories.

5.4 Consistency of multi-physical models

A complete multi-physical model shown in Fig. 12 was built. Multi-physical models of both components are connected because the FCR model needs values of equivalent AC resistances Rs and leakage inductances Lf of the transformer secondary to calculate the phase and the amplitude of VFCR by the control model (see also Fig. 8). Multi-physical model of the TT needs the harmonic spectrum of VFCR (H.VFCR) to calculate the current harmonic spectrum that flows transformer windings and
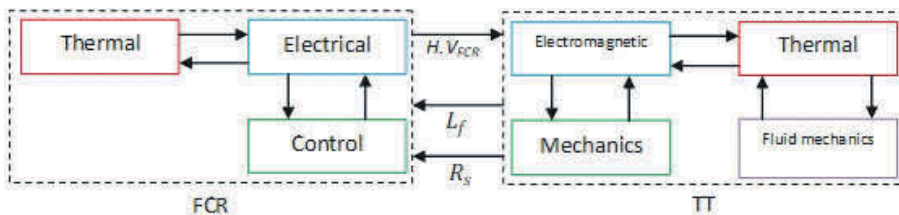
Fig. 12: Complete model of the *TT* and *FCR*.

then iron and copper losses are calculated. To solve these interactions within the optimization process, the MDF formulation [14] combined with the fixed-point method is chosen as the characteristics of the used calculator aren't suitable for parallel computing.

6 Multi-objective Optimization

As said in the design problem paragraph our design problem is a bi-objective optimization problem where the both objective are conflictual. Indeed, by reducing the *TT* mass the electrical losses will increase. It's demonstrated in [15], that for electrical systems whose the life time is long and the losses are important the use phase dominates the manufacturing and the end life phases in the life cycle of the product [16]. Then, if the TT mass is minimized, the electrical losses increase and the environmental indicator (EI) becomes worst.

So, to recapitulate, we have two conflictual objectives that are EI and TT mass, but we proved also that the EI is proportional to minus the efficiency (-?) of the system (TT+FCR). To overcome this optimization problem we combined both objectives in a single objective (Ob) which is a weighting of our objectives, for $\alpha \in [0, 1]$:

$$Ob = \alpha\,TTmass(p.u) + (\alpha - 1)\eta(p.u) \tag{23}$$

Now, our optimization problem is a single optimization problem with 8 variables, we choose the SQP method combined with the weighting method [17] to obtain many compromises between the *TT* mass and $-\eta$). Therefore, many design configurations are available to best meet the needs of customers. Algorithm optimization is shown in Fig. 13.

Optimization results are shown in Fig. 14. These results show separate Pareto fronts for different switching frequencies. This confirms that f_p has a direct influence on the geometric parameters of the transformer. According to these results, the switching frequency of 750 Hz which is higher than the actual frequency allows to reduce losses within the subsystem. But, we know that the losses within the *FCR* increase as well as the switching frequency increase. To explain these results we will study what happened with the *TT* losses.

According to the Dowell formula shown in [8, 9] and already used in the electromagnetic model. The copper losses are calculated as:

$$Losses_{copper} = R_{dc}\,I_s^2 + \sum_{h=2}^{\infty} F_R(f_h)R_{dc}I_h^2 \tag{24}$$

Where R_{dc} is the equivalent DC resistance of the *TT*, and *FR* is a coefficient allowing calculating the equivalent *AC* resistance from *DC* resistance. In this equation we have to see two terms: the first one is the current harmonic Ihand the second one is *FR*. We
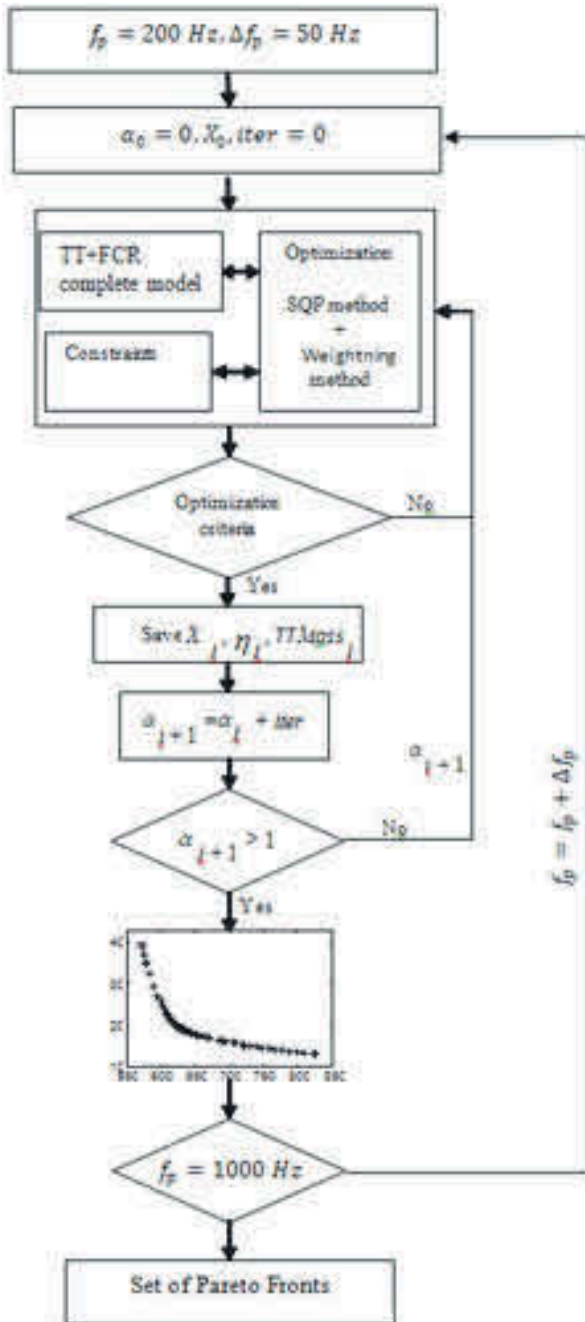
Fig. 13: Optimization process.
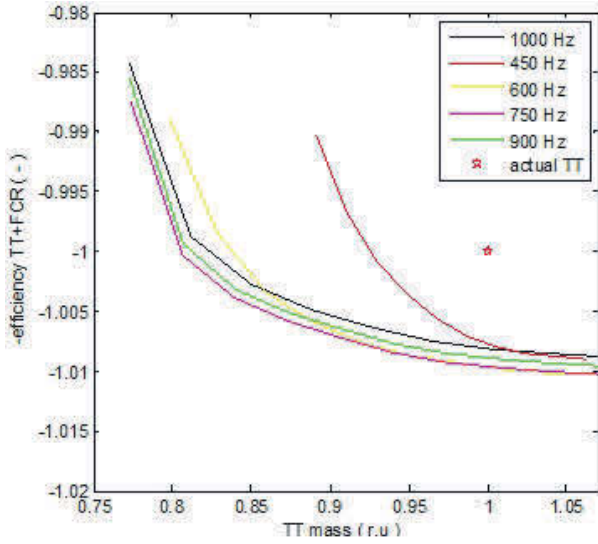
Fig. 14: Trade-offs for different switching frequency.

made a comparison between R_{ac} and $2\pi L_f f_h$ values from the fundamental frequency to the highest harmonic frequency we find ratio from 140 to 311. So, R_{ac} could be neglected, and the current harmonic could be simplified as:

$$I_h = \frac{V_h}{2\pi L_f f_h} \simeq \frac{C_1 V_h}{f_h} \tag{25}$$

wher C_1 is a constant.

We studied also in the Fig. 15 the evolution of the FR coefficient with harmonic frequencies. This figure shows that for high frequencies FR could be expressed according to the square root of the frequency as:

$$FR \simeq C_2 \sqrt{f_h} \tag{26}$$

where C_2 is a constant.

By replacing these equations in the copper losses equation, the copper losses for high frequency could be written as:

$$Losses_{copper} = R_{dc} I_s^2 + \sum_{h=2}^{\infty} C_3 \frac{1}{\sqrt{f_h}^3} \tag{27}$$

This demonstrates that for high switching frequency (also high harmonic frequencies), that the copper losses that are the dominate losses in TT (98% of losses) decrease and are close to the DC copper losses. Optimization results show also that it's possible to design a TT 18% lighter than the actual transformer with the same efficiency or a
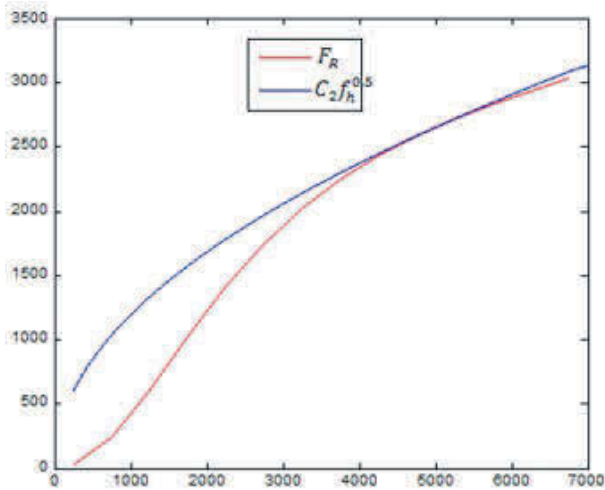
Fig. 15: Evolution of the coefficient FR with harmonic frequencies.

TT which has the same mass, but with an efficiency 1% higher than the actual *TT* with a switching frequency equal to 750Hz. More intermediate solutions that present a balance between both criteria are also available.

7 Conclusion

In this work, a specific approach is investigated in order to reduce the environmental footprint of a railway traction transformer associated to a fully-controlled rectifier. A LCA allowed calculating 11 environmental impacts of the system and then combined them in one criterion thanks to "impact 2002+" method. The design problem is simplified and expressed as a bi-objective optimization problem and solved by Multi-objective algorithms. A multiphysics model was built and used within the optimization process to calculate problem constraints and criteria. Results show that is possible to minimize the transformer mass by 18%, or improve the transformer efficiency by 1% by changing its geometric parameters and the switching frequency of the fully-controlled rectifier. These results are obtained considering that all transformer parameters are continuous. If some parameters are discrete, other algorithms as Branch and Bound [18] could be used. The optimization process will be more expensive in terms of computing time and new results are expected.

Bibliography

[1]   ISO 14001 Environmental Management Systems. Int. Organization for Standardization, 1996.

[2]   Standard ISO 14040, October 2006.

[3]   Commission Regulation (EC) No 640/2009 of 22 July 2009 implementing Directive 2005/32/EC of the European Parliament and of the Council with regard to eco-design requirements for electric motors

[4]   W.G. Hurley, W. Wölfle and J.G. Breslin. Optimized transformer design: Inclusive of high frequency effects. IEEE Trans. on Power Electronics, 13:651–659, July, 1998.

[5]   O. Jolliet, M. Margni, R. Charles, S. Humbert, G. Payet, G. Rebitzer, R. Rosenbaum. IMPACT 2002+: A New Life Cycle Impact Assessment Methodology. Int. Journal of Life Cycle Assessment, :324–330, 2003.

[6]   R. Ben Ayed, S. Brisset. Eco-design of railway traction chain. LCA Conf., Lille, France, 3-4 November, 2011.

[7]   Y. Chen and P. Pillay. An Improved Formula for lamination core loss calculations in machines operating with high frequency and high flux density excitation. Industry Applications Conf., 37th IAS Annual Meeting, Pittsburgh, Pennsylvania, USA, 13–18 October 2002.

[8]   R.W. Erickson and D. Maximovie. Fundamentals of power electronics. 2nd edition, Kluwer Academic Publishers, New York, :474–487, 2004

[9]   P.L.Dowell. Effects of Eddy Currents in Transformer Windings. Proc. of the IEE, 113(8):1387–1394, August 1966.

[10] S.A. Ryder. A simple method for calculating winding temperature gradient in power transformers. IEEE Trans. on Power Delivery, 17(4):977–982, October, 2002.

[11] A.J. Oliver. Estimation of transformer winding temperatures and coolant flows using a general network method. IEE Proc., 127(6):395–405, November, 1980.

[12] P. Fridmann. Equilibrage des réseaux de distribution (In French). Techniques de l'ingénieur, Reference BE 9200, octobre, 1999.

[13] F. Sargos. IGBT Power Electronics Teaching System-Principle for sizing power converters. Application Note AN-8005, September 2008. Online available at: http://www.thierry-lequeu.fr/data/AN-8005-Teaching-System.pdf

[14] R. Ben Ayed and S. Brisset. Multidisciplinary optimization formulations benefits on space mapping techniques. Int. Journal for Computation and Mathematics in Electrical and Electronic Engineering (COMPEL), 31(3):945–957, 2012.

[15] Codde.fr

[16] R. Ben Ayed and S. Brisset. The influence of the environmental criterion on the design of an auxiliary transformer for the railway traction. Proc. of ICEM 2010 (from CD-ROM), Rome, Italy, September 2010.

[17] S. Kreuawan. Modeling and optimal design in railway applications. Chapter 3: Optimization technique, :65-72, November 2008.

[18] R. Ben Ayed and S. Brisset. Expert Knowledge Benefits on Discrete Optimization Algorithm. Proc. of Compumag, Sidney, Australia, July, 2011.

[19] Standard ISO 14044, October 2006.

Biographies

Ramzi Ben Ayed was born in Sfax, Tunisia, on August 29th, 1982. He received the Electrical Engineering degree from the National Engineering School of Sfax, Tunisia in 2007 and the MS degree from the University of Picardie Jules Vernes, Amiens, France in 2008, and the Ph.D. degree from EcoleCentrale de Lille, Lille, France in 2012. During 2011-2013 he was a Research assistant at the University of Lille 1, where he was involving in teaching and supervising electrical engineering student. During 2013-2016 he was a consultant in designing railway subsystem. Actually, he is a professional freelancer engaged as a power design engineer in railway fields.

A. Alfaoury and A. Agha

Long - Term Energy Losses Analyses For Jordanian Power system (Commercial Losses)

Abstract: This paper aims to investigate the electrical energy losses (ΔE) in the Jordanian national electrical power system (E_S); their types, values, as well as their impacts on overall performance of the energy system. The main focus of the paper is to calculate and investigate the value of the technical losses (ΔE_T) as well as the commercial losses (ΔE_C) to the whole system losses value. In this paper, analyses of the (ΔE) data are carried out for the last sixteen years. This period of time is divided in two equal intervals of time; which are (2000-2007) and (2008-2015). The analyses concentrate mainly on the (ΔE_C) with special attention on the black losses of energy (theft), (ΔE_{B1}). The results of the two time periods are compared and evaluated by using statistical indexes. Furthermore the paper attempts to provide answers to the following questions: How and up to what value can (ΔE_C) be minimized? What is the economic influence of (ΔE_C) in [MWh]? Finally, a set of conclusions and recommendations on the obtained results are along with offered of the commercial losses for the next five years a forecast.

Keywords: Electricity losses analyses, commercial losses, thefts of electrical energy.

Classification: 65C05, 62M20, 93E11, 62F15, 86A22

1 Introduction

Since 2013, The Jordanian media has been attentive to the subject of the black losses (ΔE_{B1}), which called also, electrical energy thefts, introducing different figures from different sources about the amount of energy thefts in [MWh].

The electrical energy losses (ΔE) can be simply defined as the difference between the total of electrical plants output minus the total sent out energy. Various approaches have been used to assess the amount of the (ΔE) of the (E_S), which include analytical [1], statistical [2] and heuristic methods [3]. These approaches mainly differ in the way of (ΔE) calculation, simplicity, the input data required, computational time as well as the accuracy of the achieved results.

In order to get the right answer of (ΔE) amount in [MWh], the presented method in [4, 5] is used to analyze (ΔE) for the periods (2000-2007) and (2008-2015). The study of the (ΔE) is carried out to investigate the amount of the black losses (ΔE_{B1}) -also

A. Alfaoury and A. Agha: A. Alfaoury: Electrical Engineering Department, Al-Balqa' Applied University, Al-Salt - Jordan, email: audihalfaoury@gmail.com, A. Agha: Electrical Engineering Department, Philadelphia University, Amman - Jordan, email: aagha@philadelphia.edu.jo

known as- "the misuse of the electrical energy". The definitions and determination of the (ΔE) types will be subject to the further discussion in the following sections.

Moreover, section 2 presents the classifications of the electrical energy losses; whereas, the formulation of the mathematical model of the electrical energy losses is demonstrated in section 3. Section 4 further investigates energy losses analyses along with the statistical indexes calculations. While section 5 forecasts the commercial losses amount for the next five years. Finally, propositions and recommendations towards the reduction of the misuse of the electrical energy and results / conclusions are presented in sections 6 and 7 respectively.

2 Energy losses Classification

The electrical energy losses (ΔE) can be classified into two parts; technical losses (ΔE_T) and commercial Losses (ΔE_C) as follows:

2.1 Technical Losses (ΔE_T)

These are the "Joule effect" or heat losses, produced by the flow of the current in the (E_S) transmission lines, transforms and associated equipment. They consist of load losses and the no-load losses, as the main part of (ΔE).

2.2 The Commercial Losses (ΔE_C)

These are defined as the difference between the energy actually consumed and the energy- effectively billed by the different electric utilities. They are also, defined by [6] as a portion of energy, which is either not billed precisely or not entirely billed. The (ΔE_C) can be caused by one or more of the followings:

1. Metering Instruments Errors (ΔE_{MIE}): These are due to the errors or malfunctioning of the (CT'), (VT's) and (kWh) meters, the effects of these errors to the (ΔE_C) amount vary between (0.75% - 3%), [7].
2. Billing Error (ΔE_{BSE}): caused by the shifting of the energy meters reading, where this error for one month is about (3.36 %), however for the average value over the year, it is approximately around (0.28 %), (i.e. 3.36% / 12 month = 0.28% /year).
3. Human Error (ΔE_{HE}): caused by human during the translocations of the energy meters readings data and normally is compensated for a long period of time.
4. Illegal Consumption of Electrical Energy (ΔE_{B1}). This type of losses is also called "black losses" (??Bl) or (thefts of energy), and cannot be considered as technical losses. To determine the amount of the thefts energy (ΔE_{B1}) to the total energy (ΔE) amount, a mathematical model is formulated.

3 Energy Losses Mathematical Model

The (ΔE) for a certain period of time can be expressed as the difference between the sums of electrical plants as:

$$\Delta E = \Delta E_C + \Delta E_T \tag{1}$$

The amount of (ΔE_T) can be determined by the integration of the power losses (ΔP) over a certain period of time (T):

$$\Delta E_T = \int_0^T \Delta P(t)dt \tag{2}$$

(2) The (ΔP) is the real part of the complex power losses [8–10], obtained from the power flow program, which is subject to the line conductance (G_{ik}) and the voltage (V) magnitude between the buses (i) and (k), as:

$$P_{i,k} = G_{i,k} \Delta V_{2ik} \tag{3}$$

And from equation (1), we obtain:

$$\Delta E_C = \Delta E - \Delta E_T \tag{4}$$

Taking into account, the different types of errors as explained in (section 2), the commercial losses (ΔE_C) balance can be expressed as:

$$\Delta E_C = \Delta E_{MIE} + \Delta E_{BSE} + \Delta E_{HE} + \Delta E_{Bl} \tag{5}$$

These values of (ΔE_{MIE}), (ΔE_{EMA}), (ΔE_{BSE}), and (ΔE_{HE}) can be estimated by using statistical and engineering practice. Having the value of (ΔE_C) from equation (4) and equation (5) then, the product is the value of the (ΔE_{Bl}) as:

$$\Delta E_{Bl} = \Delta E_C - (\Delta E_{MIE} + \Delta E_{BSE} + \Delta E_{HE}) \tag{6}$$

By using equation (6), it will be possible to determine the amount of the black losses (ΔE_{Bl}), -thefts of energy-.

4 Electrical Energy Losses ANALYSIS (2000–2015)

4.1 Energy Losses Input Data

The (ΔE) data for the period (2000-2015) will be analyzed. As mentioned in (section 1) this period is divided into two equal periods of time:

Tab. 1: System Energy Balance (Extracted from the Energy Balance) [11].

A [GWh]: Sum (Gen.)+(Tran.)+(Dist.)losses

B [GWh]: Generated & Imported Energy

C [GWh]: Consumed & Exported Energy

D [GWh]: Total Sys. Losses $D = B - C$

E [GWh]: Commercial losses $E = |A - D|$

F [%]: Total Sys. Losses $F = \dfrac{D}{B}$

K [%]: Commercial Losses $K = \dfrac{E}{A}$

AVG.: Average returns the (arithmetic mean) of the arguments.

STDEV: The standard deviation is a measure of how widely values are dispersed from the average value.

MIN./AVG.: The smallest number in a set of values to the average value

MAX./AVG.: The largest number in a set of values to the average value.

Year	A	B	C	D	E	F	K
2008	2526	14385	11832	2553	27	17.75	1.07
2009	2534	14655	12095	2560	26	17.47	1.03
2010	2520	15447	12900	2547	27	16.49	1.07
2011	2713	16385	13621	2764	51	16.87	1.88
2012	2934	16497	14555	1942	992	11.77	33.81
2013	2979	16722	14356	2366	613	14.15	20.58
2014	3201	17666	15121	2545	656	14.41	20.49
2015	3325	18548	15787	2590	611	14.33	18.38
AVG.	2,841.5	16,288.1	13,783.9	2,483.9	342.63	/	/
STDEV.	317.23	1,426.45	1,423.89	243.7	419.03		
MIN. / AVG.	0.8869	0.8832	0.8584	0.782	-0.1489	/	/
MAX. /AVG.	1.1702	1.139	1.145	1.113	2.895	/	/

- The first period; is related to the (ΔE) data for the period (2008-2015) as demonstrated in (Tab. 1), which shows the relations between the obtained figures. Statistical indexes also, are calculated.
- The second period; is related to the electrical energy losses data for the period (2000-2007). The results for this period of time are obtained in the same way as the first period. However, to avoid the repetition in calculation, only the statistical indexes for this period (2000-2007) are demonstrated and compared with the period (2008-2015). The results of comparison are presented in (Tab. 2).

The MIN./AVG and MAX./AVG. ratios are used both to describe the minimum or maximum values of system and to guide policy decisions. The higher the ratio of the minimum value to the average (mean), the better is the relative position of the minimum value and vice versa. Consequently, the lower the ratio of the maximum value to the average (mean), the better is the relative position of the maximum value and vice versa [12].

Tab. 2: Statistical Indexes for (2000-2007) and (2008-2015).
(1): Sum = (Gen.) + (Tran.) + (Dist.) losses [GWh]
(2): Generated & Imported Energy [GWh]
(3): Consumed and Exported Energy [GWh]
(4): Total System Losses = $(B - C)$ [GWh]
(5): Total System Losses = (D/B) (%)
(6): Commercial losses = $|A - D|$ [GWh]
(SI): Statistical Indexes
(Ch): Change (%).
)1 : - is due to division by zero, where the [Change (%) = $(\Delta C/C_1)\%(C_2 - C_1)/C_1$]%.

(SI)	AVG.		STDEV		MIN./AVG.		MAX./AVG.	
Years	00-07	08-15	00-07	08-15	00-07	08-15	00-07	08-15
Sn.	A_1	A_2	B_1	B_2	C_1	C_2	D_1	D_2
(1)	1,746.75	2,841.50	374.85	317.23	0.75	0.89	1.41	1.17
(Ch)	62.67		−18.16		18.43		−17.15	
(2)	9,462.75	16,288.13	1,986.41	1,426.45	0.76	0.88	1.37	1.14
(Ch)	72.13		−28.19		16.56		−16.91	
(3)	7,723.75	13,783.38	1,612.69	1,423.89	0.76	0.86	1.36	1.15
(Ch)	78.45		−11.71		12.91		−15.76	
(4)	1,739.00	2,483.38	377.85	243.65	0.75	0.78	1.04	1.11
(Ch)	42.80		−35.52		4.77		7.45	
(5)	18.37	13.61	0.47	2.07	0.96	0.86	1.04	1.30
(Ch)	−25.88		339.15		−10.24		25.87	
(6)	11.25	299.00	12.85	385.63	0.00	0.0835	3.644	3.3177
(Ch)	2,557.78		2,901.48		(#DIV)1		−8.96	

4.2 Analyses of Electrical Energy Losses Results (2015)

To demonstrate the analyses of the obtained results, as an example, the analyses are conducted for the data related to the year (2015) from (Tab. 1) and as follows:

1. The value of the total system energy losses (ΔE), as (in column F) is (14.33%), which illustrates the difference between the (generated and imported energy) and (consumed and exported Energy) (i.e.: column B and column C), the result of that is 2590 [GWh] as in (column D).

2. The commercial energy losses (ΔE_C) are the difference between the sum of (generation, transmission and distribution losses - i.e. column A) and the (total system losses, i.e. column D), the result of that is 611 [GWh] as in (column E), which is percentage is equal to (18.38%) of the total amount of energy losses as in (column K).

3. Since last decade till 2011, the commercial energy losses (ΔE_C) value was varied between (1% to around 2.0%) as in (column K), and, for the last three years this value was drastically increased (i.e. 20.58%, 20.49%, 18.38% for the years 2013, 2014 2015 respectively) as in (column K). Therefore, the value of the thefts energy

(ΔE_{B1}) as indicated in eq. (6) is the difference between Energy commercial losses (ΔE_C) and the sum of justified lo (i.e. 1% - 2.5%). The product of that shall be varied between 17.38% and 16.38%, (i.e. 18.38% − 1% = 17.38% and 18.38% − 2.0% = 16.38%).

4. The value of the thefts (ΔE_{B1}) is varying between 17.38% and 16.38% of the total system energy (ΔE) which equal 14.33% for the year 2015. Thus, (ΔE_{B1}) is equal between (18.38% − 14.33% = 2.63% and 16.38% - 14.33% = 2.35%). The total value of the (generated & imported energy) is 18548 [MWh] as in (column B). Finally, the (ΔE_{B1}) amount in [MWh] is varying between (2.63% × 18548 = 487.8 [GWh]) and (2.35% × 18548 = 435.9 [GWh]. This represents the black losses (the thefts of energy) for the year 2015.

4.3 Statistical Indexes Determination

The results of comparison between the statistical indexes of the electrical energy losses for the Periods of (2000-2007) and (2008-2015) are demonstrated in (Tab. 2).

4.4 Energy Losses Statistical Indexes Analyses

The analyses are carried out here based on the statistical indexes as in (Tab. 2) and as follows:

1. The "average change in percentage" (chg %) of the (consumed and exported energy) is equal to (78.45%), and is more than (chg %) of the (generated & imported energy) which equal to (72.13%). This means, there is still a need for new generating units to be added to the electrical system.
2. The (chg %) of the (total system losses) is equal to (−25.88%). The sign (−) is due to the total energy amount (ΔE) for the period of (2008-2015) is less in total than for the period (2000-2007) which calculated from the relation of column (D/B) in (Tab. 1).
3. The (chg %) of the (commercial losses) is about (−8.96%), and is due to the great efforts taken by the electric providers companies in striving the illegal consumption of energy (thefts).
4. The (chg %) of the standard deviation (STDEV) of the (commercial losses) is equal to (2.9%) and this is due to illegal consumption of energy (thefts).
5. The (chg %) of the value of (MIN/AVG) in the (total system losses) is equal (−10.24%), this means that there is a decrease of the total losses value due to the efforts taken against the illegal consumption of energy (thefts). And the same conclusion can be extracted from the relation of (MAX/AVG) value of the sum losses which is equal (25.87%).
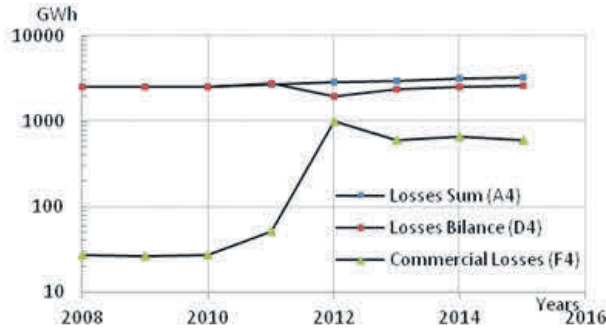
Fig. 1: System losses.

Furthermore, a lot other relations can be deduced from (Tab. 2).

Electrical System Losses Curve The system energy losses (ΔE) for whole the analyzed period (2008-2015) is presented as in Fig. 1, where; (line D_4) is slightly decreased in comparison to (line A_4), meanwhile the commercial losses (line F_4) are increased. This can be interpreted as follows: as there was an increment on the demand for electrical energy due to the increment in loads, this causes a relative reduction in the ratio of the total losses. Consequently, the relative system losses are reduced and the whole system efficiency is slightly improved.

5 Electrical Commercial Losses Forecasting (2016-2020)

In order to forecast the behavior of the commercial losses to the total amount of commercial losses for the next five years (2016-2020), the analyses is run based on the existing data of the commercial losses in (%) as presented (Tab. 1) column (K), moreover, the analysis is performed by using regression line analysis, whereas the least squares method is used to provide the best possible fit [13]. By that, the liner regression model as in equation (7) is used.

$$Y = a\,t + b \qquad (7)$$

where: Y: The regression line
a: The slope of the line is the change in (Y) which accompanies an increase of one unit of time (t).
t: Time, it is equal 1 for the first year of the analyzed period and so up to n-years.
R_2: The coefficient of determination is varying between (0 and 1). The more (R_2) is close to 1, the more strong relationship is in the fitting of the data.

The illustration of the commercial losses is as plotted in Fig. 2.

Tab. 3: Existing and Forecasting of Commercial Losses (%)

	Existing Energy Commercial losses (2008-2015)							
Years	2008	2009	2010	2011	2012	2013	2014	2015
Losses (%)	1.07	1.03	1.07	1.88	33.81	20.58	20.49	18.38

	Five Year Forecasting (2016-2020)				
Years	2016	2017	2018	2019	2020
Losses (%)	27.83	31.51	35.19	38.86	42.54
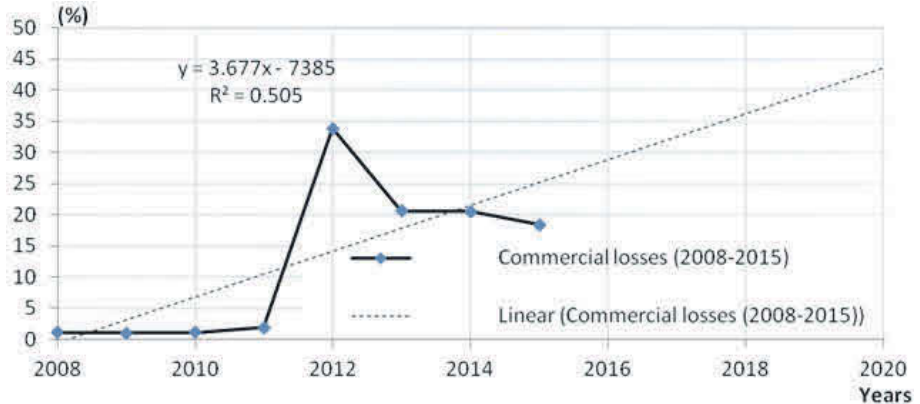
Fig. 2: System losses. The dotted line is the trend line of the commercial losses (2016-2020). The straight line is the existing commercial losses (2008-2015).

6 Proposition Towards Electricity Theft Reduction

The supplier of electricity shall seek to provide legal and economic actions on the consumers of the illegal energy [14, 15], and these efforts would be and not only limited to the followings:

1. Increase the penalties on electrical energy thefts in order to make the decision misuse of electrical energy is very risky and not economical at all.
2. Punishment and Deterrence: shall be proportional to the amount of electrical energy thefts with some minimum boundary limit.
3. Not allowing the consumers of electrical energy to install at their premises any kind of (black boxes etc.) without prior approval of the electrical energy suppliers.
4. Setting up a plan to change the existing energy meters to the smart type, and starting with the consumers who are already suspect of misuse of electrical energy.
5. Establish software programs to control the amount of consumed energy, and to indicate any unjustified deviation in electrical energy consumption.

6. Exchange the experience and methodology with other institutions and personnel involved in reduction of the electrical energy thefts.
7. Electrical energy prices shall be within a reasonable price for the low income populations to avoid the misuse of electrical energy, the price might be supported either by direct or indirect subsidy.

7 Results and Conclusions

An overview of electrical energy commercial losses has been presented in this paper. Moreover, definitions of the types of electrical energy losses have been introduced and evaluated. The mathematical model of the losses has been constructed along with the developed statistical indexes to evaluate the rate of changes of the variables.

The analysis of statistical indexes shows that, the amount of thefts of electrical energy is sometimes becoming one of the major parts of the commercial losses contents.The amount of thefts of electrical energy is drastically increased for the years (2012-2015) as presented in (Tab. 1) and in (2015) is slightly reduced to ($\approx$ 2%) due to the actions taken against the thefts.

In the case that quick and vital actions are not taken in nearest future, the value of commercial losses could reach -due to the thefts of electrical energy- to value of (42%) of the total energy losses value as deduced from the forecasting analyses as in (Tab. 3).

Additionally, the analyses show that the actions taken by the electrical energy providers are still not sufficient to reduce the illegal consumption of electrical energy. Therefore, recommendations concerning electricity theft reduction are presented, including; technical, economical and special regulations as presented in (section 6).

Bibliography

[1] N. E. Chang. Determination of primary-feeder loses. IEEE Trans. on Power Apparatus Systems, 87(12):1991–1994, December, 1968.
[2] N. Tawalbeh, A. Agha. Statistical Approach for the Analyses of Energy System Losses in Jordan. MESM'05 7th Middle Eastern Simulation Multiconference, :27–32, Porto, Portugal, 24–26th, October, 2005.
[3] T.S. Abdel-Salam, A.Y. Chikhani, R.Hackam. A new technique for loss reduction using compensating capacitors applied to distribution systems with varying load condition. Power Delivery, 9(2):819–827, April, 1994.
[4] A. Agha. Electrical Energy Commercial losses - Problems & Solutions. Electricity Regulatory Commission workshop, Amman, Jordan, 22 December, 2008.
[5] A. Agha, A. Alfaoury. Commercial losses in Jordanian Electrical System. 13th Int. Multi-Conf. on Systems, Signals & Devices (SSD) Conf. on Power Systems & Smart Energies, Leipzig, Germany, March 21-24, 2016.

[6] S. Pande, J.G. Ghodekar. Computation of Technical Power Loss of Feeders and Transformers in Distribution System using Load Factor and Load Loss Factor. (IJMSE), 3(9):22–25, June, 2012.

[7] HLK Current Transformers Catalogue 2004. HLK energietechniek B.V., www.hlk.nl.

[8] C.E.Lin, S.T.Chen, C.L.Huang. A direct Newton-Raphson economic dispatch. IEEE Trans. on Power Systems, 7(3):1149–1153, August, 1992.

[9] E. F.Hill, William D.Stevenson. An improved method of determining incremental loss factors from power system admittances and voltages. IEEE Trans. on Power Apparatus & Systems, 87(6):1419–1425, 1968.

[10] M. Mohsin, S. Om , K. Pankaj, K. Gopal. Real Time Study on Technical Losses in Distribution System. (IJAREEIE), 3(1):131–137, Special Issue, February 2014.

[11] National Electric Power Company (NEPCO), Annual Report, 2008 till 2015, Amman, Jordan.

[12] J. Rutkowski. The Minimum Wage: Curse or cure?. Human Development Economic Europe and Central Asia Region the World Bank, July 1, 2003.

[13] S. M. Ross. Introduction to Probability and statistics for Engineers and Scientists. 5th edition, Elsevier Inc. 2014.

[14] R. Jiang et al. Energy-Theft Detection Issues for Advanced Metering Infrastructure in Smart Grid. Tsinghua Science and Technology, 19(2):105–120, April, 2014.

[15] S. Sahoo, D.N. Nikovski, T. Muso, K. Tsuru. Electricity Theft Detection Using Smart Meter Data. Mitsubishi Electric Research Laboratories, Inc., 2015.

Biographies

Ayman Agha was born in Irbid- Jordan in. He received M.Sc. and Ph.D. degrees in electrical engineering from AGH University of Science and Technology - Cracow - Poland in 1989 and 1997 respectively. He joined Jordan Phosphate Mines Co. (JPMC) in 1989 as maintenance, Planner, Preventive maintenance engineer and at the project's department till 2000 year. From 2000 to 2004 he worked as a Studies and Design Dept. Manger in Riyadh/ KSA. In 2004 re-joined his previous work in JPMC, worked in Mega projects. He is member of several committees involved in conventional and non - conventional energy. Since 2013, he is Certified Consultant in Electrical Power Engineering and Projects (PQAC - JAE - Jordan). In 2014 he is pursuing an academic track at the Department of Electrical Engineering - Philadelphia University, Amman-Jordan.

Audih M. Alfaoury was born in Sult- Jordan in. He received M.Sc. and Ph.D. degrees in electrical engineering from Clij Napoca Technical University -Romania 1990 and 1995respectivly .He worked at the Ministry of Energy and Minerals Resources (MEMR) 1997 until 2004 during this period he worked in many area of inters such as preparation contracts, studies and analysis as well as regulation supervise ring in distribution ,transmission and generation systems in Jordan. Relates to this paper he participated with JICA team for one year to analysis and recommendations of distribution power system in Jordan. He is member of IET. From 2004 to 2015 he is pursuing an academic track at Philadelphia University and occupied head of electrical department for two times Including teaching in the power field the ,recently he is working for Al Balqa Applied university for power and energy department.

A. Al-Faoury, M. T. Lazim, H. Al-Khashashna

A Novel Dynamics Approximation method for Analysis and Design of DC Drive Systems

Abstract: A simplified frequency method for the parameters design of a thyristor speed regulator of a DC motor is presented. The approximation of dynamics of the thyristor controller by Pades expansion simplifies the design and gives more accurate results than that when using the approximation by means of Hurwitz polynomial approximation or other conventional approximation techniques. The proposed method gives a simple approach for analysis and design of DC drive system parameters without going to the more complicated methods suggested recently for solving the DC drive problems.

Keywords: DC machine, power electronics, speed and current controllers, closed loop control theory, Pade expansion.

Classification: 34A36, 34C23, 34D45

1 Introduction

DC motors are preferred to be used in many industrial applications such as steel rolling mills, electric trains, textile factories, plastics industries, paper mills and robotic manipulators. This is because they provide smooth and precise speed control that makes the DC drives more attractive than AC drives in such applications. However, most of DC drives require current and speed controllers to perform a given application task. A feedback automatic control systems for a speed control of DC motors usually consists of two basic feedback loops. The first loop is for the control of armature current of the motor, and the second loop is for the control of motor speed.

Usually, the current feedback loop includes a current transducer, which feeds a signal to a current controller having proportional-integral characteristic (PI). Similarly, for the speed feedback loop , it is necessary to have speed transducer, which is usually a tachogenerator feeding a signal to a PI controller. This means that, the structure of the feedback automatic control system is allocated and it is required to adjust the parameter of both the controller gains and the time constants, to ensure the desired dynamics of the entire system.

A. Al-Faoury, M. T. Lazim, H. Al-Khashashna: A. Al-Faoury, Al-Balqa' Applied University, Salt, Jordan, email: audihalfaoury@gmail.com , M. T. Lazim, H. Al-Khashashna, Philadelphia University, Amman, Jordan, emails: drmohamadtofik@yahoo.com, hudefah_hb@yahoo.com

The major problems in applying a conventional control algorithm to the controllers design are the effects of nonlinearity in DC motor drive system. The nonlinear characteristics such as friction and saturation in the DC motor itself and the control circuit of the converter could largely affect the performance of the controllers.

Several advanced model-based control methods such as variable structure control, model reference adaptive, and model order reduction techniques have been developed to reduce these effects. However, the performance of these methods depends on the accuracy of models and parameters and most of the approaches do not include the effects of the converter parameters which are very important issues.

Conventionally, the dynamics of the DC drive is usually described using time delays (or transportation lags). This fact leads to some difficulties in the analysis, synthesis and simulation of practical systems. The exact analysis of high order systems for stability problem is both tedious and costly.

To overcome the stability problem Hutton & Friedland [2] and Appiah [3] gave different methods, called stability based reduction methods which make use of some stability criterion. Other approaches in this direction included methods such as that given in references [4, 5] which do not make use of any stability criterion but always lead to the stable reduced order models. Bosley , Lees and others [6] had proposed method of reduction based on the fitting of the time moments of the system and its reduced model, but this method have a serious disadvantage that the reduced order model may be unstable even though the original high order system is stable. Some combined methods are also given in references [7, 8] in which the denominator of the reduced order model is derived by some stability criterion method while the numerator of the reduced model is obtained by some other methods [9]. The model order reduction method is a mixed method, where the numerator polynomial of reduced order model is obtained by using the stability equation method and numerator polynomial is obtained by the method proposed in reference [10].

In reference [11], a model order reduction method is proposed and its helps in finding the current controller gain value only.

It is found, from the above previous works, that the exact analysis of complex systems for stability problem is both tedious and costly. In order to derive a simple and accurate method of solution one can use some conventional and well known methods for this purpose. In this paper a simple method is proposed which helps in finding both the speed and current controller gain values using conventional control theory. The time delay is approximated by mean of the Pades expansion [12]. This derived mathematical model gives more accurate result than that given in any other techniques as will be shown in the following sections.

2 DC Motor Drive System

A simplified block diagram of the DC drive closed loop system that employs AC-DC converter (rectifier) using thyristor or any other power semiconductor devices elements is shown Fig. 1. The thyristor bridge converter gets its ac supply through a single- phase transformer and fast acting ac contactors. The dc output is fed to the armature of the dc motor. The field is separately excited, and the filed supply can be kept constant or regulated, depending on the need for the field weakening mode of operation.

Here, the feedback control system with the thyristor elements is, in fact, non-linear sample-data system with variable parameters. The block diagram of such system is shown in Fig. 2. In this case the thyristor unit is considered as sampler with a sampling period $T = \frac{1}{qf}$, where f = supply frequency and the factor (q) depends on the drive type, ($q = 1$ for half wave rectifier, $q = 2$ for full wave rectifier and corresponding by $q = 6$ for three phase rectifier).
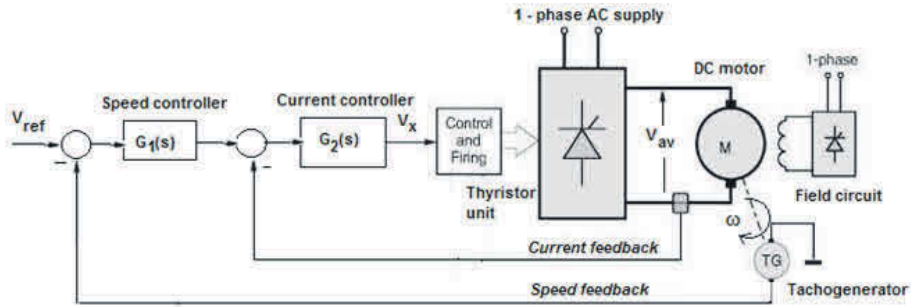

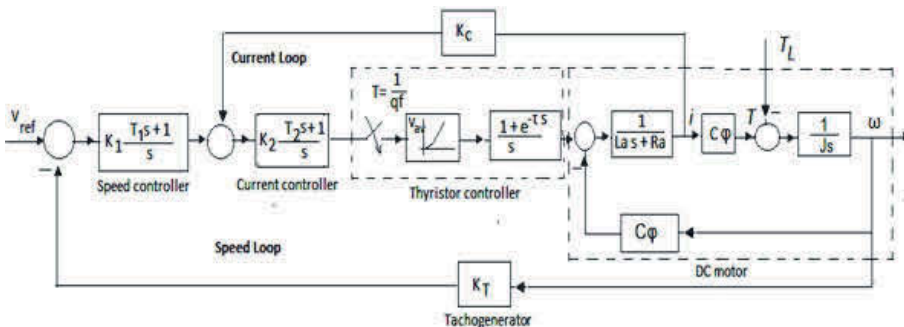**Fig. 1:** Typical electric DC drive components.

Fig. 2: Electric DC drive block diagram with speed and current controllers.

For full wave rectifier, the static characteristic of the thyristor unit is given by the following equation [2]:

$$V = \frac{V_{max}}{\pi}\left(1 - \cos\frac{\pi V_x}{V_0}\right) \tag{1}$$

The dependence (1) is depicted on Fig. 2, curve (1). It is obvious that the static characteristic is nonlinear and the gain of thyristor unit is not constant since $\frac{\partial V_{max}}{\partial V_x}$ will be varied according to V_x.

The function $\frac{\partial V_{max}}{\partial V_x} = f\left(\frac{V_x}{V_0}\right)$ is shown in the Fig. 3, curve (2). However in the present work a linear approximation of the static characteristic of the drive unit is considered, however, the gain of the unit $K_R = \frac{V_{av}}{V_x}$ is also assumed to be constant.

The zero order holder shown Fig. 2 represents a memory holding average voltage until next coming pulse from the triggering unit. Discreet properties of the thyristor controller can be replaced by means of time delay in the form of transfer function given by:

$$G_R = \frac{V_{av}(s)}{V_x(s)} = K_R e^{-\frac{Ts}{2}} \tag{2}$$

In Fig. 1, the DC motor has a tachogenerator whose output is used for closing the speed loop. The motor is driving a load T_L considered to be frictional for this treatment. The output of the tachogenerator is filtered to remove the ripples to provide the signal, ω. The speed command ω is compared to the speed reference signal to produce a speed error signal. This signal is processed through a proportional-plus-integral (PI)
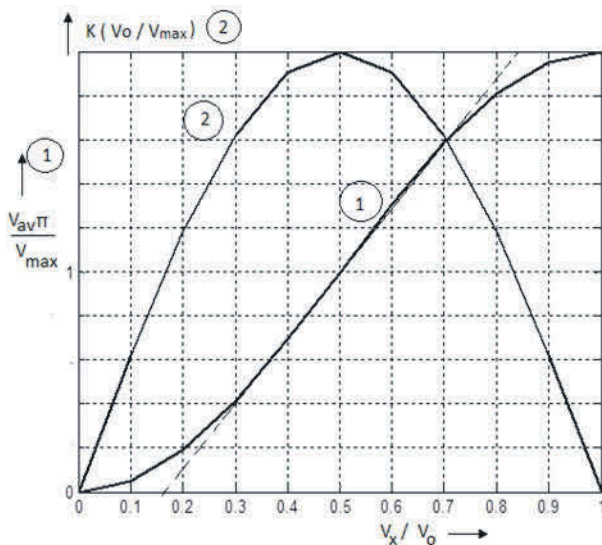

Fig. 3: Gain of thyristor unit.

controller to determine the torque command. The torque command is limited, to keep within the safe current limits and the current command is obtained by proper scaling. The armature current command i_a is compared to the actual armature command i_c to have a zero current error. The PI controller produces the equivalent control signal V_a when an error signal is occurred. The control signal accordingly modifies the triggering angle α to be sent to the converter for implementation.

The main objective of the present work is to simplify the procedure of parameters design on the base of linear theory of feedback control systems. This will be shown here in after.

3 Closed Loops Transfer Functions

A typical feedback automatic control system is as shown in Fig.4. This system consists of individual elements having transfer functions as follows,

For the DC armature controlled motor:

$$G_M(s) = \frac{\omega(s)}{V_{av}(s)} = \frac{K_M}{T_{EM}T_E s^2 + T_{EM}s + 1} \tag{3}$$

where:

$$T_{EM} = \frac{R_a J}{(C\phi)^2} , \quad T_E = \frac{L_a}{R_a}$$

The transfer function (TF) of the motor with respect to speed and load torque is:

$$G_T(s) = \frac{\Delta\omega(s)}{T_L(s)} = \frac{R_a}{C\phi} \frac{T_E s + 1}{T_{EM}T_E s^2 + T_{EM}s + 1} \tag{4}$$

The (TF) of thyristor unit may be approximated by the well known Pade's expansion as:

$$G_R = \frac{V_{av}(s)}{V_x(s)} = K_R\, e^{-\frac{Ts}{2}} = K_R\, \frac{1 - \frac{1}{4}Ts}{1 + \frac{1}{4}Ts} \tag{5}$$
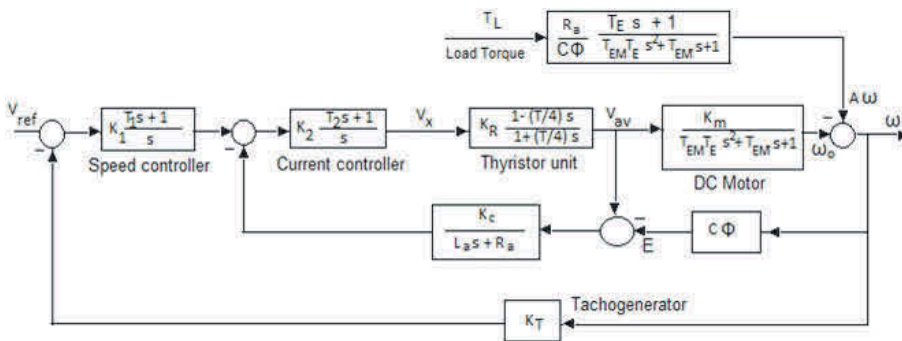

Fig. 4: Block of the DC drive system with speed and current controllers.
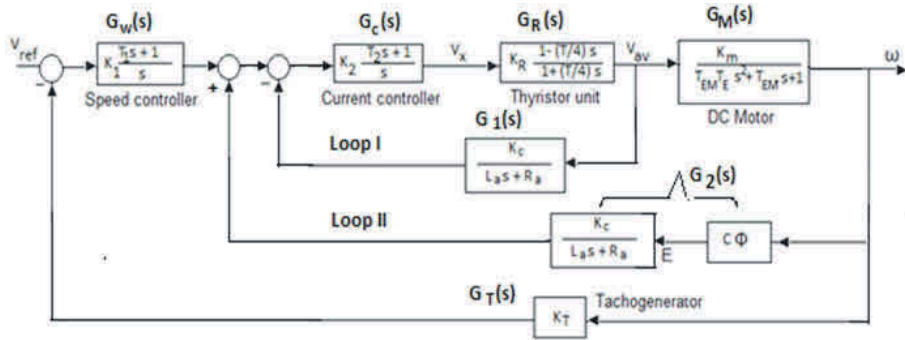
Fig. 5: Simplified block diagram and the transfer functions of the DC drive.

The transfer function of the current controller and speed controller has proportional-integral character given by [13–15]:

$$G_C = K_2 \frac{1 + T_2 s}{s} \tag{6}$$

$$G_\omega = K_1 \frac{1 + T_1 s}{s} \tag{7}$$

and the TF of the tachogenerator is:

$$G_T(s) = \frac{V_r(s)}{\omega(s)} = K_T \tag{8}$$

The block diagram corresponds to the DC drive system is shown in Fig. 4. This diagram can be rearranged by using the block algebra rules such that one can use bode plot for the design of the parameters. The modified block diagram is indicated on Fig. 5 which shows the performance of the system under no load condition.

The minor loop I represents the influence of a motor terminal voltage on current control, and consequently, the minor loop II, with positive feedback, represents the influence of the induced voltage E on the control of the motor current.

4 Design of Drive Prameters Using Bode Plot

The design procedure of DC drive parameters is given by solution of minor loops to ensure the stable condition of operation. This can be arranged as follows.

4.1 Minor loop of current control

The transfer function of the open loop is given by:

$$G_o^I(s) = \frac{K_{01}}{R_a} \frac{(1 + T_2 s)(1 - \frac{T}{4} s)}{s(1 + T_E s)(1 + \frac{T}{4} s)} \tag{9}$$

where $K_{01} = K_R K_2 K_C$.

Under the assumption that $T_E > \frac{1}{4}T$, the time constant of the current controller is taken to be $T_2 = T_E$, and the transfer function (TF) of the minor closed loop is:

$$G_I(s) = -\frac{G_C(s)G_R(s)}{1 + G_0^I(s)} = -\frac{R_a}{K_c}\frac{(1 + T_E s)(1 - \frac{T}{4}s)}{1 + 2\xi_1\tau_1 s + \tau_1^2 s^2} \tag{10}$$

where:

$$\tau_1 = \sqrt{\frac{R_a T}{4K_{01}}}, \quad \xi_1 = \frac{1}{2\tau_1}\left(\frac{R_a}{K_{01}} - \frac{T}{4}\right)$$

It is obvious that for a stable operation of the minor loop I, the following condition must be valid:

$$\frac{R_a}{K_{01}} > \frac{T}{4} \tag{11}$$

Moreover, the term $(1 - \frac{1}{4}Ts)$ leads to what is called "the non-minimal systems" and for these reasons it is convenient to use the Bode plot and to apply a Nyquist's stability criterion [13–15]. The procedure will be shown later.

4.2 Minor loop of current control

The open loop transfer function is:

$$G_o^{II}(s) = \frac{1 - \frac{1}{4}Ts}{(1 + 2\xi_1\tau_1 s + \tau_1^2 s^2)(1 + T_{EM}s + T_{EM}T_E s^2)} \tag{12}$$

Correspondingly the TF of the closed loop is:

$$G_{II}(s) = K_{II}\frac{G_I(s)G_M(s)}{1 - G_o^{II}(s)} = \frac{(1 - \frac{1}{4}Ts)(1 + T_E s)}{s(1 + a_1 s + a_2 s^2 + a_3 s^3)} \tag{13}$$

where:

$$K_I I = \frac{K_M R_a}{K_C(T_{EM} + 2\xi_1\tau_1 + \frac{1}{4}T)}$$

$$a_3 = \frac{\tau_1^2 T_{EM} T_E}{T_{EM} + 2\xi_1\tau_1 + \frac{1}{4}T}$$

$$a_2 = \frac{2\xi_1\tau_1 T_{EM} T_E + \tau_1^2 T_{EM}}{T_{EM} + 2\xi_1\tau_1 + \frac{1}{4}T}$$

$$a_1 = \frac{T_E T_{EM} + 2\xi_1\tau_1 T_{EM} + \tau_1^2}{T_{EM} + 2\xi_1\tau_1 + \frac{1}{4}T}$$

The final arrangement leads to the transfer function of open loop of the overall system:

$$G_0(s) = G_{II}(s)G_\omega(s)G_I(s) = K\frac{(1 - \frac{1}{4}Ts)(1 + T_E s)(1 + T_1 s)}{s^2(1 + a_1 s + a_2 s^2 + a_3 s^3)} \tag{14}$$

From equation (14), it is obvious that the DC drive system with two PI controllers is a feedback automatic control system of type 2. It is required to adjust the parameters K_1, K_2, T_1, T_2 and K_C in such a manner as to ensure the stability of operation as well as to obtain better and acceptable transient process. The transient process is evaluated in the frequency domain by the well-known cross over frequency and phase margin techniques. When the bode plot of equation (14) is drawn, the value of open loop gain can be found as:

$$K = \frac{K_1 K_M K_T R_a}{K_C(T_{EM} + 2\xi_1 \tau_1 + \frac{1}{4}T)} \tag{15}$$

where K_1 and K_C which are unknown parameters and consequently τ_1 the time constant of the speed controller can be determined. Now by using equation (9), the unknown parameters like T_2 and K_2 can also be determined.

4.2.0.1 Application of the method:

The design procedure under investigation is applied for the case of DC armature controlled motor with permanent magnet excitation with parameters presented in appendix I.

The thyristor controller unit, which is in this case, is full-wave rectifier of 50 Hz supply frequency having a sampling period $T = \dfrac{1}{2f} = 0.01s$. For the given parameters of the DC motor under consideration, the time constant of the current controller $T_2 = T_m$. The transfer function (9) is:

$$G_0^r(s) = \frac{K_{01}}{R_a} \; \frac{1 - \frac{1}{4}Ts}{s(1 + \frac{1}{4}Ts)} \tag{16}$$

The Bode plot is shown in Fig. 6 where the gain $\dfrac{K_{01}}{R_a} = 150$ and the gain margin and the phase margin are $P_m = 76$ and $\Delta\varphi = 50$.This is a sufficient value in order to fulfill the condition given in equation (1). The step response and pole-zero map are shown in Fig. 7,while the magnitude response and system noise are shown in Fig. 8.

Now with time constant $T_1 = 0.0041s$ and damping ratio $\xi = 0.52$, the transfer function of the minor loop I is:

$$G_0(s) = \frac{0.211}{K_C} \; \frac{(1 - 0.0025s)(1 + 0.00865s)}{1 + 0.0043s + 1.7 \times 10^{-5}s^2} \tag{17}$$

In the next step the transfer function of the minor loop II is calculated:

$$G_{rr}(s) = \frac{14.8}{K_C} \; \frac{(1 - 0.0025s)(1 + 0.00865s)}{1 + 0.007s + 2.6 \times 10^{-5}s^2 + 7.1 \times 10^{-8}s^3} \tag{18}$$
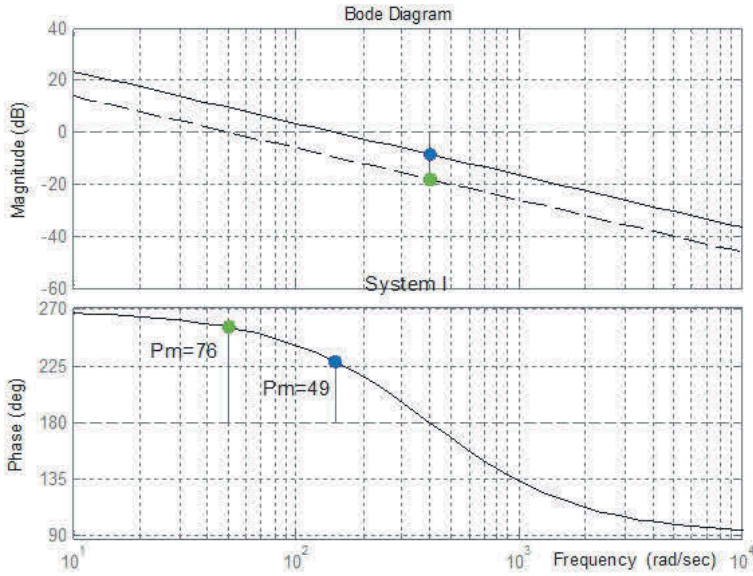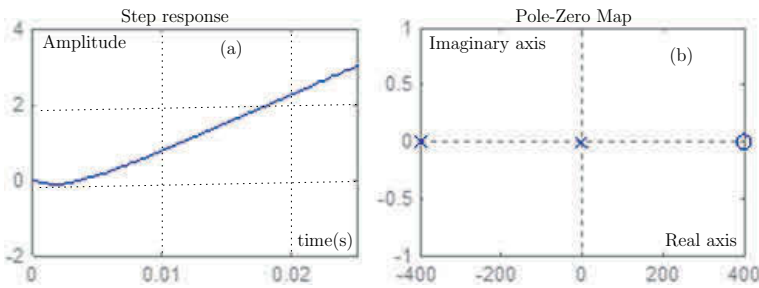
Fig. 6: Bode plot for equation (16).

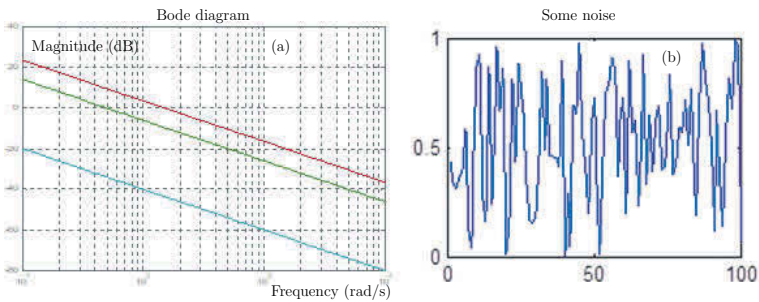**Fig. 7:** (a) Step response, and (b) pole-zero map of equation (16).

Fig. 8: (a) Magnitude response, and (b) Noise in system I of equation (16).
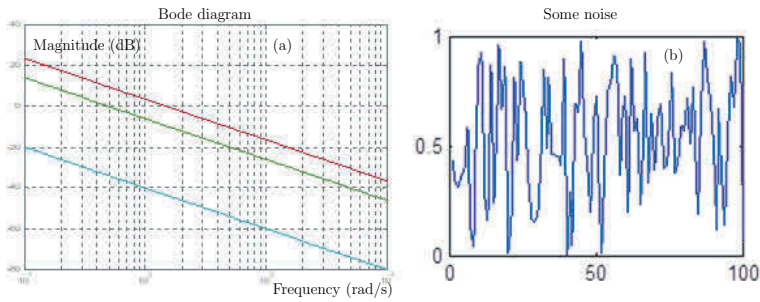
Fig. 9: Bode plot for main open loop.

In equation (18), the term 7.1×10^{-8} can be neglected since it is very small, therefore the final form of overall system open loop TF is:

$$G_{rr}(s) = \frac{14.8 K_1 K_r}{K_C} \frac{(1 - 0.0025s)(1 + 0.00865s)}{s^2 (1 + 0.00754s + 2.6 \times 10^{-5} s^2 + 7.1 \times 10^{-8} s^3)} \quad (19)$$

The Bode plot of equation (19) is shown in Fig. 9, from which, the phase margin is found to be =68. The time constant T_1 is designed to be the range of the medium part of frequency characteristic per one decade. The gain of the open loop is $K = 750$, and the ratio of gains $K_1 K_c = \dfrac{50.6}{K_r}$. In the previous step $K_{01} = K_R K_2 K_C = 31$ has been determined and consequently $K_2 K_C = \dfrac{31}{K_R}$. The time constant of speed controller is $T_1 = 0.066s$. and the time constant of the current controller is $T_1 = 8.65 \times 10^{-3}s$.

5 Conclusion

A more accurate mathematical description of dynamics of the thyristor unit has been taken into consideration when designing the parameters. For such mathematical mode it is preferable to use Bode plot as engineering approach to adjust the parameters of the feedback system. Furthermore, a block diagram of the feedback system has been derived including the effect of the induced voltage on current control. The frequency domain method facilitates the design of optimal parameters graphically and the effect of variation of parameters on stability can be also judged. The thyristor unit gain variation and consequently discontinuous current operation are not taken into consideration. An adaptive current controller solves this problem. To treat the design of the parameters rigorously a simulation of the thyristor speed regulator as a sampled-data automatic control system by means of Mat- lab program is needed. The simulation technique of the thyristor speed regulator is necessary as a preliminary design before production of speed regulator prototype.

Bibliography

[1] P.Idberq, A.Nerman. Motor Drive with Thyristor Convertors. Esselte Studium, Royal Swedish Institute of Technology, research report, Sweden, 1985.

[2] M.F. Hutton and B. Friedland. Routh approximations for reducing order linear time invariant systems. IEEE Trans. on Automatic Control, 20:329–337, 1975.

[3] R.K. Appiah. Linear model reduction using Hurwitz polynomial approximation. Int. J. Control, 28, (3):477–488, 1978.

[4] Y. Shamash. Truncation method of reduction: a viable alternative. Electronics Letters, 17:97–99, 1981.

[5] P.O. Gutman, C.F. Mannerfelt and P. Molander. Contributions to the model reduction problem. IEEE Trans. on Automatic Control, 27:454–455, 1982.

[6] M.J. Bosley and F.P. Lees. A survey of simple transfer-function derivations from high order state variable models. Automatica, 8:765–775, 1972.

[7] Y. Shamash. Model reduction using the Routh stability criterion and the Pade-approximation technique. Int. J. Control, 21:475–484, 1975.

[8] T.C. Chen, C.Y. Chang and K.W. Han. Reduction of transfer functions by the stability equation method. Journal of Franklin Institute, 308:389–404, 1979.

[9] Bai-Wu Wan. Linear model reduction using Mihailov criterion and Pade approximation technique. Int. J. Control, 33:1073–1089, 1981.

[10] T.C. Chen, C.Y. Chang and K. W. Han. Model Reduction using the stability-equation method and the Pade approximation method. Journal of Franklin Institute, 30(9):473–490, 1980.

[11] K. Ramesh, A. Nirmalkumar and G. Gurusamy. Design of Digital IIR filters with the Advantages of Model Order Reduction Technique. Int. Journal of Electronics, Communications and Computer Engineering, 1(2)117–122, 2009.

[12] K.Ramesh, K.Ayyar, A.Nirmalkumar, G.Gurusamy. Design of Current Controller for Two Quadrant DC Motor Drive by Using Model Order Reduction Technique. (IJCSIS) Int. Journal of Computer Science and Information Security, 7(1), 2010.

[13] J.Truxall. Synthesis of automatic control system. McGraw Hill Book company, New York, USA, 1961.

[14] Shengqiang Li and Xiaodong Liang. Modeling DC Motor Drive Systems in Power System Dynamic Studies. IEEE Trans. on Industry Applications, 51(1), 2015.

[15] J. Yao, Z. Jiao, and D. Ma. Adaptive Robust Control of DC Motors With Extended State Observer. IEEE Trans. on Industrial Electronics, 61(7):3630–3637, 2014.

APPENDIX I

List of symbols

t: Time (s)

$C = \frac{PN}{2\pi a}$: Motor constructional constant

J: Polar moment of intertia of armature

$K_m = \frac{1}{C}$: gain of the motor L_a: Armature circuit inductance (H)

R_m: Armature circuit resistance (Ω)

T_E: Electromagnetic time constant of a motor (s)

$T_E M = \frac{R_m J}{(C\phi)^2}$: Electromechanical time constant of a motor (s)

V_{av}: Average output voltage of the thyristor (V)

V_{max}: Maximum voltage (rectified) (V)

V_0: Reference voltage of triggering circuit (V)

V_x: Control voltage of the triggering circuit (V)

ω: Angular speed (or angular frequency in Bode plot) (rad/s)

T_L: Load torque (Nm)

T: Sampling period (s)

$G(s)$: Transfer function

ϕ: Magnetic flux (Wb)

$\varphi(\omega)$: phase frequency

Parameters of DC armature controlled motor with permanent magnet excitation

Motor of type 3 SHAT 112M used in NC system:

Rated torque 47 Nm

Rated voltage 67 V

Rated speed 52.4 rad/s

Rated current 47 A

Max. Torque 280 Nm

Armature resistance $R_a = 0.211\Omega$

Armature inductance $L_a = 1.83 \times 10^{-3}$ H

Moment of inertia $J = 0.033$ Kg m^2

Biographies

Audih Al-Faoury was born in Sult-Jordan. He received M.Sc. and Ph.D. degrees in electrical engineering from Cluj Napoca Technical University-Romania 1990 and 1995 respectively. He worked at the Ministry of Energy and Minerals Resources (MEMR) 1997 until 2004 during this period he worked in many area of inters such as preparation contracts, studies, analysis and review regulation in distribution, transmission and generation systems in Jordan. He was also an participant of JICA team for one year to analysis and recommendations of distribution power system in Jordan. He is member of IET. From 2004 to 2015 he is pursuing an academic track at Philadelphia University and occupied head of electrical department for two times Including teaching in the power field Recently he is assistant dean of engineering faculty of Al Balqa Applied University and a staff member of power and energy department and teaching all courses in power system such as protection, operation, transmission lines design, stability and reliability, electromagnetics as well as power system analyses.

Mohammed. Tawfiq Lazim graduated from Engineering College, University of Baghdad, Iraq in1967 .He received the M.Sc. degree in from University of Baghdad, Iraq in 1975 and the Ph.D in electrical and electronics engineering from the university of Bradford, West Yorkshire, England in 1981, all in electrical and electronics engineering. He was assistant professor and head of electrical and electronics engineering department at the Military Engineering College, Iraq from 1981 to 1991 and head of computer engineering department at the Mansoor University, Iraq from 1991 to 1999. He worked at the Nahrain University, Baghdad, Iraq as associate professor and head of electronics and communication engineering department from 1999 to 2007.He joined the Faculty of Engineering, Philadelphia University, Jordan in 2007, and is now Professor of Electrical and Power Electronics Applications in the electrical engineering department. He is the author of four books and translator to Arabic of thee books.

Huthaifa Alkhashashna Electrical Engineering Department, Philadelphia University, Jordan. He was graduated from Electrical Engineering Department, Jordan University of Science and Technology (JUST), Jordan in 2012. He joined the Faculty of Engineering, Philadelphia University, Jordan in 2014. He has strong knowledge and experience in electrical machines and drives, He is currently a post graduate student at Mechatronics Engineering Department, Philadelphia University at the final research period.

J. Loukil, F. Masmoudi and N. Derbel

Third order Model and Identification of Lead Acid Batteries Using Meta-Heuristic Algorithms and Experimental Measurements

Abstract: Today, lead acid batteries are even studied in an intensive way thanks to their economic interest related to their use in renewable energies and automotive sectors. The modelling of lead acid batteries can be done in several ways depending on the accuracy and system requirements. An accurate electrical model is very helpful for simulation, modelling, optimization, and control of battery cell systems. In this paper, an effective and suitable mathematical model of a battery cell has been treated. The implementation of the third order model well describes the internal aspect of the battery and reveals a good compromise between the precision and the complexity. In order to imitate the real behaviour for this kind of batteries and then to extract the charge and the discharge characteristics, an identification algorithm of internal parameters of the proposed model has been suggested with several methods: (i) the identification using electrical characteristics established by the manufacturer datasheet, (ii) the identification through a genetic algorithm and (iii) the identification using a particle swarm optimization.

Using Matlab-Simulink, recovered simulations have been compared to those provided by POWER KINGDOM 7Ah-12V battery's datasheet. Then, the behaviour of the third order model has been validated by an experimental test under real conditions. The setup is based on voltage and current sensors. An Arduino Board is used to acquire data from sensors and send them to the computer.

The influence and variation effects of the temperature and the discharge current have been evaluated for the proposed model.

Obtained results show an acceptable correspondence with the data issued by the manufacturer, the genetic algorithm, the particule swarm optimisation and the experimental work. These methods become an useful tool for researchers to determine easily the optimal internal parameters of lead acid batteries.

Keywords: Lead acid battery, Third order model, Internal parameters, Datasheet, Experimental work, Genetic algorithm, Particle swarm optimization.

Classification: 65C05, 62M20, 93E11, 62F15, 86A22

J. Loukil, F. Masmoudi and N. Derbel: J. Loukil, F. Masmoudi and N. Derbel: , [1] Control & Energy Management Laboratory (CEMLab), University of Sfax, Sfax Engineering School, Sfax, Tunisia , [2] Digital Research Center of Sfax (CRNS), emails: jihen.loukil@gmail.com, ferdaous.masmoudi@gmail.com, n.derbel@enis.rnu.tn

1 Introduction

Currently, the electrical energy consumption is greatly increasing. Therefore looking for an other attractive alternatives is necessary. Today, renewable energies are considered as inexhaustible sources that can be substituted for future energy demand. However, the production by this clean systems is very fluctuant and depends especially on weather conditions. To overcome this problem, the exploitation of storage devices is critical to maintain the stability and the supply of the load power in case of a failure of this renewable energy systems. Several types of batteries are now subject to further development and research.

Among these, the lead acid battery is considered as an effective technology. It remains the dominant battery chemistry for several applications. It is the best choice of chemical storage systems thanks to the low cost, the good recyclability, the low auto– discharge current and the favorable electrochemical characteristics [1, 2].

Battery modeling has received an important attention in recent years [1, 5]. So, The main challenge of researchers is to improve an efficient battery model that can be able to describe and to estimate effectively the behaviour and the performance of this device under different operating conditions. Lead acid battery cell modeling involves the formulation of the non–linear of its electrical characteristics. Therefore, numerous models have been developed such as generic models [3, 4], electrochemical models [5, 6], and electric circuit based models [7–9]. They vary from models with simple assumptions to advanced models accompanying with several physical variables.

The electric-circuit based model is one of the most commonly used in the literature. It is more suited to well describe the battery charge and discharge status. Moreover, it can be easily integrated with control algorithms. For the modeling of lead acid batteries, various equivalent circuit models are presented like Thevenin model [10, 11], the Third order model, Randle and Copetti model, etc. [12–14].

The third order model is the focus of this paper. It is widely used. It well describes the behaviour of the battery and takes more in consideration variations of the temperature and the state of charge (SOC) [15].

In the literature, several investigations have been developed to identify different parameters of the battery model. Indeed, it is very important to discover these unknown parameters in order to estimate the perfection degree, the state of charge, the state of health and the quality of this device. In [16], an algebraic method is used for extracting parameters of Thevenin's equivalent circuit for any initial condition. Fairweather, and Foster demonstrated that a Pseudo Random Binary Sequence excitation is an useful tool [17]. It lead to the identification of specific parameters for Valve Regulated Lead Acid batteries. Tremblay and louis have shown how parameters of a Generic battery model can easily be determined from a manufacturer's discharge curve. In [18], a technique called an impedance spectroscopy has been described in order to deduce unknown components of the model.

In this paper, a POWER KINGDOM battery module with a nominal voltage of 12V and a nominal capacity of 7Ah has been studied.

In order to refine the electrical characteristics of a battery, solving the problem of battery parameter identification has been addressed by the use of the producer datasheet, the genetic algorithm (GA), and the particle swarm optimization (PSO).

2 Mathematical model of a lead acid battery

Developing an equivalent circuit model for the battery is necessary to understand the physical configuration of battery's cell as well as electrical characteristics of each component [19, 20].

The network of the following model of the battery is described by Fig. 1. It has been designed to have the ambient temperature T_a and the charge/discharge current I as inputs, and the voltage V_{batt}, the electrolyte temperature T_e, and the state of charge SOC as outputs. The battery model has two operation modes: charge and discharge. The battery is considered in discharge mode when the current is negative, and in charge mode when the current is positive.

The temperature, the battery storage capacity, the age life, the depth of charge (DOC), the state of charge (SOC), the state of health (SOH), and the charge and discharge currents are main factors that affect battery performances. Thus, they must be analyzed and treated. The state of charge (SOC) is defined as the percentage of the energy stored in a fully charged battery. The depth of charge (DOC) measured the remaining usable charge. The state of health is defined to show how weak the battery. It represents the percentage of remaining capacity to the initial capacity when the battery is new.

The third order model takes into consideration the most of these parameters. It can well reflect the dynamic behaviour of the battery. The electrical equivalent circuit of the third order model is shown in Fig. 2. The model is composed by two parts: a main branch which describes the battery dynamics under operating conditions. It is formed of an electromotive force E_m, a resistance R_2 placed in series with the bloc R_1, and C_1. The second part is the parasitic branch. Not all the energy issue to the battery
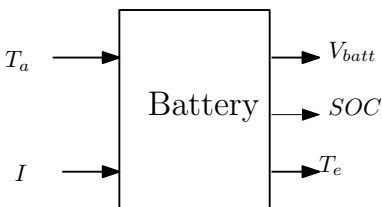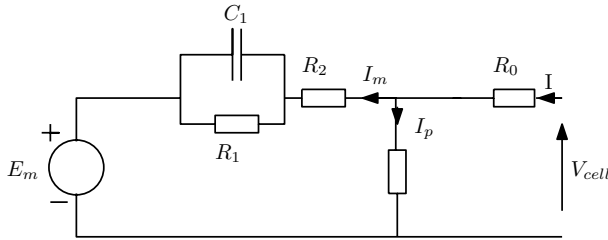

Fig. 1: Battery model

Fig. 2: Third order model

will be stored, part of this will be lost for different reasons such as water electrolysis. A parasitic branch presents the energy loss, it approximates the behaviour of the battery at the end of the charge.

- E_m (V) represents the open circuit voltage.
- R_1 (Ω) resistance affects the battery during discharging.
- C_1 (F) describes the transient dynamic.
- R_2 (Ω) resistance affects the battery during charging.
- I_p (A) presents the parasitic branch current.
- R_0 (Ω) is the terminal resistance.

The presented model illustrates one cell of the battery. To obtain the required operating battery voltage (12 V), cells should be connected in a serie arrangement. Therefore, the output of the cell should be multiplied by the number of series cells (6 cells).

Different elements of the equivalent circuit are based on nonlinear equations. All these include parameters that depend on the temperature of the electrolyte T_e, the discharge current and the state of charge SOC [21–25].

- Main branch voltage E_m: The internal electromotive force E_m should be expressed according to the following equation:

$$E_m = E_{m0} - K_e T_e (1 - SOC) \tag{1}$$

  - E_{m0} (V): Internal electromotive force at full charge
  - K_e (V/ K): Constant
  - T_e (K): Electrolyte temperature
- Main branch resistance R_1: The resistance R_1 varies with DOC. It increases exponentially when the battery will be exhausted during a discharge. It can be approximated by:

$$R_1 = -R_{10} \ln(DOC) \tag{2}$$

  - R_{10} (Ω) : Constant

–   Main branch capacitance C_1: The relationship between the resistance R_1, and the main branch capacitance C_1 is described as follows:

$$C_1 = \frac{\tau_1}{R_1} \tag{3}$$

  – τ_1 (s): Main branch time
  τ_1 models the voltage delay when the battery current change.
–   Main branch resistance R_2: It increases exponentially when the battery becomes full. It can be determined as follows:

$$R_2 = R_{20}\frac{\exp[A_{21}(1-SOC)]}{[1+\exp\frac{A_{22}I_m}{I_n}]} \tag{4}$$

  – R_{20} (Ω): constant
  – A_{21}, A_{22}: constants
  – I_m (A): Main branch current
  – I_n (A): Nominal battery current
–   Terminal resistance R_0: In the following, the expression of the resistance seen at the battery terminals R_0 is given by:

$$R_0 = R_{00}[1+A_0(1-SOC)] \tag{5}$$

  – R_{00} (Ω): The value of R_0 for SOC=1
  – A_0: Constant
–   Parasitic branch current I_p: The parasitic current is very small under most conditions, except at high state of charge.
  I_p is expressed as follows:

$$I_p = V_{PN}G_{P0}\exp\left[\frac{V_{PN}}{V_{P0}} + A_p\left(1-\frac{T_e}{\theta_f}\right)\right] \tag{6}$$

  – V_{PN} (V): Voltage of parasitic branch
  – G_{P0}, A_p, V_{P0}: Constants
  – θ_f: Electrolyte freezing temperature $\theta_f \in [-35\,°C, -40\,°C]$
–   Voltage parasitic branch V_{PN}: The voltage of the parasitic branch V_{PN} can be determined as follows:

$$V_{PN} = E_m + V_R + V_2 \tag{7}$$
$$V_R = R_1I_1 \tag{8}$$
$$V_2 = R_2I_m \tag{9}$$

  – V_R (V): Voltage of resistance R_1.
  – V_2 (V): Voltage of resistance R_2.
  – I_1 (A): Current of the resistance R_1.

- The state of charge:

$$SOC = 1 - \frac{Q_e}{C(0, T_e)} \tag{10}$$

- The depth of charge:

$$DOC = 1 - \frac{Q_e}{C(I, T_e)} \tag{11}$$

- Q_e: Extracted charge
- $C(0, T_e)$ (Ah): Nominal capacity
- $C(I, T_e)$ (Ah): Used capacity

The battery's charge expires prematurely, when the discharge current is rather important.

The expression of the extracted charge Q_e is given by:

$$Q_e = -\int_0^t I_m \mathrm{d}t \tag{12}$$

The equation corresponding to the battery's capacity:

$$C(I, \theta) = \frac{[K_c C_0 (1 - \frac{T_e}{\theta_f})^\varepsilon]}{[1 + (K_c - 1)(\frac{I}{I_n})^\delta]} \tag{13}$$

The relation between currents I, I_p, and I_m is:

$$I_m = I - I_p \tag{14}$$

- I_m (A): Main branch current
- I_p (A): Parasitic current
- I (A): Charge/Discharge current

The dynamic equation of I_1 can be expressed as follows:

$$\dot{I_1} = \frac{I_m - I_1}{\tau_1} \tag{15}$$

The output voltage of one cell is:

$$V_{CELL} = V_{PN} + R_0 I \tag{16}$$

The thermal model tracks the battery's electrolyte temperature. This model allows to estimate the change of the temperature due to the ambient temperature and the power loss. The dynamic equation of the cell temperature can be estimated by this equation:

$$T_e = T_{einit} + \int_0^t \frac{(P_s R_\theta - (T_e - T_a))}{(R_\theta C_\theta)} \mathrm{d}t \tag{17}$$

- T_a (K): Ambient temperature.

- T_{einit} (k): Initial temperature of the electrolyte
- R_θ ($°C$/W): Thermal resistance
- C_θ (KJ/$°C$): Thermal capacitance
- P_s (J): Power loss

When the battery is discharging, or charging, there is a current lost through the battery, which produces heat. The power loss can be calculated as follows:

$$P_s = V_R I_1 + R_0 I^2 \tag{18}$$

3 Determination of unknown parameters

Considering the model mentioned above, there are unknown electrical parameters that must be defined. These parameters are E_{m0}, K_e, R_{10}, R_{00}, A_0, K_c, C_0, ε, δ, R_{20}, A_{21}, A_{22}, R_θ, C_θ, G_{P0}, V_{P0}, A_P. Three main approaches have been used to solve the parameter identification problem. In a first part, the determination of these quantities is based on solving some equations using manufacturer's information. In the second part, an identification methodology through a meta-heuristic search: genetic algorithm (GA) and particle swarm optimization (PSO) will be proposed.

3.1 The manufacturer's datasheet

The proposed battery to be studied in this paper is the lead acid marketed under the reference POWER KINGDOM 7Ah-12V. Electrical performances of the battery consist of measuring the discharge characteristic (V, t) in a fixed temperature and in a fixed current value. This performance provides a method for reporting the electrical behaviour of battery cells. The manufacturer includes in the datasheet the evolution of the discharge characteristic curve which is supplied by the battery with different values of the discharge current in an ambient temperature $25°C$ as shown in Fig. 3.

Electrical specifications provided by the manufacturer in the datasheet are summarized in Table I.

3.2 Identification using the datasheet

To identify internal parameters of a battery cell, the basic idea is to exploit measures provided by the manufacturer's datasheet. The determination of these quantities is based on solving a system of equations.

The (V, C) characteristic curve of the battery defined in Fig. 4 illustrates some key points namely:
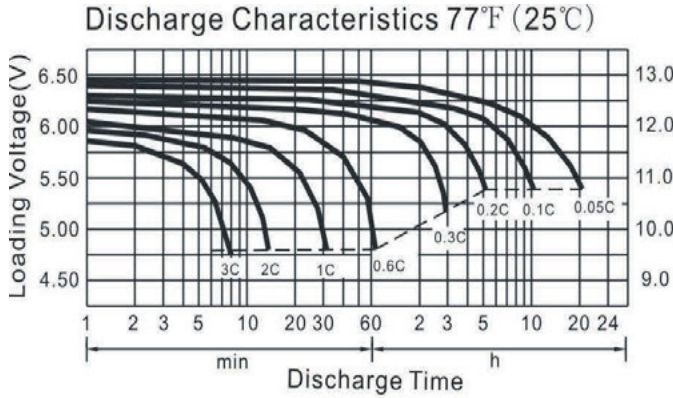- The Nominal voltage , coordinated $(a) = (V_3)$.

Fig. 3: Discharge Characteristics for different discharge currents

Tab. 1: Electrical specifications of battery 12V/7Ah

Electrical quantities	values
Nominal voltage	12 V
Nominal Capacity	7 Ah
Ambient temperature	$25\,°C$
Maximum discharge current	2.1 A
Internal resistance	$22\,m\Omega$

- The Maximum capacity, coordinated $(b) = (V_4)$.
- The Exponential voltage, coordinated $(c) = (V_2)$.
- The discharged current , coordinated $(d) = 1.19A$.
- The Voltage at 10 % maximum capacity, coordinated $(e) = (V_1)$.
- The Fully charged voltage, coordinated $(f) = (V_0)$.

The identification of the unknown parameters $(E_{m0},\ K_e,\ R_{00},\ R_{10},\ A_0\ )$ of the equivalent electrical model is based on solving the system formed by the following relationships.

$$E_{m0} = V_0 \tag{19}$$

$$K_e = \frac{V_1 - V_2}{T_e} \tag{20}$$

$$R_{00} = \frac{V_1 - V_2}{I} \tag{21}$$

$$R_{10} = \frac{V_0 - V_1}{I} \tag{22}$$

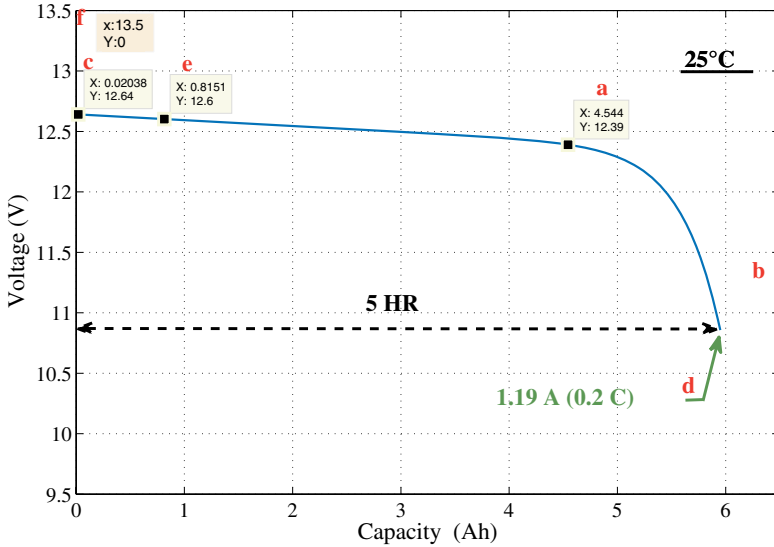$$A_0 = \frac{V_3 - V_4}{V_0 - V_2} \tag{23}$$

$$\tag{24}$$

Fig. 4: battery datasheet: I=1.19A, C=5.95Ah

Tab. 2: Thermal parameters

Parameters	Value obtained from datasheet
$R_\theta(°C/W)$	10
C_θ (KJ/$°C$)	0.9

The proposed thermal model depends on the implementation of the battery in his environment. It is composed by a simple thermal resistance R_θ, thermal capacitance model C_θ. These two parameters can be obtained by the manufacturers of batteries or can be derived experimentally.

The mentioned equation of the parasitic branch contains parameters (G_{P0}, A_p, V_{P0}) that should be determined. To identify these constants, the electrolyte temperature can be estimated equal to the ambient temperature, and the battery must be considered completely full. For this reason, it can be assumed that the main branch current is zero.

The constant G_{P0} is considered very small, on the order of $2 \times 10^{-12} \ \Omega^{-1}$.

For computing the unknown parameter A_p, several tests have been demonstrated that :

$$I_p(30\%) \approx 10I_p(30\%) \tag{25}$$

The identification of V_{P0} can be calculated by using equation (6) considering I_p is equal to the nominal discharge current which means that the battery is completely full (I_m=0).

Tab. 3: Parameters from different discharge curve

Discharge current(A)	Temperature (°C)	Capacity (Ah)
0.35	25	7
0.35	40	8.4
0.65	25	6.51
1.19	25	5.95

To find the rest of electrical parameters, a battery test should be realised in four times and in different conditions $C(I_1, T_a)$, $C(I_1, T_2)$, $C(I_2, T_a)$, $C(I_3, T_a)$.

Table III illustrates these different tests.

The adopted idea in determining the unknown parameters of a battery cell is to exploit values from different test showing in table III.

Starting by computing the temperature coefficient α:

$$C(I, \theta) = (1 + \alpha \Delta \theta) C(I, \theta_0) \tag{26}$$

The following relation can be estimated between the two parameters ε and α:

$$\varepsilon = \alpha(T_a - \theta f) \tag{27}$$

Then, the unknown parameter C_0 can be calculated:

$$C(I_n, \theta_n) = C_0 \left(1 - \frac{\theta_n}{\theta_f}\right)^\varepsilon \tag{28}$$

To determine K_c and δ, it is necessary to calculate: $C(I_1, T_a)$ and $C(I_2, T_a)$:

$$C_1 = C(I_1, T_a) \tag{29}$$

$$C_2 = C(I_2, T_a) \tag{30}$$

$$C_1 = \frac{[K_c C_0 (1 - \frac{T_a}{\theta_f})^\varepsilon]}{[1 + (K_c - 1)(\frac{I_1}{I_n})^\delta]} \tag{31}$$

Equation (29) can be rewritten as follows:

$$\frac{C_1}{C_0(1 - \frac{T_a}{\theta_f})^\varepsilon} = \frac{K_c}{1 + (K_c - 1)(\frac{I_1}{I_n})^\delta} \tag{32}$$

Considering the following relation:

$$A = \frac{K_c}{1 + (K_c - 1)(\frac{I_1}{I_n})^\delta} \tag{33}$$

By developing equation (31), the parameter K_c can be expressed as follow:

$$K_c = \frac{A(1 - \frac{I_1}{I_n})^\delta}{1 - A(\frac{I_1}{I_n})^\delta} \tag{34}$$

Equation (32) is expressed in terms of the two unknown parameters: K_c and δ. To solve this problem, we can use equation (28):

$$C_2 = \frac{[K_c C_0 (1 - \frac{T_a}{\theta_f})^\varepsilon]}{[1 + (K_c - 1)(\frac{I_2}{I_n})^\delta]} \tag{35}$$

Rewriting equation (33):

$$\frac{C_2}{C_0 (1 - \frac{T_a}{\theta_f})^\varepsilon} = \frac{K_c}{1 + (K_c - 1)(\frac{I_2}{I_n})^\delta} \tag{36}$$

Considering the following relation:

$$B = \frac{K_c}{1 + (K_c - 1)(\frac{I_2}{I_n})^\delta} \tag{37}$$

By developing the equation (33), the parameter K_c can be expressed as follows:

$$K_c = \frac{B(1 - \frac{I_2}{I_n})^\delta}{1 - B(\frac{I_2}{I_n})^\delta} \tag{38}$$

Solving the system with the two relations (32) and (36), δ and K_c can be calculated.

3.3 Identification using a meta-heuristic algorithms

Sometimes, several parameters are not provided usually by the producer. Therefore, the identification of the model unknown parameters should be treated with an optimization process that can be able to adjust these quantities [26]. Recently, meta-heuristic algorithms have attracted significant attention. This paper proposes the use of a genetic algorithm and a particle swarm optimization. These algorithms should minimize an objective function. If this step is achieved, the model output could fit the experience to have a new generation of parameters. Figure 5 describes the process of identification through these two types of algorithms.

3.3.1 Identification using a genetic algorithm

GA is an adaptive heuristic search which is based on an analogy with the behaviour of chromosomes, and the evolutionary ideas of natural selection. It rely on bio-inspired
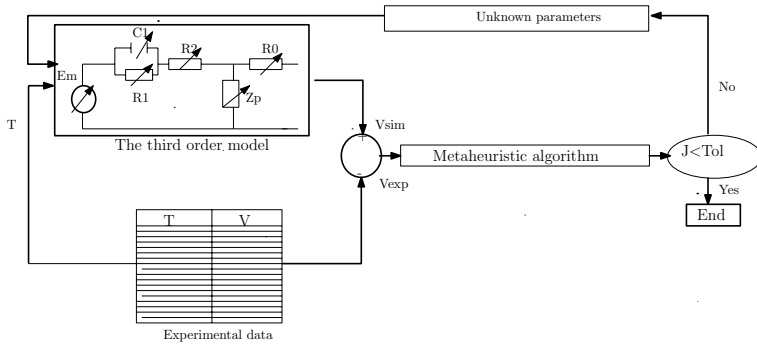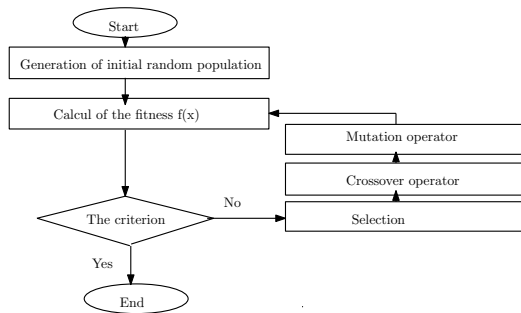
Fig. 5: Identification process.

Fig. 6: Flowchart of the genetic algorithm.

operators such as mutation, crossover and selection. Figure 6 shows the flowchart of a genetic algorithm.

3.3.2 Identification using a particle swarm optimization

PSO is a population based on stochastic optimization techniqueS inspired by the social behavior of a flock of bird. This metaphor has been explained that all particles in the swarm fly through an environment following the fitter members of the swarm and biasing their movement toward their good areas. The goal of this algorithm is to have all particles located at the optimum [27]. Figure 7 reveals different steps of this method.

In order to validate this step, an experimental test should be established. Figure 8 shows the test bench of discharging and charging a lead acid battery 12V/7Ah under real conditions.

It is composed by the following components:
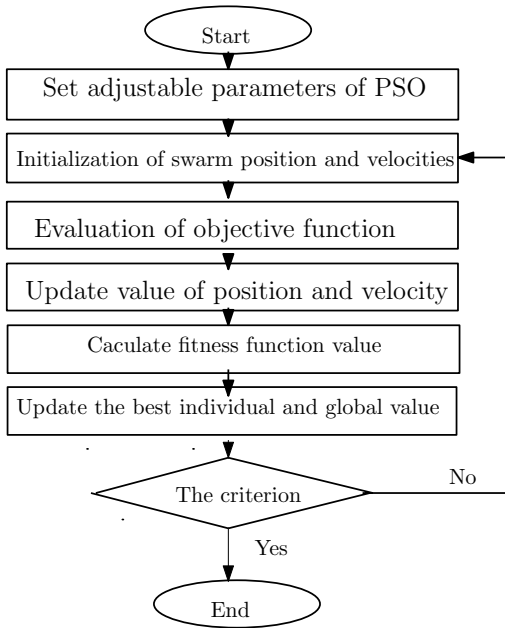−   Battery : Lead acid battery 12V/7Ah.

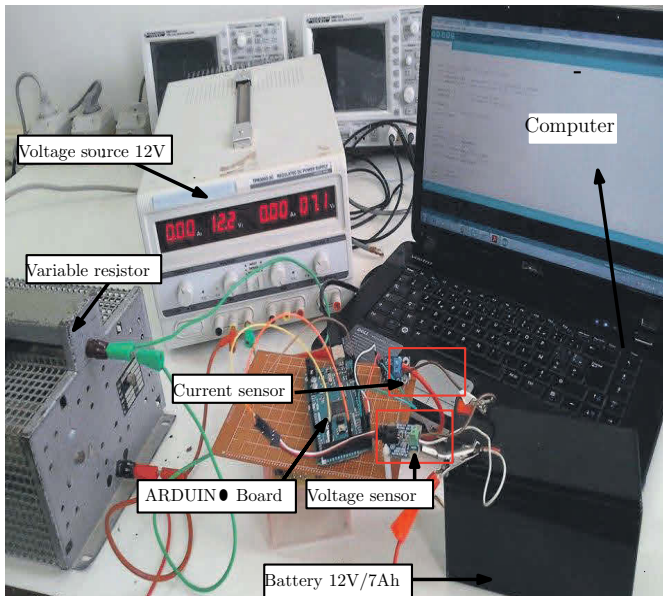**Fig. 7:** Flowchart of the particle swarm optimization

Fig. 8: Experimental test

- The current sensor : allows the measurement of the battery current.
- The voltage sensor : allows the measurement of the voltage on battery terminals.
- The variable resistance: to change the value of the connected load.
- ARDUINO Boards: allows the acquisition of current and voltage data for registration on a computer file.
- Voltage source 12V: to supply the battery during the period of charge.

4 Simulation results

Focus on the analysis of the electric characteristics of the third order model, simulation works has been established. At the first part, model's parameters have been extracted through methods mentioned above, and in the second part, a study work has been realised in order to evaluate the effect of the temperature on the behavior of the developed equivalent electric model.

4.1 Results of parameter identification

The proposed model and algorithms have been tested on the lead acid battery 7 Ah, 12 V. Results are illustrated in Table IV.

Tab. 4: Electrical parameters

Parameters	Values obtained from datasheet	Values obtained from GA	Values obtained from PSO
K_c	0.93	0.9529	0.93
$C_0(AS)$	24164	16775	20182
δ	0.01	0.43	0.0895
ε	0.078	0.8567	0.8938
E_{m0}	2.2833	2.3163	2.3251
K_e	$1.677 10^{-4}$	$2.2730 10^{-4}$	$1.887 10^{-4}$
$R_{10}\ \Omega$	0.0336	0.0964	0.0963
$R_{00}\ \Omega$	0.1471	0.1796	0.14
A_0	0.6273	0.41	0.0198
G_{P0}	10^{-12}	$10e^{-12}$	10^{-12}
A_P	-8.057	0.2528	-8
V_{P0}	0.15	0.7168	0.15
R_θ	10	13.7489	10
C_θ	0.9	0.9129	0.9
R_{20}	$15 10^{-3}$	$15 10^{-3}$	$20 10^{-3}$
A_{22}	2	10	1.8
A_{21}	0.1	0.5706	3
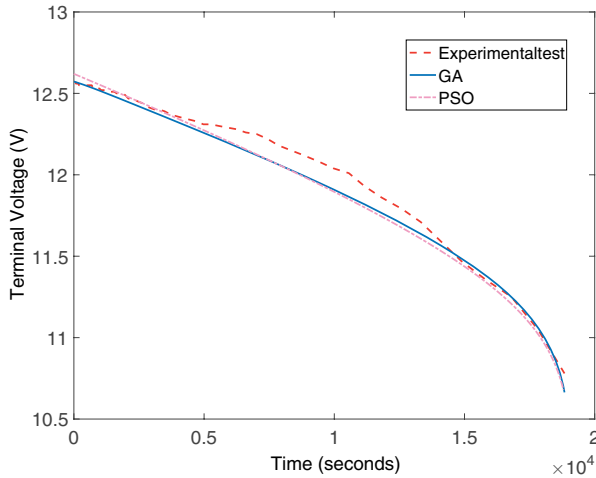
Fig. 9: Terminal voltage of battery: $I = 1.19A$

An acceptable agreement of measured and simulated curves obtained from the genetic algorithm and the particle swarm optimization is shown in Fig. 9. This discharge characteristic of the third order model can be mentioned similar to the battery discharge curve. So, it can be assumed that this proposed model can be used to well modulate the lead acid battery.

According to these results, solving the problem of battery parameter identification can be addressed by GA and PSO. In fact, these meta-heuristic algorithms yield better results than traditional ones (identification using the manufacturer datasheet). They are easy to implement, and they converge quickly to the good results.

The SOC is an important parameter which reflects the battery performances. Therefore, it is necessary to discharge the battery with an adequate current and not for a long period. An accurate use of the battery can not only prevent an over-discharge, and improve the battery life but also allows us to save energy. Fig. 10 shows variations of the state and depth of charge of the battery (considered battery full charged for $t = 0$).

During the discharge of the battery, the state of charge decreases linearly. After discharging the accumulator, the voltage becomes equal to 10.78 V and the SOC approaches to zero. As defined above, the depth of charge depends on the average discharge current, so a high level of current can expire the battery's charge more prematurely. For this reason, DOC is usually less than or equal to SOC.
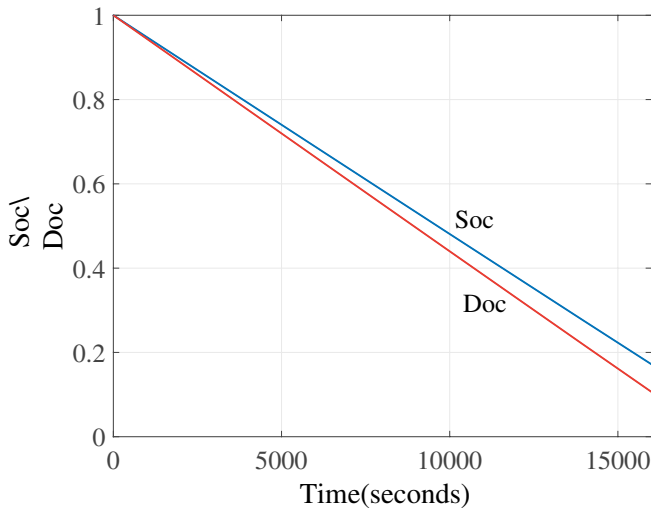
Fig. 10: State of charge SOC and depth of charge DOC during discharge test

4.2 Battery cell characteristics at various temperature

Equations of parameters of the battery cell described above are sensitive to temperature variations. These characteristics described in the datasheet have been established when the battery is put under the standard conditions $25°C$. Otherwise, under other values of the temperature, these characteristics take other gaits.

Figures 11 and 12 draw the influence of the temperature on the discharge and charge voltage of the battery.

The lead acid reaction is sensitive to the temperature. When the lead-acid battery is made at low temperature, its internal resistance increases. This means that voltage is increased under recharging, and it is depressed under discharging in cold cells. The effect of temperature becomes pronounced enough to distinctly change not only the behavior of the basic operating characteristics of the storage system voltage, but also its useful capacity.

Figure 13 presents the effect of the temperature on the discharge capacity.

The temperature has big influences on the speed of the discharge of the battery. In fact, an increase of the temperature is accompanied by a moderate decrease of the capacity of the battery according to the storage time, so a reasonable rise is shown in the used capacity. This is explained by an decrease of the resistivity of the electrolyte and an increase of the diffusion coefficient of the sulfuric acid solution.
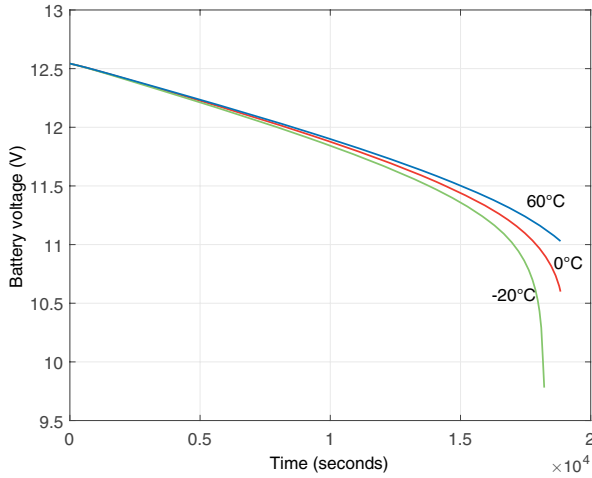
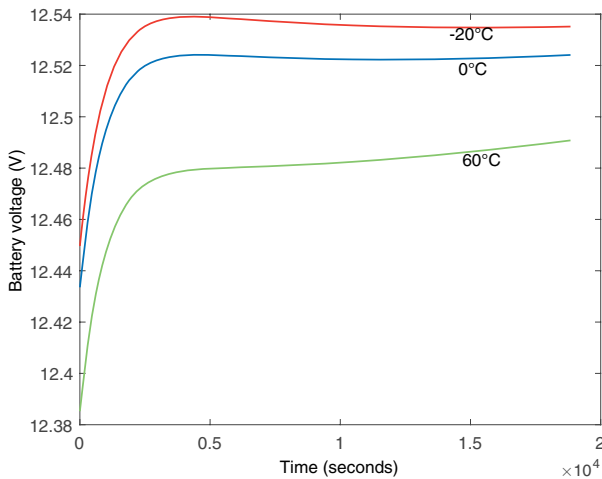**Fig. 11:** Effect of the temperature on the discharge battery voltage ($I = -1.19A$)

Fig. 12: Effect of the temperature on the charge battery voltage ($I = 0.3A$)

5 Conclusion

Taking into account the complexity of the modeling of the behavior of the storage system, we have exploited the third order model. This model allows us to characterize the operation of batteries, using three methods of identification algorithms. The
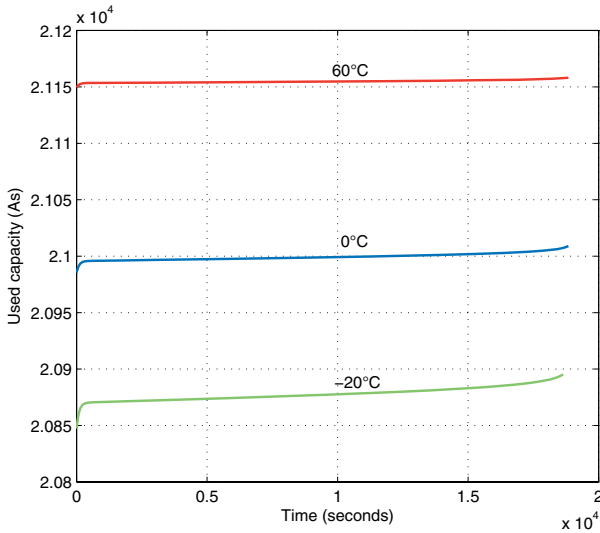
Fig. 13: Influence of the temperature on the used capacity

genetic algorithm and a particle swarm optimization has been implemented in order to search optimal internal parameters of the proposed model. An experimental validation test has been applied on the battery lead acid 12V/7Ah to obtain the discharge characteristic under real conditions. Computing internal parameters, using the manufacturer's datasheet, could imitate the behavior of the real battery. The effectiveness of the proposed equivalent circuit model has been carried out considering in the first part simulation works whose results have been validated by experiments and in the second part simulation works that has been improved with the data calculated through algorithms.

Bibliography

[1] Timothy R. Cook, Dilek K. Dogutan, Steven Y. Reece, Yogesh Surendranath, Thomas S. Teets, and Daniel G. Nocera, Solar Energy Supply and Storage for the Legacy and Nonlegacy Worlds. Chemical Reviews,110 (11), 2010.

[2] H. Chen, T. N. Cong, W. Yang, C. Tan, Y. Li, and Y. Ding, Progress in electrical energy storage system: A critical review, Progress in Natural Science. 19:291-312, 2009.

[3] Olivier Tremblay, Louis.A Dessaint, Experimental validation of a battery Dynamic model for EV applications, ISSN. World electric vehicle journal, 2009.

[4] Olivier Tremblay, Louis.A Dessaint, Abdel-Illah Dekkiche, A generic battery model for the dynamic simulation of hybrid electric vehicles, IEEE. World electric vehicle journal, 2007.

[5] Kandler A. Smitha, Christopher D. Rahnb, Chao-Yang Wangb, Control oriented 1D electrochemical model of lithium ion battery, Energy Conversion and Management. 48 (9), 2007.

[6] Domenico Di Domenico, Anna Stefanopoulou and Giovanni Fiengo, Lithium-Ion Battery State of Charge (SOC) and Critical Surface Charge (CSC) Estimation using an Electrochemical Model-driven Extended Kalman Filter.

[7] Tingshu Hu, Hoeguk Jung, Simple algorithms for determining parameters of circuit models for charging/ discharging batteries, Journal of Power Sources 233, 2013.

[8] Lijun Gao, Shengyi Liu, and Roger A. Dougal, Dynamic Lithium-Ion Battery Model for System Simulation, IEEE Transactions on components and packaging technologies, 25 (3), 2002.

[9] Min Chen, and Gabriel A. Rinćon-Mora, Accurate electrical battery model capable of predicting runtime and $I - V$ performance, IEEE transactions on energy conversion. 21 (2), 2006.

[10] Rami yamin, Ahmed rachid, Modeling and simulation of a lead acid battery packs in matlab simulink, International Conference on Computer Modelling and Simulation, 2014.

[11] Aden Seamana, Thanh-Son Daob, John McPheea, A survey of mathematics-based equivalent-circuit and electrochemical battery models for hybrid and electric vehicle simulation, Journal of Power Sources 256:410–423, 2014.

[12] Massimo Ceraolo, New Dynamical Models of Lead-Acid Batteries, IEEE transactions on power systems,15 (4), 2000.

[13] Nazih Moubayed, Janine Kouta, Ali EI-Ali, Hala Dernayka, and Rachid Outbib, Parameter identification of the lead acid battery model, IEEE, 2008.

[14] Abbas Razzazan, Aliakbar Razzazan, Seyed Mojtaba Shahamiri, Jasem Jafari, Identification, Modeling and Prediction of Stored Energy in Lead-Acid Battery, International Journal of Review in Life Sciences, 2015.

[15] A. Ould Mohamed Yahya, A. Ould Mahmoud, and I. Youm 2, Modeling of an integrated storage system in a hybrid system (PV / Wind / Diesel), Review of Renewable Energies. 10, 2007.

[16] Lalitha Devarakonda, Tingshu Hu, Algebraic method for parameter identification of circuit models for batteries under non zero initial condition, Journal of power sources, 2014.

[17] A.J.Fairweather, M.P.Foster, D.A.Stone, Bttery parameter identification with pseudo random binary sequence excitation, Journal of power sources, 2011.

[18] P.Mauracher, E.Karden, Dynamic modelling of lead acid batteries using impedance spectroscopy for parameter identification, Journal of power sources, 1997.

[19] M.A.Cassaca, Z.M. Salameh,Determination of lead acid battery capacity via mathematical modeling techniques, IEE Trans.Energiy convers 1992.

[20] Bajracharya Q, Dynamic modeling, monitor-ing and control of energy storage system, 2013.

[21] Stefano Barsali and Massimo Ceraolo, Dynamical models of lead acid batteries, implementation issues, Ieee transactions on energy conversion, 2002.

[22] Massimo Ceraolo. New Dynamical Models of Lead Acid batteries: IEEE transactions on energy systems, 2000.

[23] Abbas Razzazan, Aliakbar Razzazan, Seyed Mojtaba Shahamiri, Jasem Jafari, Identification, modeling and prediction of stored Energy in lead-acid battery, 2015.

[24] Robyn A. Jackey, A simple, effective lead-acid battery modeling process for electrical system component selection, 2007.

[25] Nazih Moubayed, Janine Kouta, Ali EI-Ali, Hala Dernayka and Rachid Outbib, parameter identification of the lead acid battery model, 2008.

[26] Guo Sh, The application of genetic algorithms to parameter estimation in Lead−Acid battery equivalent circuit models, 2010.

[27] Johson Browly, clever algoritms:Nature-Inspired Programming Recipes.

Biographies
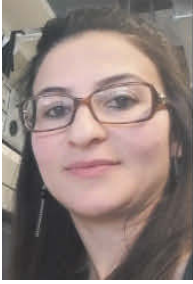
Jihen Loukil received the Electrical Engineering Diploma from the National Engineering School of Sfax (ENIS) in June 2013. Since 2015, she has joined the Control and Energy Management Laboratory (CEMLab). She is in the process of completing her doctoral studies at the ENIS to get the PhD degree in the Electrical System and Renewable Energy (SEER). Currently, she continues her scientific research and experimental works in the Digital Research Center of Sfax. Her current research interests include nonlinear systems, automatic, electronics, networked systems, battery, photovoltaic system etc. She is the author of 2 papers published in international Journals and of 3 papers published in international conferences and books.

Ferdaous Masmoudi received the Electrical Engineering Diploma from the National Engineering School of Sfax (ENIS) in June 2012. Since 2012, she has joined the Control and Energy Management Laboratory (CEMLab). She got her PhD doctoral at the ENIS on 2016. Currently, she is working a Doctor Engineer at the Novel-ti Society, Tunisia.

Nabil Derbel was born in Sfax (Tunisia) in April 1962. He received his Engineering Diploma from the National School of Engineering of Sfax in 1986, the DEA diploma in Automatics from INSA de Toulouse in 1986, the PhD. degree from the Laboratoire LAAS Of Toulouse in 1989, and the Doctorat dÉtat degree from the National School of Engineering of Tunis in 1997. He joined the Tunisian University in 1989, where he held different positions involved in research and education. Currently, he is Professor of Automatic Control at the National School of Engineering of Sfax. His current interests include optimal control, sliding mode control, fuzzy systems, neural networks…

F. Sdiri, Y. Bensalem, H. Trabelsi and M. Abdelkrim

A short circuit fault estimation in PMSM: A comparative study of an adaptive observer and an unknown inputs observer

Abstract: Recently, interest has been increased on model-based approaches for fault detection and particularly focused on observers. The fault detection methods based on observers are considered as successful method. This paper presents a comparative study between two observation techniques applied to field oriented control of permanent magnet synchronous machine (PMSM) under inter turn short circuit. These approaches are used to estimate the PMSM machine state vector and the fault current. The comparative study is done between the adaptive and the unknown inputs observer in order to choose which exhibits the highest performance. Finally, the simulation results are compared to validate the accuracy of analytic method.

Keywords: inter turn short circuit, adaptive observer, unknown inputs observer, fault estimation

Classification: 65C05, 62M20, 93E11, 62F15, 86A22

1 Introduction

The PMSM is actually considered the most used, according to an important role in different applications, the high power and high efficiency [1, 2]. The reliability and safety of PMSM became an interesting domain to avoid a severe damage. The causes of the faults in PMSM can be of various origins such as mechanical vibrations, warming up losses in coppers and cooling problems temperature. About 35% to 40% of the faults in PMSM are related to the insulation of the stator winding and the short circuit fault, as considered the inter turn short circuit is the most occurred faults [3]. This fault spreads quickly and leads to dangerous damage. There is a large volume of published studies describing this fault[4, 5]. The early detection of inter turn short circuit fault is necessary to maintain the operation of the machine [6].

F. Sdiri, Y. Bensalem, H. Trabelsi and M. Abdelkrim: F. Sdiri, University of Gabes, Tunisia, email: fatma.sdiri24@gmail.com , Y. Bensalem, University of Gabes, Tunisia, email: bensalem.yemna@yahoo.fr , H. Trabelsi, University of Sfax, Tunisia, email: Hafedh.trabelsi@enis.rnu.tn, M. Abdelkrim, University of Gabes, Tunisia, email: naceur.abdelkrim@enig.rnu.tn

Different strategies exist in the literature concentrated on the faults detection. These methods can be classified into three main categories; model-less methods, model-based methods and artificial intelligence methods.

Also known as fault detection methods based on signal analysis, the model-less method based on measured machine signals, harmonic or stochastic oscillations. Especially for the vibrations of the machine, the analyzed measurement of the speed, the torque, the position or the currents can be applied in order to make a decision on the health state of the concerned machine. Methods based on signal analysis can be temporal, such as statistic [7], frequency-based methods such as the Fourier transform [8] or methods using a time-frequency approach such as wavelets [9].

In the bibliography, there are also fault detection approaches known by intelligent approaches which are developed in recent years that apply to systems with artificial intelligence. These techniques can combine signal analysis and model-based method to detect and locate a fault. The intelligent method are interested to; expert systems, fuzzy logic, failure trees, neural networks and shape recognition.

Several research works concerning fault detection methods has focused on model-based method. In fact, the parametric method using equations which describe the system. The presence of fault is manifested by a difference between the evolution of the machine parameters in healthy and faulty cases. The identification of the parameters and variables can be done using optimization algorithms, or observers such as the Kalman filter [10].

Much of the current literature on detection methods is increased attentiveness in many applications related to observers approaches. This technique has become a very important area of research [11, 12]. Contrary to the other detection methods, this technique enable to determinate the faults presence and the time of detection, the kind, the fault location, the size, severity and time-variant of the faults. This technique uses the input and output signals to estimate the state and the faults, which is then employed to establish the fault tolerant control loop. It has been developed also to reduce the complexity and the reliability of the electrical structures [13]. Due to their simplicity, many observation methods have been developed in the literature. As presented in [14] and [15] a sliding mode observer of PMSM has been used to estimate the rotor speed and position. A kalman filter has been proposed for stator inter-turn short-circuit detection in permanent magnet synchronous generators [16]. New fault impedance modeling for magnetic characteristics analysis has been used for fault detection in [17]. Also, a high order sliding mode observer has been used to detect the considering fault in [18]. A full adaptive PMSM observer has been applied for fault detection in [19]. The estimation techniques are treated by several research works.

This paper present two observation methods, adaptive observer and unknown inputs observer (UIO)to estimate the fault,the rotor speed and the stator phase currents of the permanent magnet synchronous machine (PMSM). The estimation faults methods of the inter turn short circuits fault of PMSM operating under the Field Oriented Control (FOC). Then, a comparative study between two observers has been performed in order

to discover the most suitable method of detection based on the obtained simulation results. These two observers have been investigated in the healthy condition and under inter turn short circuit fault.

The organization of the paper is as follows. In section II, the mathematical modeling of PMSM in abc frame under field oriented control is given. In Section III, the adaptive observer design is described and the simulation results are illustrated. The UIO design is developed in section IV. Moreover, the simulation results are compared to validate the efficiency observer. Finally, in section V some conclusions are presented.

2 model of faulty PMSM

The equations system of faulty PMSM machine in abc frame is described by:

$$
\begin{bmatrix} V_a \\ V_b \\ V_c \\ 0 \end{bmatrix} = \begin{bmatrix} R_s & 0 & 0 & -R_{a2} \\ 0 & R_s & 0 & 0 \\ 0 & 0 & R_s & 0 \\ -R_{a2} & 0 & 0 & -R_{a2}+R_f \end{bmatrix} \begin{bmatrix} i_a \\ i_b \\ i_c \\ i_f \end{bmatrix}
$$

(1)

$$
+ \begin{bmatrix} L_s & 0 & 0 & -L_{a2}-M_{a1a2} \\ 0 & L_s & 0 & -M_{a2b} \\ 0 & 0 & L_s & -M_{a2c} \\ -L_{a2}+M_{a1a2}-M_{a2b} & 0 & 0 & L_{a2} \end{bmatrix} \times \frac{d}{dt} \begin{bmatrix} i_a \\ i_b \\ i_c \\ i_f \end{bmatrix} + \begin{bmatrix} e_a \\ e_b \\ e_c \\ e_f \end{bmatrix}
$$

with

$$
\begin{bmatrix} e_a \\ e_b \\ e_c \\ e_f \end{bmatrix} = \psi_m \begin{bmatrix} \cos\theta \\ \cos\left(\theta - \frac{2\pi}{3}\right) \\ \cos\left(\theta + \frac{2\pi}{3}\right) \\ \mu\cos\theta \end{bmatrix}
$$

(2)

where (V_a, V_b, V_c), (i_a, i_b, i_c, i_f) and (e_a, e_b, e_c, e_f) are respectively the phase voltages, the stator phase currents and the backemf in the abc frame. i_f is the fault current. R_S and L_s are the stator resistance and the stator inductance respectively. ψ_m is the flux linkage due to the permanent magnets.

R_{a2}, r_f and L_{a2} are respectively the resistance of the faulty windings, the short circuit resistance and the self-inductance of the faulty windings, M_{a2b}, M_{a2c} and M_{a1a2} are respectively the mutual inductances between windings and μ is the fraction of shorted turns.

The electromagnetic torque (T_e) and the mechanical rotation speed of the faulty PMSM (Ω) are described respectively by:

$$
T_e = \frac{e_a i_a + e_b i_b + e_c i_c + e_f i_f}{\Omega}
$$

(3)

$$\frac{d\Omega}{dt} = -\frac{f}{J}\Omega + \frac{1}{J}(T_e - T_l) \tag{4}$$

where T_l is the load torque, f is the friction coefficient and J is the motor inertia. According to equation (1) and (4) the electrical state model of the faulty synchronous motor in the reference frame (a,b,c) can be written by system (5).

$$\begin{cases} \dot{x}(t) = Ax(t) + Bu(t) + Ff(t) \\ y(t) = Cx(t) \end{cases} \tag{5}$$

where the state vector $x(t)$, the output vector $y(t)$, the control vector $u(t)$ and $f(t)$ represents the fault are given by the following equations:

$$x(t) = \begin{bmatrix} i_a(t) \\ i_b(t) \\ i_c(t) \\ \Omega(t) \end{bmatrix}, \quad y(t) = \begin{bmatrix} i_a(t) \\ i_b(t) \\ i_c(t) \\ \Omega(t) \end{bmatrix}, \quad u(t) = \begin{bmatrix} v_a(t) - e_a(t) \\ v_b(t) - e_b(t) \\ v_c(t) - e_c(t) \\ T_e(t) - T_l(t) \end{bmatrix}, \quad f(t) = \begin{bmatrix} i_f(t) \\ \frac{d}{dt}i_f(t) \end{bmatrix}$$

The state matrix A, the input matrix B, the matrix C and the matrix F are given by the following equations:

$$A = \begin{bmatrix} \frac{-R_S}{L_s} & 0 & 0 & 0 \\ 0 & \frac{-R_S}{L_s} & 0 & 0 \\ 0 & 0 & \frac{-R_S}{L_s} & 0 \\ 0 & 0 & 0 & \frac{-f}{J} \end{bmatrix}, \quad B = \begin{bmatrix} \frac{1}{L_s} & 0 & 0 & 0 \\ 0 & \frac{1}{L_s} & 0 & 0 \\ 0 & 0 & \frac{1}{L_s} & 0 \\ 0 & 0 & 0 & \frac{1}{J} \end{bmatrix}$$

$$C = \begin{bmatrix} 1 & 0 & 0 & 0 \\ 0 & 1 & 0 & 0 \\ 0 & 0 & 1 & 0 \\ 0 & 0 & 0 & 1 \end{bmatrix}, \quad F = \begin{bmatrix} \frac{R_{a2}}{L_s} & \frac{L_{a1a2}}{L_s} \\ 0 & \frac{M_{a1b}}{L_s} \\ 0 & \frac{M_{a1c}}{L_s} \\ 0 & 0 \end{bmatrix}$$

3 Adaptive observer applied to PMSM

3.1 Adaptive observer design

The adaptive observer, in the referential (a, b, c), is presented by (6).

$$\begin{cases} \dot{\hat{x}}(t) = A\hat{x}(t) + Bu(t) + Ff(t) - L(\hat{y}(t) - y(t)) \\ \hat{y}(t) = C\hat{x}(t) \end{cases} \tag{6}$$
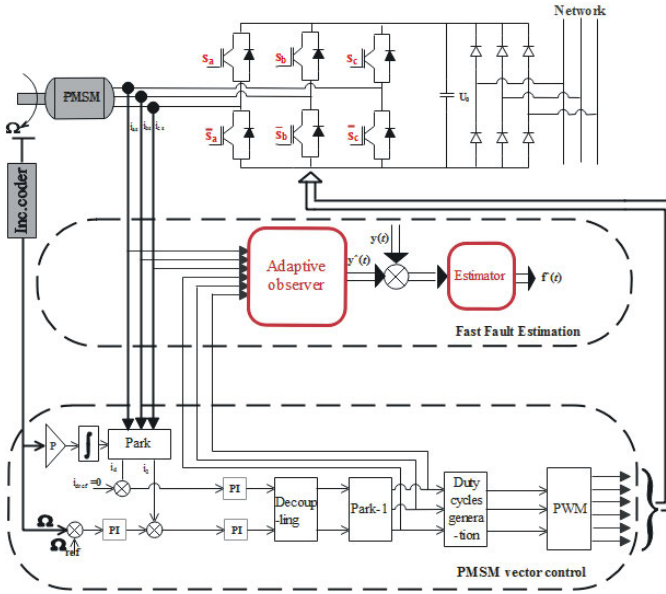
Fig. 1: Architecture of the PMSM vector control with adaptive observer.

Where $\hat{x}(t) \in \mathbb{R}^4$, $\hat{y}(t) \in \mathbb{R}^4$ and $\hat{f}(t) \in \mathbb{R}^2$ are the estimated state vector, the estimated output vector and the estimated fault vector respectively. Since it has been verified that the pair (A,C) is observable, the observer gain matrix L can be chosen in such away that $(A - LC)$ is a stable matrix.

The adaptive observer of the PMSM under field oriented control as shown in Fig. 1.

The existence conditions of this observer are presented in Assumptions 1 and 2.

Assumption 1: rank($f(t)$) = rank(CF).

Assumption 2: The invariant zeros of (A, E, C) belong to open left half plane (LHP).

The error vector $e_x(t)$ of the state $x(t)$, the output $y(t)$ and the fault $f(t)$ are presented as follow.

$$e_x(t) = \hat{x}(t) - x(t) \qquad (7)$$

$$e_y(t) = \hat{y}(t) - y(t) \qquad (8)$$

$$e_f(t) = \hat{f}(t) - f(t) \qquad (9)$$

Then, the state error dynamic $e_x(t)$ is defined as state space by (10).

$$\dot{e}_x(t) = (A + LC)\,e_x(t) + Fe_f(t) \qquad (10)$$

To ensure the observer convergence, it is necessary that the (10) is stable. The Lyapunov function is chosen in the form as follows:

$$V(t) = e_x^T(t) P e_x(t) + \frac{1}{\delta} e_f^T(t) \Phi^{-1} e_f(t). \tag{11}$$

Where P is a positif matrix such as $P^T = P$ and δ is a strictly positive scalar. The symmetric positive matrix $\Phi \in \mathbb{R}^{4 \times 4}$ is the learning rate.

Theorem1: If there exist symmetric positive definite matrices $P, R \in \mathbb{R}^{4 \times 4}$, an observer gain $L \in \mathbb{R}^{4 \times 4}$ and a matrix $S \in \mathbb{R}^{2 \times 4}$ satisfy the following conditions:

$$P(A + LC) + (A + LC)^T P = -R \tag{12}$$

$$F^T P = SC \tag{13}$$

Theorem2: Under Assumptions (1) and (2), given scalars d, l >0, if there exist symmetric positive definite matrices $P \in \mathbb{R}^{4 \times 4}$, $G \in \mathbb{R}^{2 \times 2}$ and $S \in \mathbb{R}^{2 \times 4}$ such that 13 and the following condition are verified.

$$\begin{bmatrix} P(A+LC) + (A+LC)^T P & -\frac{1}{\delta}(A+LC)^T PF \\ * & -2\frac{1}{\delta} F^T PF + \frac{1}{\delta\lambda} G \end{bmatrix} < 0 \tag{14}$$

Then the FFE algorithm is

$$\dot{\hat{f}}(t) = -\Phi S(\dot{e}_y(t) + \delta e_y(t)) \tag{15}$$

Proof: To ensure the observer convergence, it is requested that the derivative of Va must be negative and definite [20]. Thus we have:

$$\dot{V}_a(t) = \dot{e}_x^T(t) P e_x(t) + e_x^T(t) P \dot{e}_x(t) + 2\frac{1}{\delta} e_f^T(t) \Phi^{-1} \dot{e}_f(t). \tag{16}$$

$$\dot{V}_a(t) = e_x{}^T(t)\left((A+LC)^T P + P(A+LC)\right) e_x(t) + 2 e_x^T(t) PF e_f(t)$$
$$-2\frac{1}{\delta} e_f^T(t) \Phi^{-1} \dot{f}(t) - 2\frac{1}{\delta} e_f^T(t) S(\dot{e}_y(t) + \delta e_y(t)). \tag{17}$$

using 13, we obtain:

$$-2\frac{1}{\delta} e_f^T(t) S(\dot{e}_f(t) + \delta e_y(t)) = -2\frac{1}{\delta} e_f^T(t) F^T P(\dot{e}_x(t) + \Phi^{-1} e_x(t)) \tag{18}$$

$$\dot{V}_a = e_x{}^T(t)\left((A+LC)^T P + P(A+LC)\right) e_x(t) - 2\frac{1}{\delta} e_f^T(t) f^T P(A+LC) e_x(t)$$
$$-2\frac{1}{\delta} e_f^T(t) F^T PF e_f(t) - 2\frac{1}{\delta} e_f^T(t) \Phi^{-1} \dot{f}(t) \tag{19}$$

To simplify the (19), we can use lemma 1.

Lemma 1: if G is a positive definite matrix and λ is a strictly positive constant, the following inequality is verified:

$$-2\frac{1}{\delta}e_f^T(t)\,\phi\dot{f}(t) \le \frac{1}{\delta\lambda}e_f^T(t)\,Ge_f(t) + \frac{\lambda}{\delta}\dot{f}^T(t)\,\phi^{-1}G^{-1}\phi^{-1}\dot{f}(t) \tag{20}$$

or we have

$$\left\|\frac{d}{dt}i_f(t)\right\| = \frac{\mu}{\mu(1-\mu)R_a + R_f}U_0 \tag{21}$$

where $f_{\max} = \dfrac{\mu}{\mu(1-\mu)R_a + R_f}U_0$ is a finite value:

$$0 \le f_{\max} < \infty \tag{22}$$

According to lemma, (20) is developed as:

$$-2\frac{1}{\delta}e_f^T(t)\,\phi\dot{f}(t) \le \frac{1}{\delta\lambda}e_f^T(t)\,Ge_f(t) + \frac{\lambda}{\delta}f_{\max}^2\left(\phi^{-1}G^{-1}\phi^{-1}\right) \tag{23}$$

Then, the derivative of V_a satisfies the following condition:

$$\dot{V}_a \le \zeta^T(t)\,\Theta\zeta(t) + \alpha \tag{24}$$

where

$$\alpha = \frac{\lambda}{\delta}f_max^2\left(\phi^{-1}G^{-1}\phi^{-1}\right), \quad \zeta(t) = \begin{bmatrix} e_x(t) \\ e_f(t) \end{bmatrix}$$

$$\Theta = \begin{bmatrix} P(A+LC)+(A+LC)^T P & -\frac{1}{\delta}(A+LC)^T PF \\ \star & -2\frac{1}{\delta}F^T PF + \frac{1}{\delta\lambda}G \end{bmatrix}$$

and $\star$ denotes the symmetric elements in a symmetric matrix.
When $\Theta < 0$ we can obtain $\zeta^T(t)\,\Theta\zeta(t) < -\varepsilon\|\zeta(t)\|^2$, where $\varepsilon = \beta_{\min}(-\Theta)$.
Thus, the observer (6) is stable ($\dot{V}_a < 0$)if it satisfies the inequality.

$$\varepsilon\|\zeta(t)\|^2 > \alpha \tag{25}$$

Which means that the estimation errors of the state and the fault are uniformly bounded, then the adaptive fault estimation

$$\dot{\hat{f}}(t) = -\Phi S\left(\dot{e}_y(t) + \delta e_y(t)\right) \tag{26}$$

Here, we can use the Linear Matrix Inequality (LMI) technique to solve $\Theta < 0$ inequality [21]. The LMI technique is based on the condition of asymptotic stability of the state error based on Lyapunov direct method. But, it is difficult to solve $\Theta < 0$ and 13 simultaneously. Luckily we can transform 13 to the following optimisation [22].

minimise h subject to $\Theta < 0$ and 27

$$
\begin{bmatrix}
\eta I & F^T P - SC \\
\left(F^T P - SC \right)^T & \eta I
\end{bmatrix} > 0
\tag{27}
$$

Then the fault estimation based on adaptive observer algorithm is describe by:

$$
\hat{f}(t) = -\Phi S \left(e_y(t) + \delta \int_{tf}^{t} e_y(\tau) \, d\tau \right)
\tag{28}
$$

3.2 Simulation results

The adaptive observer was applied to PMSM and tested in different stages of speed under field oriented control. The characteristics of the machine is given in Table 2. Simulation tests were performed using Matlab-Simulink software with a Runge-Kutta method (with sampling time 10^{-5} sec).

After starting the PMSM, a load torque $T_l = 5$ N. m at time $t = 0.5$ s is applied. Moreover,the inter turn short circuit occurred at time $t = 1.5$ s.
Figure (2) shows the evolution of the stator phase currents in the (a, b, c) frame. Considering a inter turn short circuit failure occurring at time $t = 1.5$ s, we remark that the magnitude of the stator phase currents in (a, b, c) frame grows significantly with a quite large asymmetry between them. Figure 3.a shows the estimated stator currents using adaptive observer. Figure 3.b shows the current error i_a, so we can observe that the magnitude of this error is around 0.02 A.

The PMSM speed evolution under the field oriented control follow correctly to the reference value as shown in Fig. 4.a. Moreover, we remark at 1. 5 s an increase in the
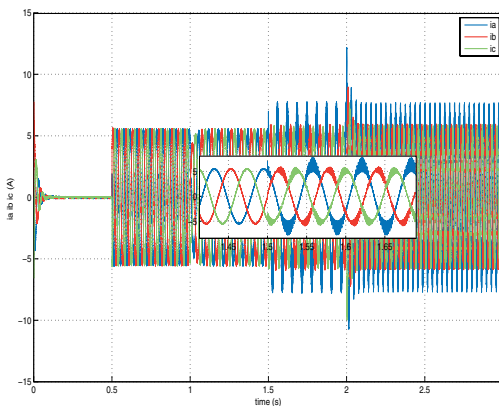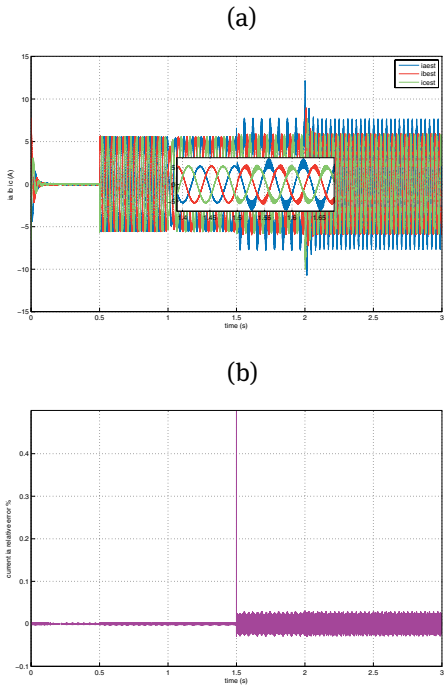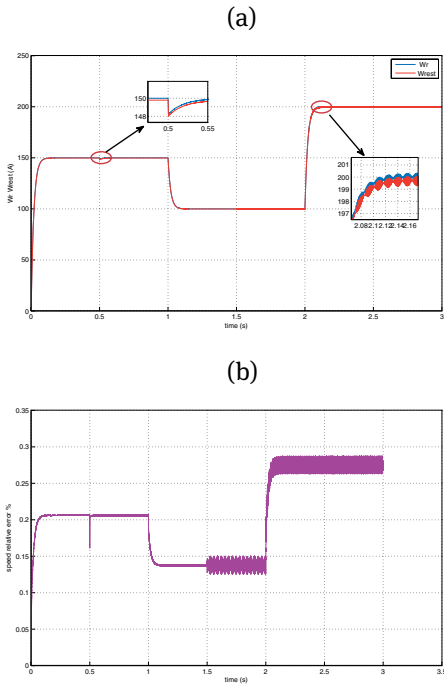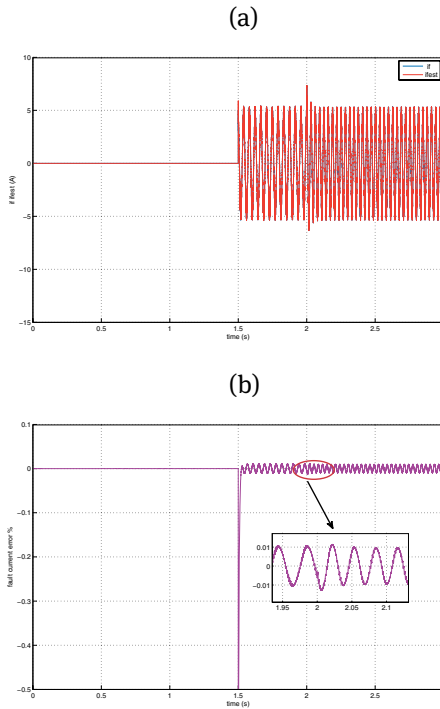

Fig. 2: Simulation results of the stator phase currents in (a, b, c) frame.

(a)

(b)

Fig. 3: Evolution of the current i_a. (a) Evolution of the estimated stator phase currents. (b) Evolution of the current i_a error.

(a)

(b)

Fig. 4: Evolution of the rotor speed w_r. Evolution of the measured and the estimated speed w_r. Evolution of the speed w_r error.

(a)

(b)

Fig. 5: Evolution of the fault current i_f. (a) Evolution of the measured and the estimated fault current i_f. (b) Evolution of the fault current i_f error.

speed magnitude ripple. Therefore, the estimated speed has the same evolution of the measured one. The error speed takes a small value reaches to orders of 0. 2 rd/s as shown in Fig. 4.b.

Figure 5.a shows the evolution of the fault current i_f. This fault is average zero at time $t = 1.5$ s and take then the sinusoidal form after the failure occurs. We note that the fault current i_f is a time-varying fault. We note that the convergence of this observer with a small error between the measured and the estimated fault current around 0.01 A value, as shown in Fig. 5.b.

4 Unknown inputs observer application

4.1 Unknown inputs observer design

The electrical state model of the synchronous motor, can be written with unknown inputs as follows:

$$\begin{cases} \dot{x}(t) = Ax(t) + Bu_d(t) + Ff(t) + Dd(t) \\ y(t) = Cx(t) \end{cases} \tag{29}$$

Where the control vector $u_d(t)$ and the unknown input $d(t)$ are given by the following equations:

$$u_d(t) = \begin{bmatrix} v_a - e_a \\ v_b - e_b \\ v_c - e_c \\ T_e \end{bmatrix}, \quad d(t) = T_l(t)$$

The unknown inputs matrix D is given by the following equation:

$$D = \begin{bmatrix} 0 \\ 0 \\ 0 \\ 1 \\ -\dfrac{1}{J} \end{bmatrix}$$

We note that:

- rank (CD) = rank $(D) = q$
- rank (CF) = rank $(F) = l$
- rank $\begin{bmatrix} sI_n - A & D & F \\ C & 0 & 0 \end{bmatrix}$ = rank (A) + rank (D) + rank (F) $\forall$ s $\in$ $\mathbb{C}$, $\mathbb{R}(s) > 0$

A non singular matrix T is chosen such that rank (T) = rank $(A) = n$.

Where $T = \begin{bmatrix} N & D & F \end{bmatrix}$ with N is an arbitrary matrix. A transformation of the initial system which can be represented in the following equation:

$$\begin{cases} \dot{\bar{x}}(t) = \bar{A}\bar{x}(t) + \bar{B}u_d(t) + \bar{D}d(t) + \bar{F}f(t) \\ \bar{y}(t) = \bar{C}\bar{x}(t) \end{cases} \tag{30}$$

$$\bar{A} = T^{-1}AT = \begin{bmatrix} \bar{A}_{11} & \bar{A}_{12} & \bar{A}_{13} \\ \bar{A}_{21} & \bar{A}_{22} & \bar{A}_{23} \\ \bar{A}_{31} & \bar{A}_{32} & \bar{A}_{33} \end{bmatrix}, \bar{B} = T^{-1}BT = \begin{bmatrix} B_1 \\ B_2 \\ B_3 \end{bmatrix},$$

$$\bar{D} = T^{-1}D = \begin{bmatrix} 0 \\ I_l \\ 0 \end{bmatrix}, \bar{F} = T^{-1}F = \begin{bmatrix} 0 \\ 0 \\ I_q \end{bmatrix}, \bar{C} = CT = \begin{bmatrix} CN & CD & CF \end{bmatrix}.$$

Corresponding to the state vectors $x_2(t)$ and $x_3(t)$, the unknown input $d(t)$ and the fault $f(t)$ are introduced, where $\bar{x}(t) = T^{-1}x(t) = \begin{bmatrix} \bar{x}_1(t) \\ \bar{x}_2(t) \\ \bar{x}_3(t) \end{bmatrix}$ and $\bar{x}_1(t)$ $\in$ $\mathbb{R}^{n-l-q}$, $\bar{x}_2(t)$ $\in$ $\mathbb{R}^l$, $\bar{x}_3(t)$ $\in$ $\mathbb{R}^q$.

So the unknown input and fault free-system is written as follows:

$$\begin{bmatrix} I_{n-l-q} & 0 & 0 \end{bmatrix}\dot{\bar{x}}(t) = \begin{bmatrix} \bar{A}_{11} & \bar{A}_{12} & \bar{A}_{13} \end{bmatrix}\bar{x}(t) + \bar{B}_1 u_d(t) \tag{31}$$

$$y(t) = \begin{bmatrix} CN & CN & CF \end{bmatrix}\bar{x}(t) \tag{32}$$

$\bar{x}_2(t)$ and $\bar{x}_3(t)$ can be obtained from $y(t)$ and $\bar{x}_1(t)$.

We choose the non singular matrix $U = \begin{bmatrix} CD & CF & Q \end{bmatrix}$, $Q \in \mathbb{R}^{p*p-l-q}$ is an arbitrary matrix with $p \geqslant l + q$.

which can be defined:

$$U^{-1} = \begin{bmatrix} U_1 \\ U_2 \\ U_3 \end{bmatrix} \tag{33}$$

$U_1 \in \mathbb{R}^{l*p}$, $U_2 \in \mathbb{R}^{q*p}$, $U_3 \in \mathbb{R}^{(p-l-q)*p}$

We obtain:

$$U^{-1}U = \begin{bmatrix} U_1 \\ U_2 \\ U_3 \end{bmatrix} \begin{bmatrix} CD & CF & Q \end{bmatrix} = \begin{bmatrix} U_1 CD & U_1 CF & U_1 Q \\ U_2 CD & U_2 CF & U_2 Q \\ U_3 CD & U_3 CF & U_3 Q \end{bmatrix}$$
$$= \begin{bmatrix} I_l & 0 & 0 \\ 0 & I_q & 0 \\ 0 & 0 & I_{P-l-q} \end{bmatrix} \tag{34}$$

Equation (32) is multiply by U^{-1} by two sides, taking into account the two relations (33) and (34), the observation equation is given by:

$$U_1 y(t) = U_1 CN\bar{x}_1(t) + \bar{x}_2(t) \tag{35}$$

$$U_2 y(t) = U_2 CN\bar{x}_1(t) + \bar{x}_3(t) \tag{36}$$

$$U_3 y(t) = U_3 CN\bar{x}_1(t) \tag{37}$$

Therefore, the substitution of (35) and (36) in (31), and the combination with (37), gives the following system:

$$\begin{cases} \dot{\bar{x}}_1(t) = \tilde{A}_1 \bar{x}_1(t) + \bar{B}_1 u_d(t) + E_1 y(t) \\ \bar{y}(t) = \tilde{C}_1 \bar{x}_1(t) \end{cases} \tag{38}$$

where

$$E_1 = \bar{A}_{12} U_1 + \bar{A}_{13} U_2$$
$$\tilde{C}_1 = U_3 CN \tag{39}$$
$$\bar{y}(t) = U_3 y(t)$$

An unknown inputs observer may be developed as follows:

$$\dot{w}(t) = \left(\tilde{A}_1 - L\tilde{C}_1\right) w(t) + \bar{B}_1 u_d(t) + L\bar{y} + E_1 y(t)$$
$$= \left(\tilde{A}_1 - L\tilde{C}_1\right) w(t) + \bar{B}_1 u_d(t) + (LU_3 + E_1) y(t) \tag{40}$$

where $w(t) = \hat{x}_1(t)$, $w \in \mathbb{R}^{n-l-q}$.

L is the observer gain to maintain the stability of $\left(\tilde{A}_1 - L\tilde{C}_1\right)$ The existence conditions of this observer is described by:

- The pair $(\tilde{A}_1, \tilde{C}_1)$ observable or detectable
- Rank $\begin{bmatrix} sI_{n-l-q} - \bar{A}_{11} & -\bar{A}_{12} & -\bar{A}_{13} \\ CN & CD & CF \end{bmatrix} = n \, \forall s \in \mathbb{C}, \mathbb{R}(s) \geqslant 0$

The state estimation error dynamics becomes:

$$\dot{e}_{\bar{x}1}(t) = \left(\tilde{A}_1 - L\tilde{C}_1 \right) e_{\bar{x}1}(t) \tag{41}$$

where $e_{\bar{x}1}(t) = w(t) - \bar{x}_1(t)$.

If $\left(\tilde{A}_1 - L\tilde{C}_1 \right)$ is Hurwitz, the estimation error converges exponentially to zero. From (35) and (36), the state of the original system (29) can be estimated as follows:

$$\hat{x}(t) = T\hat{\bar{x}}(t) = T \begin{bmatrix} \hat{\bar{x}}_1(t) \\ \hat{\bar{x}}_2(t) \\ \hat{\bar{x}}_3(t) \end{bmatrix} = T \begin{bmatrix} w(t) \\ U_1 y(t) - U_1 CN w(t) \\ U_2 y(t) - U_2 CN w(t) \end{bmatrix} \tag{42}$$

After an algebraic manipulation of the equations corresponding to the state vector in (30), the reduced order observer (40) and the equation (42), we can obtain an estimate of the unknown input d denoted by $\hat{d}(t) \in \mathbb{R}^l$, such that:

$$\begin{aligned} \hat{d}(t) &= \dot{\hat{\bar{x}}}_2(t) - \begin{bmatrix} \bar{A}_{21} & \bar{A}_{22} & \bar{A}_{23} \end{bmatrix} \hat{\bar{x}}(t) - \bar{B}_2 u_d(t) \\ &= U_1 \dot{y}(t) + G_1 w(t) + G_2 y(t) + G_3 u(t) \end{aligned} \tag{43}$$

where

$$G_1 = U_1 CN \left(LU_3 CN - \bar{A}_{11} + \bar{A}_{12} U_1 CN + \bar{A}_{13} U_2 CN \right) - \bar{A}_{21} + \bar{A}_{22} U_1 CN + \bar{A}_{23} U_2 CN \tag{44}$$

$$G_2 = U_1 CN \left(-LU_3 - \bar{A}_{12} U_1 - \bar{A}_{13} U_2 \right) - \bar{A}_{22} U_1 - \bar{A}_{23} U_2 \tag{45}$$

$$G_3 = -U_1 CN \bar{B}_1 - \bar{B}_2 \tag{46}$$

The estimation error of the unknown input, designated by $e_d(t)$ is:

$$e_d(t) = d(t) - \hat{d}(t) = U_1 CN \dot{e}(t)_{\bar{x}1}(t) + \left(\bar{A}_{12} - \bar{A}_{22} U_1 CN - \bar{A}_{23} U_2 CN \right) e_{\bar{x}1}(t) \tag{47}$$

In the same way, the estimated fault is given by:

$$\begin{aligned} \hat{f}(t) &= \dot{\hat{\bar{x}}}_3(t) - \begin{bmatrix} \bar{A}_{31} & \bar{A}_{32} & \bar{A}_{33} \end{bmatrix} \hat{\bar{x}}(t) - \bar{B}_3 u_d(t) \\ &= U_2 \dot{y}(t) + G_4 w(t) + G_5 y(t) + G_6 u_d(t) \end{aligned} \tag{48}$$

where

$$G_4 = U_2 CN \left(LU_3 CN - \bar{A}_{11} + \bar{A}_{12} U_1 CN + \bar{A}_{13} U_2 CN \right) - \bar{A}_{31} + \bar{A}_{32} U_1 CN + \bar{A}_{33} U_2 CN \tag{49}$$

$$G_5 = U_2 CN \left(-LU_3 - \bar{A}_{12} U_1 - \bar{A}_{13} U_2 \right) - \bar{A}_{32} U_1 - \bar{A}_{33} U_2 \tag{50}$$

$$G_6 = -U_2 CN \bar{B}_1 - \bar{B}_3 \tag{51}$$

The estimation error of the fault $e_f(t)$ is given by:

$$e_f(t) = f(t) - \hat{f}(t) = U_2 C N \dot{e}_{\bar{x}1}(t) + \left(\bar{A}_{31} - \bar{A}_{32} U_1 C N - \bar{A}_{33} U_2 C N\right) e_{\bar{x}1}(t) \quad (52)$$

4.2 Simulation results

The UIO was applied to PMSM machine and tested in different stages of speed under field oriented control. The obtained simulations results are shown in the following figures.

Figure 6.a shows the estimated stator currents using UIO and Fig. 6.b illustrate the current error i_a. We can observe that the magnitude of this error is around 5.10^{-14} A.

(a)

(b)
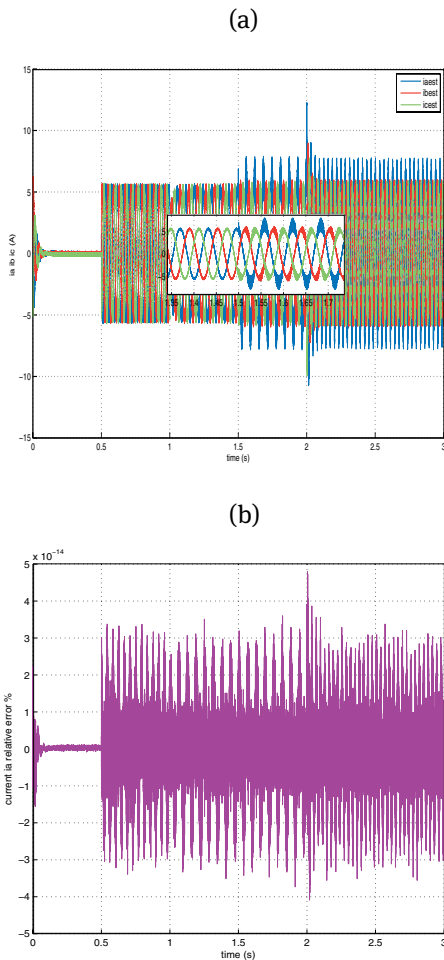
Fig. 6: Evolution of the current i_a. (a) The estimated stator phase currents. (b) Evolution of the current i_a error.

(a)

(b)
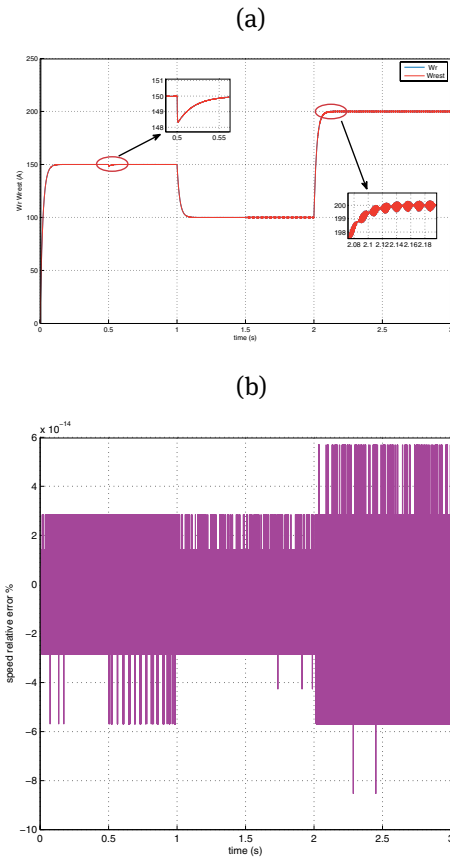
Fig. 7: Evolution of the rotor speed w_r. (a) Evolution of the measured and the estimated speed w_r. (b) Evolution of the speed w_r error.

Compared to adaptive observer, the UIO presents a low level error for stator currents. Therefore, the UIO is more efficient than the adaptive observer.

Based on the Fig. 7.a, we observe that the UIO estimated speed follows correctly the measured speed. Therefore the measured and estimated speed have the same evolution with a similar magnitude. Fig. 7.b shows that the error speed is average around 6.10^{-14} rd/s.

Figure 8.a shows the measured and the estimated fault current i_f. We note that the convergence of this observer with a small phase shifting between the measured and the estimated fault current as shown in 8.b. Figure 9.a shows the measured and the estimated load torque T_l. Therefore the measured and estimated load torque have the same evolution. Moreover, considering inter turn short circuit failure occurring at time $t = 1.5$ s, we note an increase in the load torque magnitude ripple. The error load torque takes a value reaches to 1 N. m as shown in Fig. 9.b.

(a)

(b)
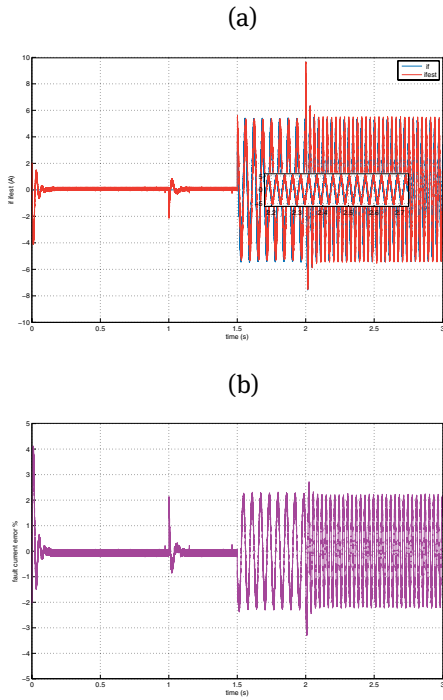
Fig. 8: Evolution of the fault current i_f. (a) Evolution of the measured and the estimated fault current i_f. (b) Evolution of the fault current i_f error.

Tab. 1: Comparison of both observers

	Adaptive Observer	Unknown inputs Observer
Stator currents	+	++
Speed	+	++
Fault current	++	+
Load torque	—	+

Table 1 presents a qualitative comparison between the both observers. For the state estimation; the stator currents and the rotor speed, it can be seen that the unknown inputs observer are more efficient. On the contrary, for the fault estimation, the adaptive observer give a better performance compared to the UIO. We note that the UIO can be estimate the load torque of the machine which represents the unknown input.

(a)

(b)
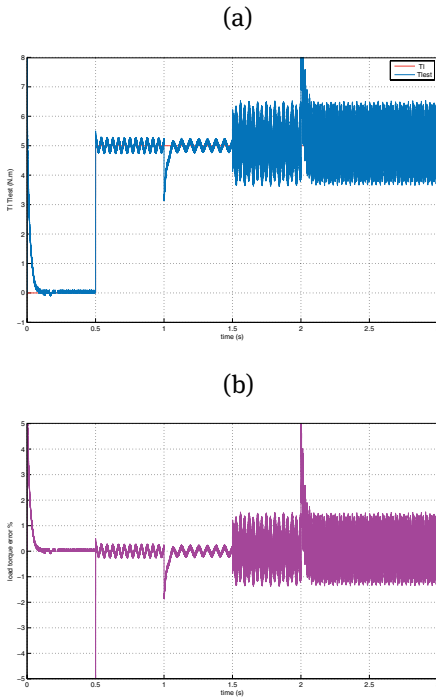
Fig. 9: Evolution of the load torque T_l. (a) Evolution of the measured and the estimated load torque T_l. (b) Evolution of the load torque T_l error.

Tab. 2: Specifications adopted for PMSM

	Parameter values of PMSM
L_s	3. 1 mH
R_s	0. 44 Ω
J	0. 00001 Kg m^2
p	4
F	0. 00001 Kg m^2/s

5 Conclusion

The both observers techniques, adaptive and unknown inputs are presented and applied to a variable speed PMSM. These techniques estimate the stator phase currents, the rotor speed and the inter turn short circuit faults. The first observer is based on LMI approach, although, the principal of the second observer is to make the error estimation independent of the unknown inputs. The comparison between these

observers is presented to validate the efficient one. Simulation results are shown that the high performance is obtained using the unknown inputs observer for the stator phase currents and rotor speed estimation. In contrary, the adaptive observer can estimate an inter turn short circuit fault more rapidly and give a better performance compared to unknown inputs observer.

Acknowledgment

Bibliography

[1] D. Bochao, C. Shumei, W. Guoliang, X. Bingliang *et al.* .A simple diagnosis of winding short-circuited fault of pmsm for electric vehicle. *Vehicle Power and Propulsion Conf. (VPPC)*, :88–91, 2012.

[2] N. Leboeuf, T. Boileau, B. Nahid-Mobarakeh, N. Takorabet, F. Meibody-Tabar, and G. Clerc. Effects of imperfect manufacturing process on electromagnetic performance and online interturn fault detection in PMSMS. *IEEE Trans. on Industrial electronics*, 62(6):3388–3398, 2015.

[3] P. Albrecht, J. Appiarius, R. McCoy, E. Owen, and D. Sharma. Assessment of the reliability of motors in utility applications-updated. *IEEE Trans. on Energy conversion*, (1):39–46, 1986.

[4] J. Yang, Y. Zhao, and X. Ma. An online detection system for inter-turn short circuit faults in dry-type air-core reactor based on labview. *Int. Conf. on Electrical Machines and Systems (ICEMS)*, :1–5, 2011.

[5] M. Zafarani, E. Bostanci, Y. Qi, T. Goktas, and B. Akin. Inter-turn short circuit faults in permanent magnet synchronous machines: An extended review and comprehensive analysis. *IEEE Journal of Emerging and Selected Topics in Power Electronics*, 2018.

[6] M. Y. Kia, M. Khedri, H. R. Najafi, and M. A. S. Nejad. Hybrid modelling of doubly fed induction generators with inter-turn stator fault and its detection method using wavelet analysis. *IET Generation, Transmission & Distribution*, 7(9):982–990, 2013.

[7] J. Hang, S. Ding, J. Zhang, M. Cheng, W. Chen, and Q. Wang. Detection of interturn short-circuit fault for pmsm with simple fault indicator. *IEEE Trans. on Energy Conversion*, 31(4):1697–1699, 2016.

[8] T. Boileau, N. Leboeuf, B. Nahid-Mobarakeh, and F. Meibody-Tabar. Synchronous demodulation of control voltages for stator interturn fault detection in PMSM. *IEEE Trans. on Power Electronics*, 28(12):5647–5654, 2013.

[9] N. H. Obeid, A. Battiston, T. Boileau, and B. Nahid-Mobarakeh. Early intermittent interturn fault detection and localization for a permanent magnet synchronous motor of electrical vehicles using wavelet transform. *IEEE Trans. on Transportation Electrification*, 3(3):694–702, 2017.

[10] M. N. Said, M. E. H. Benbouzid, and A. Benchaib. Detection of broken bars in induction motors using an extended kalman filter for rotor resistance sensorless estimation. *IEEE Trans. on energy conversion*, 15(1):66–70, 2000.

[11] R. T. Meyer, R. A. DeCarlo, S. C. Johnson, and S. Pekarek. Short-circuit fault detection observer design in a pmsm. *IEEE Trans. on Aerospace and Electronic Systems*, 2018.

[12] N. Boumalha, R. Hachelef, D. Kouchih, M. Tadjine, and M. Boucherit. Diagnostic and fault tolerant control by adaptive observer of doubly-fed induction generators with inter-turn rotor and stator fault based wind turbine. 5th *Int. Conf. on Electrical Engineering-Boumerdes (ICEE-B)*, :1–6, 2017.

[13] M. A. Hamida, J. De Leon, and A. Glumineau. Observateur adaptatif interconnecté pour la commande sans capteur de la msapps. 7th *Conf. Int. Francophone d'Automatique*, :6, 2012.

[14] V. C. Ilioudis. A model based sliding mode observer applied in pmsm sensorless control for speed and position. 25th *Mediterranean Conf. on Control and Automation (MED)*, :921–926, 2017.

[15] H. Mehta, V. Joshi, and P. Kurulkar. Implementation issues of sliding mode observer for sensorless field oriented control of pmsm using TMS320F2812. *IEEE Symp. on Sensorless Control for Electrical Drives (SLED)*, :1–6, 2016.

[16] B. Aubert, J. Régnier, S. Caux, and D. Alejo. Kalman-filter-based indicator for online interturn short circuits detection in permanent-magnet synchronous generators. *IEEE Trans. on Industrial Electronics*, 62(3):1921–1930, 2015.

[17] K. -T. Kim, J. Hur, and G. -H. Kang. Inter-turn fault analysis of ipm type BLDC motor using fault impedance modeling. 8th *Int. Conf. on Power Electronics and ECCE Asia (ICPE & ECCE)*, :2216–2224, 2011.

[18] A. Guezmil, H. Berriri, A. Sakly, and M. F. Mimouni. High order sliding mode and an unknown input observers: Comparison with integral sliding mode control for induction machine drive. 7th *Int. Conf. on Modelling, Identification and Control (ICMIC)*, :1–6, 2015.

[19] M. L. Masmoudi, E. Etien, S. Moreau, and A. Sakout. Amplification of single mechanical fault signatures using full adaptive pmsm observer. *IEEE Trans. on Industrial Electronics*, 64(1):615–623, 2017.

[20] K. Zhang, B. Jiang, and V. Cocquempot. Adaptive observer-based fast fault estimation. *Int. Journal of Control, Automation, and Systems*, 6(3):320–326, 2008.

[21] O. Hrizi, B. Boussaid, A. Zouinkhi, and M. N. Abdelkrim. Robust unknown input observer-based fast adaptive fault estimation: Application to mobile robot. *Handbook of Research on Advanced Intelligent Control Engineering and Automation*, IGI Global, :427–456, 2015.

[22] K. Zhang, B. Jiang, and P. Shi, *Observer-based fault estimation and accomodation for dynamic systems*, Springer, vol. 436, 2012.

Biographies

Fatma Sdiri was born in Tatawin, Tunisia. She received the electrical engineering diploma in 2013 from the National Engineering School of Gabes in Tunisia. She is currently Ph. D. student in Electrical Engineering and she is a member of the Modeling, Analysis and Control of Systems (MACS) laboratory. Her current research interests include motor drives and control, diagnosis and fault-tolerant control.

Yemna Bensalem was born in Gabes, Tunisia. She received the B. Sc and M. Sc from the university of Gabes and Sfax, in 2003 and 2005 respectivly. She received the Ph. D. degree from the National school engineering of gabes, Tunisia in 2010. She is currently member in the Modeling, Analysis and Control of Systems (MACS) laboratory. in the university of Gabes. Her interests include design, modeling, control and faults diagnosis of electrical machines.

Hafedh Trabelsi receiced the B. S. degree from Sfax Engineering School(SES), University of Sfax, Tunisia, in 1989, the M. S. degree in the central school of Lyon, France, in 1990, the Ph. D degree from the university of Pris XI Orsay, France in 1994, all in electrical engineering and in 2008, the habilitation degree from the University of Sfax. He is currently a full professor of Electrical Engineering in (SES). He is a member of the research laboratory Computer Embedded system(CES) dealing with smart system and device.

Mohamed Naceur Abdelkrim obtained a Diploma in Technical Sciences in 1980, his Master Degree in Control in 1981 from the ENSET school of Tunis (Tunisia), and his PhD in Control in 1985 and the Doctorate in Sciences Degree (Electrical engineering) in 2003 from the ENIT School of Tunis. Since 2003 he is Professor at the Electrical Engineering Department (Control) of the National Engineering School of Gabes (Tunisia) and he is manager of the Modeling, Analysis and Control Systems (MACS) laboratory.

R. Mars, B. Bouzidi, B. El Badsi and A. Yangui

DCC and DTC of Three-Level Inverter Fed Brushless DC Motor Drives with Torque Ripple Reduction

Abstract: In medium and high power applications, the BLDC motor is associated to multi-level inverters particularly the three levels NPC topology (B12). To improve the torque performance of the B12-inverter fed BLDC motor drives, this paper deals with the synthesis and performance analysis of three control strategies, namely: (i) DCC strategy with current controlled, (ii) DTC_1 strategy, with torque controlled, inspired from the one developed by Takahashi in induction motor drives and (ii) DTC_2 strategy that eliminates the torque dips penalizing DTC_1. Simulation results, carried out considering low and high reference motor speeds, prove the high performance exhibited by the proposed DTC_2 strategy which exhibits a remarkable reduction of the torque ripple and a low distortion in the line currents.

Keywords: Three level NPC inverter, brushless DC motor, direct current control, direct torque control, torque ripple, simulation results.

Classification: 65C05, 62M20, 93E11, 62F15, 86A22

1 Introduction

The brushless DC motor is used in a variety of industry applications due it high efficiency and high power density due to the absence of field winding, in addition the absence of brushes leads to high reliability, low maintenance and high capability [1]. BLDC motor, with a trapezoidal back-electromotive-force (EMF) waveform, has a larger torque and a higher power density than Permanent Magnet Synchronous (PMS) Motor with the sinusoidal back-EMF and the sine wave current [2, 3]. Although these features bring several advantages, the torque ripple is one of the key issues in BLDC motors [4, 5]. Therefore, reducing the torque pulsation is essential to improve the torque performance of the BLDC motor drive system [6–8].

Hence, different control strategies have been successfully implemented in the BLDC motor drives, considering the conventional inverters (two-level three-phase

R. Mars, B. Bouzidi, B. El Badsi and A. Yangui: R. Mars, B. Bouzidi, A. Yangui and B. EL Badsi: R. Mars, email: marsrabiaa@yahoo.com, B. Bouzidi, email: badiibouzidi2010@yahoo.fr, A. Yangui, email: yengui.abderrazak@gmail.com, B. EL Badsi, email: bassemelbedsi@yahoo.fr, University of Sfax, Tunisia

inverters) [9] as well as the unconventional ones (two-level four-switch inverters) [10]. Following a literature review, these strategies are based on the current and torque control approaches [11–13]. Dealing with the most popular control strategies one can distinguish:

– strategy which is based on the direct control of the current (DCC). In [13], hysteresis current controllers are used to drive BLDC motors.
– strategy which is based on the direct control of the torque (DTC). Since its introduction in the middle of the 1980's by Depenbrock and Takahashi, the DTC strategy remains, to date, a state of the art topic which is selected by many research teams worldwide [14, 15]. Recently, different DTC strategies have been successfully implemented in B6 inverter fed BLDC motor drives. In [16], a high performance DTC strategy has been proposed. It considers a vector selection table simply-reduced to the torque control with a two-phase conduction mode during sectors and three-phase conduction mode during sector-to-sector commutations. Although the torque ripple amplitude has been reduced, it has been noticed that this strategy yields unbalanced switching frequencies of the inverter upper and lower IGBTs and a relatively high average value of the common mode voltage of the BLDC motor. In [9], an improved DTC strategy has been proposed to eradicate the above-described strategy limitations.

The conventional two-level inverter is a preferred choice in most industrial low power applications. However, in medium and high power applications, conventional two-level voltage source inverters can be limited by the high distortion in the output voltage (high THD) and the voltage ratings of power switches. For these reasons, the multilevel inverters such as flying-capacitor multilevel inverters, cascaded H-bridge multilevel inverters, and the-point clamped (NPC) multilevel inverters are increasingly being used in high power applications due to their superior performance compared to two-level inverters [17]. Indeed, it offers a lower harmonic distortion of the output currents and operates with reduced $\frac{dv}{dt}$ stress as compared to the two-level inverter driven ac machines [18, 19]. Following a literature review, the flying-capacitor multilevel inverter requires a large number of bulky and expensive capacitors to clamp the voltage. The voltage tracking and pre-charging to the same voltage level of capacitors requires a complex control [20, 21]. In [22], a cascaded H-bridge five-level inverter has been proposed in to suppress torque ripple and harmonics of BLDC motor drive with speed and current closed loop control. This topology needs a galvanic isolation of the dc source for each of the H-bridge. Compared to the cascaded H-bridge and flying-capacitor topologies, the NPC topology operates with a lower number of power semiconductor devices and DC sources.

In this paper three control strategies of BLDC drives fed by three-level NPC inverter (B12) inverter have been proposed for torque ripple suppression, namely: (i) DCC with current controlled , (ii) classical DTC strategy DTC_1, and (iii) a proposed DTC_2 strategy
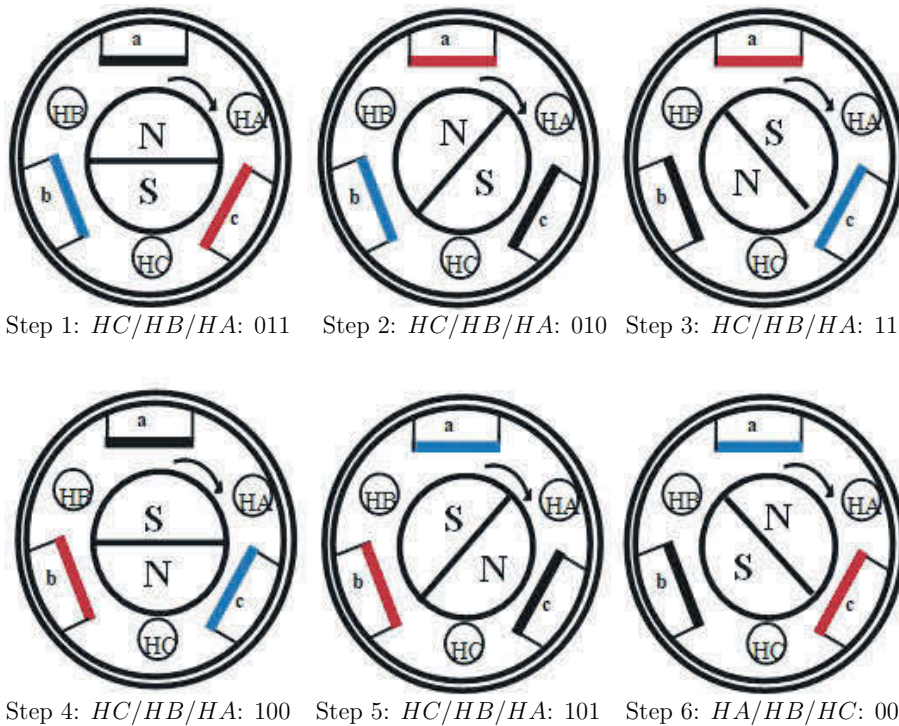
leads to suppress the torque ripple penalizing the DTC1 strategy. A comparative evaluation of the three control strategies performances is presented and commented.

2 Three-Level Inverter Fed BLDC Motor Drive

2.1 Description

The BLDC motor with trapezoidal back-EMFs is suitably fed by 120° rectangular shaped currents, which should be synchronized with the back-EMFs to develop a constant electromagnetic torque with reduced ripple. The BLDC motor is driven according to the six steps of the rotor positions determined by the Hall-effect signals as illustrate in Fig. 1.

Figure 2 illustrates the stator phase currents (i_a, i_b and i_c), the phase back-EMFs (e_a, e_b and e_c), and the corresponding Hall-sensor signals (H_a, H_b and H_c) under the maximum torque operation. The stator voltage equations of the BLDCM are described

Step 1: $HC/HB/HA$: 011   Step 2: $HC/HB/HA$: 010   Step 3: $HC/HB/HA$: 110

Step 4: $HC/HB/HA$: 100   Step 5: $HC/HB/HA$: 101   Step 6: $HA/HB/HC$: 001

Fig. 1: Two-phase excitation method with six steps for driving three-phase BLDC motors.

by:

$$
\left(
\begin{array}{rcl}
v_a &=& R_s i_a + (L_s - M)\dfrac{i_a}{dt} + e_a \\[2mm]
v_b &=& R_s i_b + (L_s - M)\dfrac{i_b}{dt} + e_b \\[2mm]
v_c &=& R_s i_c + (L_s - M)\dfrac{i_c}{dt} + e_c
\end{array}
\right)
\tag{1}
$$

where:

i_a, i_b, i_c: armature phase currents (A),

e_a, e_b, e_c: back-EMFs (V),

Ls: self and mutual inductances (H),

R_s: armature resistance (Ω).

The electromagnetic torque T_{em} produced by the BLDC motor is given as:

$$
T_{em} = \frac{e_a i_a + e_b i_b + e_c i_c}{\Omega}
\tag{2}
$$

where Ω is the rotor angular speed.

The equivalent circuit of the BLDC motor drive including the conventional three-level NPC inverter is shown in Fig. 2. This topology consists of a three-leg inverter
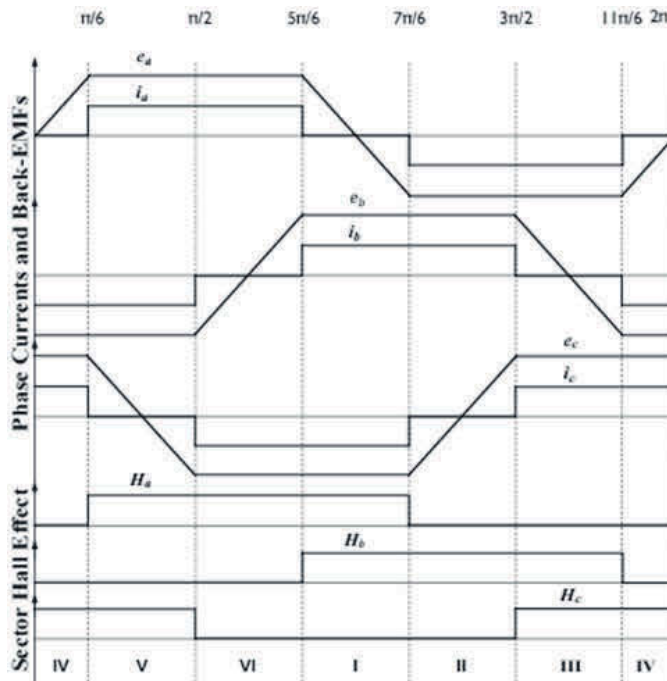
Fig. 2: BLDC motor phase currents and back-EMFs and the corresponding Hall-effect signals under maximum torque operation.
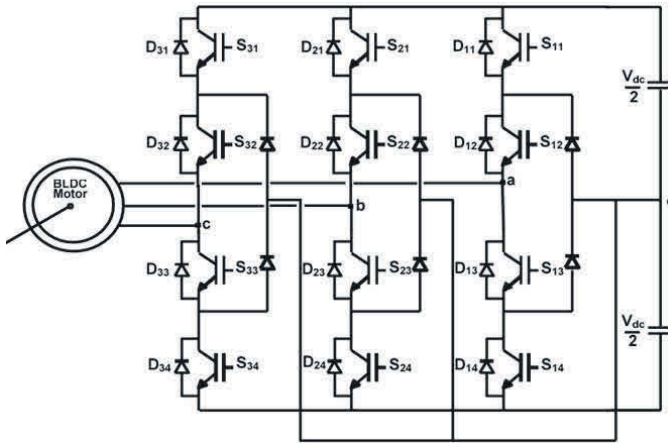
Fig. 3: Connections of the three-level NPC inverter fed BLDC motor drive.

with four power switches per leg rather than two in the case of the conventional two-level three-phase inverter.

2.2 Voltage Vectors Intrinsically-Generated by the Three-Level NPC Inverter

Let us denote the states of the four switches (top to bottom) of a given leg (numbered i=1 to 3) by the binary variables S_{il}, S_{i2}, S_{i3} and S_{i4}, where the binary "1" corresponds to an ON-state and the binary "0" indicates an OFF-state.

Let us call Sk the combination of the states of the power switches of a leg, with: $S_k = [S_{il}, S_{i2}, S_{i3}, S_{i4}]$ and the subscript k is referred to the motor phases that can be "a", "b" or "c".

The corresponding switching combinations are presented in Tab. 1 considering the case of the two-phase conduction mode of the BLDC motor. Hence, the three-level NPC inverter under two-phase conduction mode generates twelve active voltage vectors V_1 to V_{12} as shown in Fig. 4. According to their magnitudes, these vectors are divided into two groups, namely:

- half voltage vectors (V_1 to V_6) have a magnitude equal to $\frac{1}{\sqrt{6}} V_{dc}$,
- intermediate voltage vectors (V_7 to V_{12}) have a magnitude equal to $\frac{1}{\sqrt{2}} V_{dc}$.

Under three-phase conduction mode, the three-level NPC inverter generates twelve active voltage vectors (U_1 to U_{12}) and three null vectors V_{01}, V_{02} and V_{03}, as defined in Tab. 2. According to their magnitudes, the active vectors are divided into two groups, namely:

Tab. 1: The switch state combinations under the two-phase conduction mode of the BLDC motor.

$(S_a\ S_b\ S_c)$	V_α	V_β	$|V_i|$	Vector
Half voltage vectors				
(1100 0000 0000)	$\frac{1}{\sqrt{6}}V_{dc}$	0	$\frac{1}{\sqrt{6}}V_{dc}$	V_1
(0000 0000 0011)	$\frac{1}{\sqrt{24}}V_{dc}$	$\frac{1}{\sqrt{8}}V_{dc}$	$\frac{1}{\sqrt{6}}V_{dc}$	V_2
(0000 1100 0000)	$-\frac{1}{\sqrt{24}}V_{dc}$	$\frac{1}{\sqrt{8}}V_{dc}$	$\frac{1}{\sqrt{6}}V_{dc}$	V_3
(0011 0000 0000)	$\frac{1}{\sqrt{6}}V_{dc}$	0	$\frac{1}{\sqrt{6}}V_{dc}$	V_4
(0000 0000 1100)	$-\frac{1}{\sqrt{24}}V_{dc}$	$-\frac{1}{\sqrt{8}}V_{dc}$	$\frac{1}{\sqrt{6}}V_{dc}$	V_5
(0000 0011 0000)	$\frac{1}{\sqrt{24}}V_{dc}$	$-\frac{1}{\sqrt{8}}V_{dc}$	$\frac{1}{\sqrt{6}}V_{dc}$	V_6
Intermediate voltage vectors				
(1100 0000 0011)	$\sqrt{\frac{3}{8}}V_{dc}$	$\frac{1}{\sqrt{8}}V_{dc}$	$\frac{1}{\sqrt{2}}V_{dc}$	V_7
(0000 1100 0011)	0	$\frac{1}{\sqrt{2}}V_{dc}$	$\frac{1}{\sqrt{2}}V_{dc}$	V_8
(0011 1100 0000)	$-\sqrt{\frac{3}{8}}V_{dc}$	$\frac{1}{\sqrt{8}}V_{dc}$	$\frac{1}{\sqrt{2}}V_{dc}$	V_9
(0011 0000 0011)	$-\sqrt{\frac{3}{8}}V_{dc}$	$-\frac{1}{\sqrt{8}}V_{dc}$	$\frac{1}{\sqrt{2}}V_{dc}$	V_{10}
(0000 0011 1100)	0	$-\frac{1}{\sqrt{2}}V_{dc}$	$\frac{1}{\sqrt{2}}V_{dc}$	V_{11}
(1100 0011 0000)	$\sqrt{\frac{3}{8}}V_{dc}$	$\frac{1}{\sqrt{8}}V_{dc}$	$\frac{1}{\sqrt{2}}V_{dc}$	V_{12}

Tab. 2: The switch state combinations under the two-phase conduction mode of the BLDC motor.

| $(S_a\ S_b\ S_c)$	V_α	V_β	$|U_i|$	Vector
Half voltage vectors				
(1100 0000 0000)	$\frac{1}{\sqrt{6}}V_{dc}$	0	$\frac{1}{\sqrt{6}}V_{dc}$	U_1
(0000 0000 0011)	$\frac{1}{\sqrt{24}}V_{dc}$	$\frac{1}{\sqrt{8}}V_{dc}$	$\frac{1}{\sqrt{6}}V_{dc}$	U_2
(0000 1100 0000)	$-\frac{1}{\sqrt{24}}V_{dc}$	$\frac{1}{\sqrt{8}}V_{dc}$	$\frac{1}{\sqrt{6}}V_{dc}$	U_3
(0011 0000 0000)	$\frac{1}{\sqrt{6}}V_{dc}$	0	$\frac{1}{\sqrt{6}}V_{dc}$	U_4
(0000 0000 1100)	$-\frac{1}{\sqrt{24}}V_{dc}$	$-\frac{1}{\sqrt{8}}V_{dc}$	$\frac{1}{\sqrt{6}}V_{dc}$	U_5
(0000 0011 0000)	$\frac{1}{\sqrt{24}}V_{dc}$	$-\frac{1}{\sqrt{8}}V_{dc}$	$\frac{1}{\sqrt{6}}V_{dc}$	U_6
Intermediate voltage vectors				
(1100 0000 0011)	$\sqrt{\frac{3}{8}}V_{dc}$	$\frac{1}{\sqrt{8}}V_{dc}$	$\frac{1}{\sqrt{2}}V_{dc}$	U_7
(0000 1100 0011)	0	$\frac{1}{\sqrt{2}}V_{dc}$	$\frac{1}{\sqrt{2}}V_{dc}$	U_8
(0011 1100 0000)	$-\sqrt{\frac{3}{8}}V_{dc}$	$\frac{1}{\sqrt{8}}V_{dc}$	$\frac{1}{\sqrt{2}}V_{dc}$	U_9
(0011 0000 0011)	$-\sqrt{\frac{3}{8}}V_{dc}$	$-\frac{1}{\sqrt{8}}V_{dc}$	$\frac{1}{\sqrt{2}}V_{dc}$	U_{10}
(0000 0011 1100)	0	$-\frac{1}{\sqrt{2}}V_{dc}$	$\frac{1}{\sqrt{2}}V_{dc}$	U_{11}
(1100 0011 0000)	$\sqrt{\frac{3}{8}}V_{dc}$	$\frac{1}{\sqrt{8}}V_{dc}$	$\frac{1}{\sqrt{2}}V_{dc}$	U_{12}
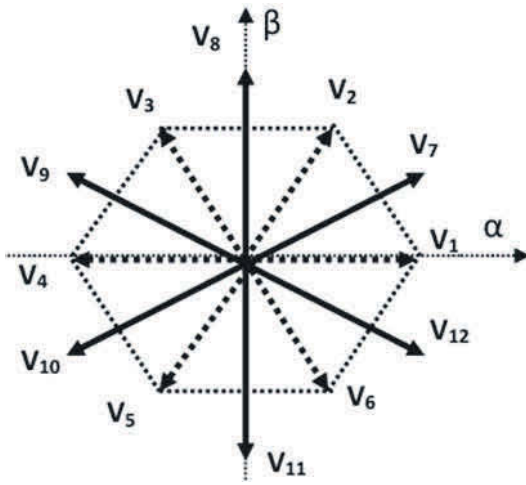
Fig. 4: Space voltage vector in the $\alpha - \beta$ stationary frame of the active voltage vectors generated by the B12-inverter in the two-phase conduction mode.

– intermediate voltage vectors (U_1 to U_6) have a magnitude equal to $\frac{1}{\sqrt{6}} V_{dc}$,
– full voltage vectors (U_7 to U_{12}) have a magnitude equal to $\sqrt{\frac{2}{4}} V_{dc}$.

Figure 5 shows the active voltage vectors, generated by the three-level NPC inverter under the three-phase conduction mode, represented in the stationary $\alpha - \beta$ plane.
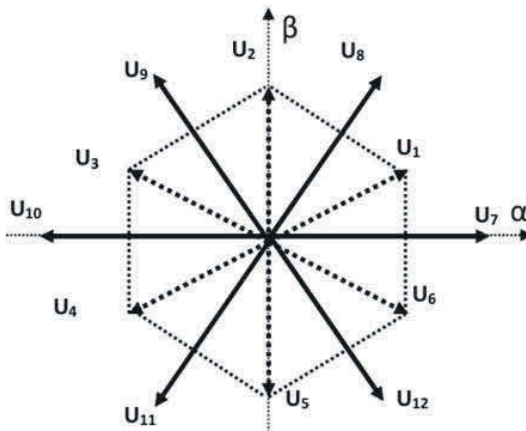

Fig. 5: Space voltage vector in the $\alpha - \beta$ stationary frame of the active voltage vectors generated by the B12-inverter in the three-phase conduction mode.
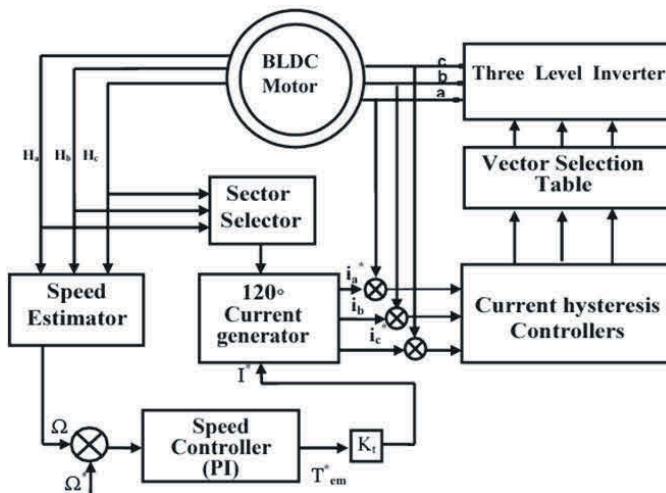
3 Control Strategies

In variable speed applications based on BLDC motor drives, two types of popular control techniques are distinguished: (i) direct current control (DCC), and (ii) direct torque control (DTC). In the following, the control techniques are reviewed, the simulation results of the control performance for each control technique are also recapitulated.

3.1 First Strategy

The first strategy, noted DCC, is based on the direct control of the motor currents through an appropriate selection of the inverter control signals.

Figure 6 shows the block diagram of the DCC strategy dedicated to the control of the BLDC motor drives. This diagram includes:

– **Sector selector:** The sectors are identified through the combinations of the three Hall-effects signals (Ha, Hb and Hc) as illustrated in Fig. 1 and Fig. 2.
– **Speed estimator:** To improve the drive cost-effectiveness, the speed estimation is carried out according to the Hall-effect signals which eliminates the encoder by using the zero-order estimation algorithm discussed in [23].
– **Speed controller (PI):** The output of the Speed controller (PI), determine the reference torque.

Fig. 6: Block diagram of the direct current control strategy implemented in the three level inverter fed BLDCM drives.

- **The torque constant** K_t**:** This constant determine the current amplitude. The DCC strategy is achieved by setting an autopilot angle ? equal to zero. In this case, the expression of the electromagnetic torque can be expressed as:

$$T_{em}(\psi = 0) = 3P\phi_{eff}I_{eff} \tag{3}$$

where:

ϕ_{eff}: The rms value of the flux

I_{eff}: The fundamental of the armature current.

Mainly provided by the BLDC motor, the flux remains almost constant. Consequently, the expression of the electromagnetic torque is reduced to:

$$T_{em}(\psi = 0) = K_t I_{eff} \tag{4}$$

- **120° Current generator:** The current generator is used to generate the reference currents $i_a^\star$, $i_b^\star$ and $i_c^\star$.
- **Current hysteresis:** The DCC strategy is based on the use of hysteresis current controllers. The outputs of these controllers are used to control the IGBTS.

3.2 Second Strategy

The second strategy, noted DTC_1, allows a direct control of the BLDC motor electromagnetic torque through an appropriate selection of the inverter control signals, in order to fulfill the requirements as whether the electromagnetic torque needs to be increased or decreased. This strategy was inspired from the conventional one introduced by Takahashi.

Figure 7 shows the block diagram of the DTC1 strategy dedicated to the control of three level inverter fed BLDC motor drives.

The vector selection table of the DTC_1 strategy, is summarized in Tab. 3. For the case of sector I, DTC_1 strategy considers the following control laws:

- the application of the active voltage vector V_8, achieves the control combination $(c_\tau = +1)$,
- to achieve the control combination $(c_\tau = -1)$, the conventional DTC_1 strategy applies the vector V_{11}.

The vector selection table generates the sequence (0000 0011 1100) to reduce the torque ($c_\tau = -1$). This vector is characterized by a regenerative sequence as shown in Fig. 8. The two currents ib and ic are forced to flow through the diodes D_{23}, D_{24}, D_{31} and D_{32} and the supply source V_{dc} which generates the fairly fast variations of $\left|\frac{di_b}{dt}/\right|$ and $\left|\frac{di_c}{dt}/\right|$ during this regenerative phase.

As a conclusion, the major drawback of the DTC1 strategy is due to the systematic application of active voltage vectors to maintain the electromagnetic torque ($c_\tau =$
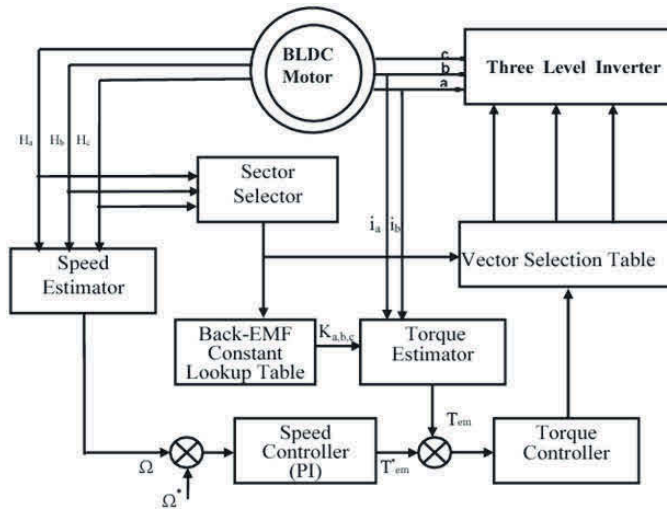
Fig. 7: DTC scheme of three level inverter fed BLDC motor drives.

**Tab. 3:** Vector selection table corresponding to the DTC1 strategy.

	Sectors					
c_τ	I	II	III	IV	V	VI
+1	V_8	V_9	V_{10}	V_{11}	V_{12}	V_7
−1	V_{11}	V_{12}	V_7	V_8	V_9	V_{10}

−1). The application of these voltage vectors affects the electromagnetic torque. This latter undergoes rather rapid drops which lead on the one hand, to a high switching frequency of the IGBTs, and on the other hand, to an important torque amplitude ripple due to the exceeding of the torque hysteresis band during the falls of this latter.

3.3 Third Strategy

The third strategy, noted DTC_2, is based on the subdivision of the ?-? stationary frame into six sectors. Such a subdivision is similar to the one adopted in the DTC1 strategy dedicated to the control of three level inverter fed BLDC motor drives.

The DTC_2 is proposed to minimize the torque ripple penalizing the DTC_1 strategy. The implementation scheme of this strategy is similar to the one adopted in the DTC_1 strategy. The control rules embedded in the vector selection table is the only difference between the control schemes of the proposed DTC1 and DTC_2 strategies. The synthesis of the vector selection table considers the following control laws:
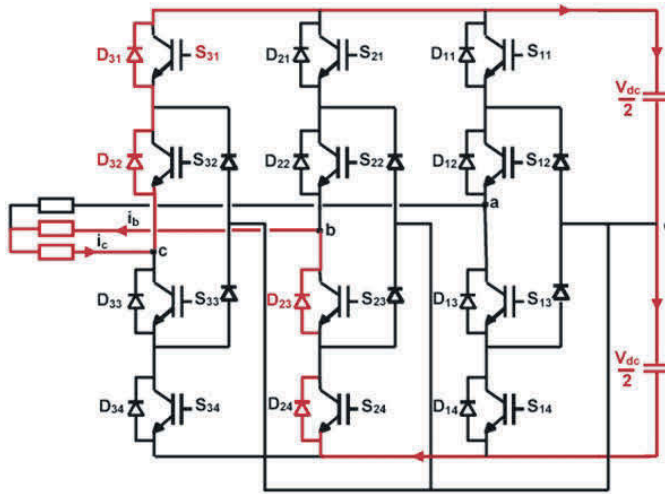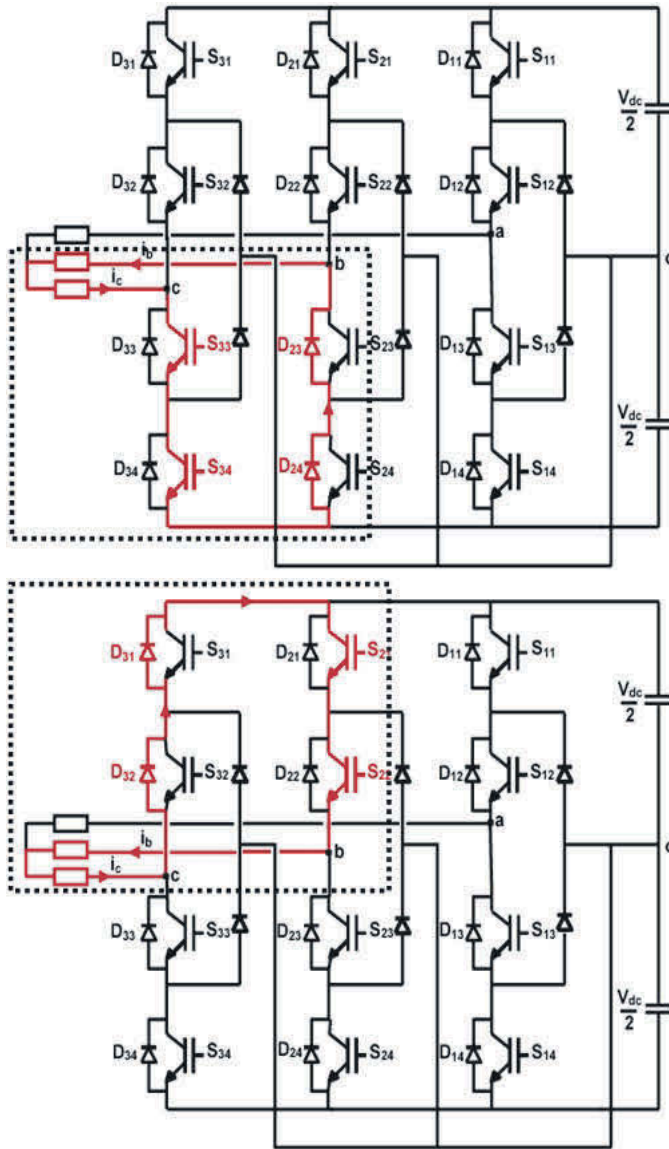
Fig. 8: Current transition during sector I under the conventional DTC1 strategy considering the case of a torque decrease ($c_\tau = -1$).

- for the six sectors, the DTC_2 strategy applies the same active voltage vectors considered in DTC_1 to achieve the control combination ($c_\tau = +1$) corresponding to the increase of the electromagnetic torque
- the application of the voltage vectors V_i ($i = 1$ to 6) achieves the control combination ($c_\tau = -1$), making a difference with DTC1 that considers the voltage vector V_i ($i = 7$ to 12). To obtain balanced switching frequencies of the upper and lower IGBTs, these vectors are characterized by freewheeling sequences involving the upper (IGBT and diode) for a given sector and the lower (IGBT and diode) in the next sector. The above-adopted reasoning has been considered in the six sectors.

Dealing with sector I, the decrease of the torque, in the case of the counterclockwise rotation, is achieved by the active voltage vector V_7. As illustrated in Fig. 9.a , this vector is characterized by a freewheeling sequence involving the lower (S_{33} and S_{34}) IGBTs and (D_{23} and D_{24}) diodes making a difference with the DTC_1 strategy that considers the voltage vector V_5 witch characterized by a regenerative phase. This condition can be also achieved by the application of an active voltage vectors characterized by a freewheeling sequence involving the upper (S_{21} and S_{22}) IGBTs and (D_{31} and D_{32}) diodes as illustrated in Fig. 9.b. The resulting vector selection table is provided in Tab. 5. Although the two approaches are different, it has been found that they lead to the same performance.

The application of the intermediate voltage vector V_i ($i = 7$ to 12) is characterized by a decrease of the torque with a slope that has an absolute value lower than the one observed under the application of the half voltage vector V_i ($i = 1$ to 6). Consequently,

Fig. 9: Current transition during sector I under the DTC$_2$ strategy. Legend (a): torque decrease ($c_\tau = -1$) (first approach) and (b): torque decrease ($c_\tau = -1$) (second approach).

the DTC$_2$ strategy leads to minimize the torque ripple during sequence operation by the application of appropriate half voltage vectors instead of intermediate active voltage vectors. It exhibits lower switching losses than the ones yielded by the conventional DTC$_1$ strategy.

Tab. 4: First vector selection table of the proposed DTC$_2$ strategy in the case of anticlockwise rotation.

	Sectors					
c_τ	I	II	III	IV	V	VI
+1	V_8	V_9	V_{10}	V_{11}	V_{12}	V_7
−1	V_2	V_3	V_4	V_5	V_6	V_1
Clamped	K_{33}	K_{21}	K_{13}	K_{31}	K_{23}	K_{11}
Signal	& K_{34}	& K_{22}	& K_{14}	& K_{32}	& K_{24}	& K_{24}

Tab. 5: Second vector selection table of the proposed DTC$_2$ strategy in the case of anticlockwise rotation.

	Sectors					
c_τ	I	II	III	IV	V	VI
+1	V_8	V_9	V_{10}	V_{11}	V_{12}	V_7
−1	V_3	V_4	V_5	V_6	V_1	V_2
Clamped	K_{21}	K_{13}	K_{31}	K_{23}	K_{11}	K_{33}
Signal	& K_{22}	& K_{14}	& K_{32}	& K_{24}	& K_{24}	& K_{34}

# 4 Simulation-Based Investigation of the proposed strategies Performance

This paragraph is aimed at simulation-based investigation of the proposed strategies performance. The ratings and parameters of the BLDC motor, used in the simulation works, are provided in Tab. 6. The sampling period T_s is equal to 55μs. For the sake of comparison, the same PI controller parameters have been adopted in both strategies. The Proportional-Integral controller of the speed loop is defined by a proportional gain $K_p = 1$ and an integral gain $K_i = 0.5$. The hysteresis bounds of the stator currents are equal to ±0.001A. For both implemented DTC strategies DTC$_1$ and DTC$_2$, the hysteresis controllers of the electromagnetic torque are two-level comparators. The hysteresis bounds of the torque are equal to ±0.001Nm.

Tab. 6: BLDC motor parameters

DC-link voltage	24	p	3
Rated torque	2.5 Nm	R_s	0.2 Ω
Rated speed	2500 rpm	L_s	0.3 mH
J	4.1 gm^2	f	0.5 mN.m.s
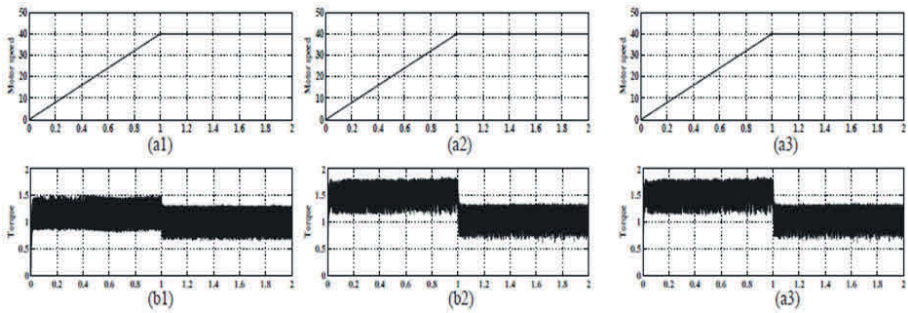
Fig. 10: Simulated steady-state variables yielded by the direct current control strategy (subscript 1), the DTC$_1$ strategy (subscript 2) and the proposed DTC$_2$ one for a speed Ω = +40rad/s considering the case of an anticlockwise rotation. (a): motor speed (b): electromagnetic torque.
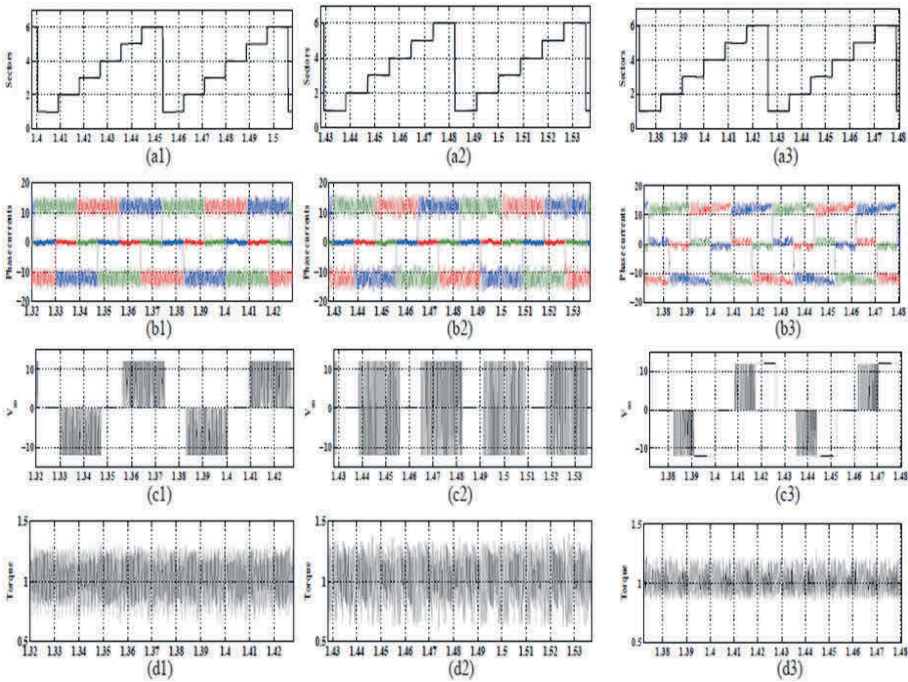
Fig. 11: Simulated steady-state variables yielded by the direct current control strategy (subscript 1), the DTC$_1$ strategy (subscript 2) and the proposed DTC$_2$ one for a speed Ω = + 40rad/s considering the case of an anticlockwise rotation. (a): sector succession, (b): phase currents, (c): phase voltage V_{ao}, (d): electromagnetic torque.

The obtained simulation results at steady state operation of the BLDCM drive corresponding to the case of a high reference speed of +120rad/s are illustrated in Fig. 12 and Fig. 13.
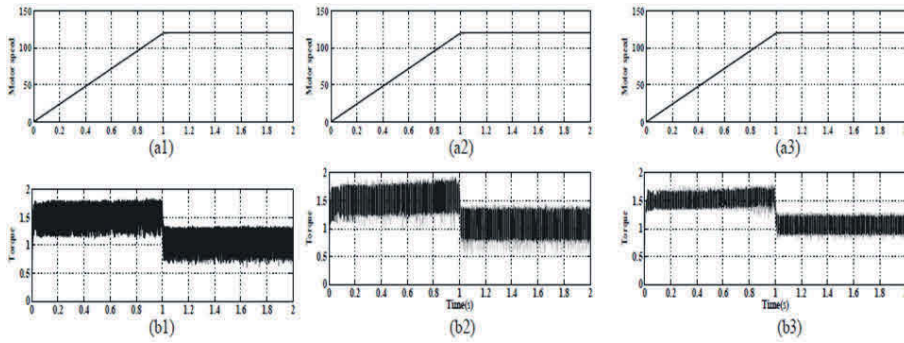
Fig. 12: Simulated steady-state variables yielded by the direct current control strategy (subscript 1), the DTC$_1$ strategy (subscript 2) and the proposed DTC$_2$ one for a speed $\Omega = + 120\,rad/s$ considering the case of an anticlockwise rotation. (a): motor speed (b): electromagnetic torque.
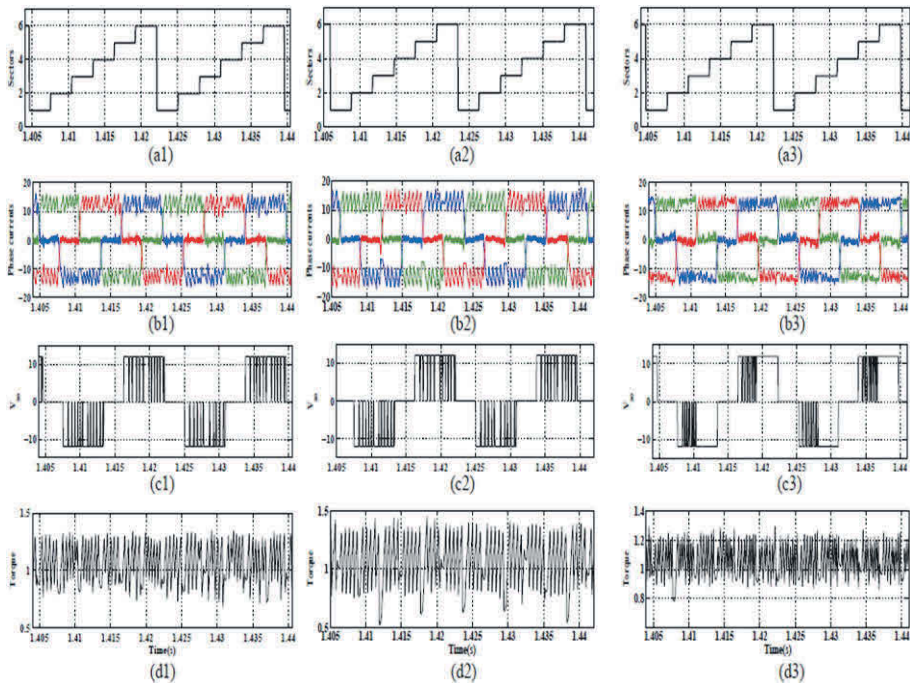

Fig. 13: Simulated steady-state variables yielded by the direct current control strategy (subscript 1), the DTC$_1$ strategy (subscript 2) and the proposed DTC$_2$ one for a speed $\Omega = + 120\,rad/s$ considering the case of an anticlockwise rotation. (a): sector succession, (b): phase currents, (c): phase voltage V_{ao}, (d): electromagnetic torque.

Figure 12 shows the waveforms of the motor speed, the electromagnetic torque. From the analysis of Figs. 12.a1, 12.a2 and 12.a3, one can notice that both strategies exhibit a high dynamic of the motor speed.

Figures 13.b1, 13.b2 and 13b3 give the stator phase currents iabc which are rectangular with a phase shift of 120°. The comparison of these figures shows that the stator current waveforms present a lower harmonic distortion, in the case of the DTC2 strategy.

Figures 13.c1, 13.c2 and 13.c3 illustrate the V_{ao} waveforms yielded by both control strategies. Referring to these Figures, it can be noted that Vao is characterized by an alternative waveform with an average value not-exceeding 1.25% of the DC-bus voltage. This is due to the balanced switching frequencies of the upper and the lower IGBTs yielded by both developed strategies.

Figures 13.d1, 13.d2 and 13.d3 give the electromagnetic torque waveform at steady-state. Referring to Fig. 13.d1, it is clearly noted that the proposed DCC strategy leads to an important torque amplitude ripple. Figure 13.d3 clearly confirms the lower torque ripple exhibited by DTC_2 due to the application of the half active voltage vectors Vi such benefit is missed in the case of the conventional DTC1 strategy due to the application of intermediate active voltage vectors Vi to maintain the electromagnetic torque ($c_\tau = -1$).

In what follows, the effectiveness of both strategies under a reference mechanical speed Ω = 40rad/s is presented in Figures 10 and 11 considering a steady-state operation characterized by a same load torque T_l = 1Nm. Referring to these Figures, one can clearly confirm that the proposed DTC_2 strategy leads to a low distortion in the line currents. It exhibits a lower torque ripple for both reference speeds compared to the ones offered by the DCC and the DTC_1 strategies.

5 Conclusions

As the BLDC motor is integrated in many industrial variable speed applications covering a wide range of power, it is associated to two-level inverter, while in medium and high power applications it is associated to multi-level inverters, particularly the three-level NPC topology. In this paper, a comparative study between three control strategies has been treated. The considered strategies are described as follows: (i) DCC which is based on the direct current control, (ii) DTC_1 which is inspired from the one implemented in induction motor drives, and (iii) DTC_2 which has been proposed to eradicate the torque ripples penalizing the DTC_1 strategy. Simulation results, carried out considering low and high reference motor speeds, leads the high performance exhibited by the proposed DTC_2 strategy. This strategy is motivated by many performances such as: lower switching losses, low distortion in the line currents and remarkable reduction of the torque ripple.

Bibliography

[1] X. Huang, A. Goodman, C. Gerada, Y. Fang, and Q. Lu. A single sided matrix converter drive for a brushless DC motor in aerospace applications. IEEE Trans. Industrial Electronics, 59(9):3542–3552, 2012.

[2] G. Buja, M. Bertoluzzo, and R. K. Keshri. Torque ripple-free operation of PM BLDC drives with petal-wave current supply. IEEE Trans. Industrial Electronics, 62(7):4034–4043, 2015.

[3] Chan, C. C., Jiang, J. Z., Xia, W., Chan, K. T. Novel wide range speed control of permanent magnet brushless motor drives. IEEE transactions on power electronics, 10(5), 539-546,1995

[4] T. Shi, Y. Guo, P. Song, and C. Xia. A new approach of minimizing commutation torque ripple for brushless DC motor based on DCDC converter. IEEE Trans. Industrial Electronics, 57(10):3483–3490, 2010.

[5] X. Li, C. Xia, Y. Cao, W. Chen, and T. Shi. Commutation torque ripple reduction strategy of Z-source inverter fed brushless DC motor. IEEE Trans. Power Electronics, 31(11):7677–7690, 2016.

[6] C. Xia, Y. Xiao, W. Chen, and T. Shi. Torque ripple reduction in brushless DC drives based on reference current optimization using integral variable structure control. IEEE Trans. Industrial Electronics, 61(2):738–752, 2014.

[7] J. Fang, H. Li, and B. Han. Torque ripple reduction in BLDC torque motor with non-ideal back EMF. IEEE Trans. Power Electronics, 27(11):4630–4637, 2012.

[8] W. Jiang, Y. Liao, J. Wang, P. Wang, and Y. Xie. Improved control of BLDCM considering commutation torque ripple and commutation time in full speed range. IEEE Trans. Power Electronics, 33(5):4249–4260, 2018.

[9] M. Masmoudi, B. El Badsi and A. Masmoudi. Direct Torque Control of Brushless DC Motor Drives with Improved Reliability. IEEE Trans. Power Electronics, 29(9):4855–4865, 2014.

[10] M. Masmoudi, B. El Badsi and A. Masmoudi. DTC of B4-Inverter-Fed BLDC Motor Drives With Reduced Torque Ripple During Sector-to-Sector Commutations. IEEE Trans. Power Electronics, 29(9):4855–4865, 2014.

[11] F. Aghili. Fault-tolerant torque control of BLDC motors. IEEE Trans. Power Electronics, 26(2):355–363, 2011.

[12] C. S. Joice, S. R. Paranjothi and V. J. S. Kumar. Digital control strategy for four quadrant operation of three phase BLDC motor with load variations. IEEE Trans. Industry Applications, 9(2):974–982, 2013.

[13] P. J. Sung, W. P. Han, L. H. Man and F. Harashima. A New Approach for Minimum-Torque-Ripple Maximum-Effeciency Control of BLDC Motor. IEEE Trans. Industrial Electronics, 47(1):109–114, 2000.

[14] I. Takahashi and T. Noguchi. A new quick-response and high efficiency control strategy of an induction motor. IEEE Trans. Industry Applications, 22(5):820–827, 1986.

[15] S. B. Ozturk and H. A. Toliyat. Direct Torque and Indirect Flux Control of Brushless DC Motor. IEEE Trans. Mechatronics, 16(2):351–360, 2011.

[16] Z. Q. Zhu and J. H. Leong. Analysis and Mitigation of Torsional Vibration of PM Brushless AC/DC Drives with Direct Torque Controller. IEEE Trans. Industry Applications, 48(4):1296–1306, 2012.

[17] J. Rodriguez, J.-S. Lai and F. Z. Peng. Multilevel inverters: A survey of topologies controls and applications. IEEE Trans. Ind. Electron., 49(4):724–738, 2002.

[18] J. P. Lyons, V. Vlatkovic, P. M. Espelange, A. A. M. Esser, and F. F. Want. Five level high power motor drive converter and control system, U.S. Patent 6 058 031, May 2, 2000.

[19] S. Bernet, T. Bruckner and P. Stiemer. Three-point converter and method for its operation, U.S. Patent 6 219 265, April 17, 2001.

[20] Y. Liu, A. Q. Huang, W. Song, S. Bhattacharya and G. Tan. Small signal model-based control strategy for balancing individual dc capacitor voltages in cascade multilevel inverter-based statcom. IEEE Trans. Industrial Electronics, 56(6):2259–2269, 2009

[21] H. Vahedi, K. Al-Haddad, P.-A. Labbe and S. Rahmani. Cascaded multilevel inverter with multicarrier pwm technique and voltage balancing feature. IEEE 23rd Int. Symp. on. Industrial Electronics (ISIE) :2155–2160, 2014.

[22] M. A. Doss, E. Premkumar, G. R. Kumar and J. Hussain. Harmonics and torque ripple reduction of Brushless DC Motor (BLDCM) using cascaded H-bridge multilevel inverter. IEEE ICPEC, :296–299, February 2013.

[23] F. G. Capponi, G. D. Donato, L. D. Ferraro, O. Honorati, M. C. Harke and R. D. Lorenz. AC Brushless Drive with Low-Resolution Hall-Effect Sensors for Surface-Mounted PM Machines. IEEE Trans. Industry Applications, 42(2):526–535, 2006.

Biographies

Rabiaa Mars received the B.S degree in 2014 in Electrical Engineering, from the Sfax Engineering National School (SENS), University of Sfax, Tunisia. She is currently working toward the PhD degree in Electrical Engineering. Her main research interests include the synthesis and the implementation of control strategies in BLDC motor drives applied to automotive actuators. She is a member of the Research Laboratory on Renewable Energies and Electric Vehicles (RELEV) of the University of Sfax.

Badii Bouzidi received the B.S. degree in 2005 in Electromechanical Engineering, the M.S. degree in 2006, and the PhD degree in 2011, all in Electrical Engineering, from the Sfax Engineering National (SENS), University of Sfax, Tunisia. His research interests include power electronics and drives, and the implementation of advanced control strategies in AC motor drives applied to automotive systems. He is a member of the Research Laboratory on Renewable Energies and Electric Vehicles (RELEV) of the University of Sfax.

Bassem El Badsi received the B.S. degree in 2004 in Electromechanical Engineering, the M.S. degree in 2005, and the PhD degree in 2009 all in Electrical Engineering, from the Sfax Engineering National (SENS), University of Sfax, Tunisia. His research interests include power electronics and drives, and the implementation of advanced control strategies in AC motor drives applied to automotive systems. He is a member of the Research Laboratory on Renewable Energies and Electric Vehicles (RELEV) of the University of Sfax.

Abderrazak Yangui received the B.S, the DEA degree and the PhD degree in Electrical Engineering from the Sfax Engineering School (SENS), University of Sfax, Tunisia in 1982, 1992, respectively. His research interests include power electronics and drives, and the implementation of advanced control strategies in AC motor drives applied to automotive systems. He is a member of the Research Laboratory on Renewable Energies and Electric Vehicles (RELEV) of the University of Sfax